

INFLUENCE OF GADOLINIUM AS A DOPANT IN III-NITRIDE DILUTE MAGNETIC  
SEMICONDUCTORS

By

JENNIFER KRISTINE HITE

A DISSERTATION PRESENTED TO THE GRADUATE SCHOOL  
OF THE UNIVERSITY OF FLORIDA IN PARTIAL FULFILLMENT  
OF THE REQUIREMENTS FOR THE DEGREE OF  
DOCTOR OF PHILOSOPHY

UNIVERSITY OF FLORIDA

2006

To my family and friends

## ACKNOWLEDGMENTS

Many people helped support both the research presented in this dissertation and my own growth in undertaking it; too many to list individually. I appreciate all that each person contributed. In particular, I thank each member of my research group, especially those who taught me the basics and kept me laughing. I also thank each member of my committee for the inspiring thoughts and insightful conversations. I have enjoyed this second round at UF and learned much during my graduate career here.

## TABLE OF CONTENTS

	<u>page</u>
ACKNOWLEDGMENTS .....	3
LIST OF FIGURES .....	6
ABSTRACT.....	9
CHAPTER	
1 INTRODUCTION TO DILUTE MAGNETIC SEMICONDUCTORS.....	11
2 EXPERIMENTAL AND THEORETICAL BACKGROUND .....	13
Experimental Progress in DMS .....	13
Materials Research .....	13
III-As .....	13
III-N.....	14
Experimental Devices.....	16
DMS Theory .....	16
Free Carrier Mediated Model .....	16
Percolation Model .....	17
Extension to Rare Earth Dopants .....	17
3 EXPERIMENTAL GROWTH CONDITIONS AND CHARACTERIZATION OF DILUTE MAGNETIC SEMICONDUCTORS .....	19
Molecular Beam Epitaxy Approach .....	19
Solid Sources .....	20
Group V Sources .....	20
Sample Preparation and Loading.....	20
Growth Procedure.....	21
Sample Characterization.....	21
Superconducting Quantum Interference Device .....	22
X-ray Diffraction .....	22
Auger Electron Spectroscopy .....	23
Secondary Ion Mass Spectroscopy .....	23
Transmission Electron Microscopy .....	23
Hall Effect .....	24
Atomic Force Microscopy and Scanning Electron Microscopy.....	24
Reflection High Energy Electron Diffraction (RHEED).....	24
4 GROWTH AND DOPING EFFECTS ON GALLIUM GADOLINIUM NITRIDE .....	28
Growth Conditions and Characterization .....	28
Thickness Study.....	29

	Si Co-Doping Effects.....	31
	Summary .....	32
5	EFFECTS OF RADIATION ON GALLIUM GADOLINIUM NITRIDE .....	43
	Experimental Procedure.....	44
	Optical Effects .....	45
	Magnetic Effects .....	46
	Mechanism.....	47
	Summary .....	47
6	THERMAL ANNEALING EFFECTS ON GALLIUM GADOLINIUM NITRIDE BASED FILMS .....	58
	Experimental Procedure.....	58
	Rapid Thermal Annealing.....	59
	Nitrogen Incorporation and Annealing.....	59
	Anneal Recovery .....	60
	Summary .....	61
7	GROWTH AND CHARACTERIZATION OF GADOLINIUM-DOPED ALUMINUM GALLIUM NITRIDE.....	73
	Experimental Procedure.....	73
	Results and Discussion .....	74
	Summary and Conclusion.....	76
8	GADOLINIUM-BASED DILUTE MAGNETIC SEMICONDUCTOR HETEROSTRUCTURES .....	88
	Experimental Procedure.....	88
	GaGdN/AlN Heterostructures .....	89
	GaGdN:Si/AlN Heterostructures .....	90
	AlGaIn:Gd/GaN Heterostructures.....	90
	Summary and Conclusion.....	91
9	SUMMARY AND FUTURE WORD .....	101
	LIST OF REFERENCES .....	105
	BIOGRAPHICAL SKETCH .....	110

## LIST OF FIGURES

<u>Figure</u>	<u>page</u>
3-1 Different MBE growth modes: (a) Frank-van der Merwe, (b) Stranski-Krastanow, and (c) Volmer-Weber. ....	26
3-2 The Veeco Gen-II MBE system arrangement .....	27
4-1 RHEED image of 1 x 3 reconstruction seen in GaGdN:Si grown at $T_{Si} = 1200^{\circ}C$ . ....	33
4-2 XRD of GaGdN is shown for a 1500Å thick film grown at $T_{Gd} = 1050^{\circ}C$ . ....	34
4-3 AFM image of GaGdN:Si shown for a 1500Å sample grown at $T_{Si} = 1000^{\circ}C$ and $T_{Gd} = 1050^{\circ}C$ . ....	35
4-4 TEM images of GaGdN:Si showing highly ordered lattices. ....	36
4-5 PL spectra of GaGdN grown to 1500Å at $T_{Gd} = 1075^{\circ}C$ . ....	37
4-6 Estimated saturation magnetization and coercivity vs. GaGdN thickness shown. ....	38
4-7 Magnetization vs. applied field taken at 10 and 300K shown at top. ....	39
4-8 Electrical data as a function of Si cell temperature. ....	40
4-9 Estimated saturation magnetization and coercivity vs. Si cell temperature shown. ....	41
4-10 Magnetization vs. applied field taken at 300K for GaGdN:Si is shown at top. Bottom shows magnetization vs. temperature under a constant field of 200 Oe. ....	42
5-1 PL spectra of GaCrN after exposure to 0, 10, and 40 MeV protons. ....	48
5-2 PL spectra of GaGdN after exposure to 0, 10, and 40 MeV protons. ....	49
5-3 Band edge luminescence normalized to as grown values vs. photon exposure energy is shown. ....	50
5-4 Saturation magnetization vs. proton energy shown for GaCrN both before and after plasma annealing at $500^{\circ}C$ . ....	51
5-5 Saturation magnetization vs. proton energy shown for GaGdN both before and after plasma annealing at $500^{\circ}C$ . ....	52
5-6 Hysteresis loops for as grown and irradiated GaGdN samples. ....	53
5-7 Hysteresis loops for as grown and irradiated GaCrN samples. ....	54

5-8	Magnetization vs. applied field curves taken at 300K are shown for pre- and post-N <sub>2</sub> plasma annealing for GaGdN irradiated with 40 MeV protons.....	55
5-9	Magnetization vs. temperature curves showing zero field-cooled and field-cooled traces for GaGdN exposed to 10 MeV before and after annealing.....	56
5-10	Magnetization vs. temperature curves showing zero field-cooled and field-cooled traces for as grown, irradiated, and annealed GaCrN. ....	57
6-1	Normalized saturation magnetization of GaGdN plotted against RTA temperature.....	62
6-2	Normalized saturation magnetization of GaGdN:Si plotted against RTA temperature.. ....	63
6-3	Anneal temperature versus coercivity values shown. Values taken from hysteresis curves at 300K. ....	64
6-4	Normalized saturation magnetization of GaGdN:Si plotted against RTA temperature when under partial air. ....	65
6-5	Saturation magnetization plotted against nitrogen flow rate during GaGdN growth. ....	66
6-6	Nitrogen flow rate versus saturation magnetization shown for various plasma anneal temperatures.....	67
6-7	Normalized saturation magnetization versus nitrogen plasma anneal temperature for varying nitrogen flow rates during GaGdN growth.....	68
6-8	Hysteresis loops shown for GaGdN as grown, after a 700°C RTA, and further plasma annealing at 500°C.. ....	69
6-9	Magnetization versus applied field curves shown for GaGdN as grown, after RTA at 700°C, and further oxygen plasma annealing at 500°C.....	70
6-10	Hysteresis loops show magnetization for GaGdN as grown, after nitrogen plasma annealing at 700°C, and 60 min exposure to ultraviolet ozone.....	71
6-11	Hysteresis loops shown for GaGdN before and after 60 minutes of UV-O <sub>3</sub> exposure.....	72
7-1	Images of RHEED pattern for T <sub>Al</sub> = 1000°C. Top shows the faint 1 x 3 pattern. Bottom shows the start of 2D/3D growth. ....	77
7-2	Growth rate of AlGa <sub>N</sub> :Gd as a function of T <sub>Al</sub> is shown. ....	78
7-3	AFM image shows the surface of AlGa <sub>N</sub> with T <sub>Al</sub> = 1025°C (26% Al).....	79
7-4	Composition of Al in Al <sub>x</sub> Ga <sub>1-x</sub> N:Gd versus T <sub>Al</sub> is shown along with the linear fit of the data. ....	80

7-5	Indicative AES scan is shown for AlGa <sub>N</sub> :Gd at T <sub>Al</sub> = 1025°C after a 30 sec. sputter. ....	81
7-6	Carrier concentration as a function of Al composition is shown.....	82
7-7	Magnetization versus applied field curve shown for T <sub>Al</sub> = 1025°C (26% Al).....	83
7-8	Saturation magnetization vs aluminum cell temperature is plotted.....	84
7-9	Coercive field shown plotted against T <sub>Al</sub> .....	85
7-10	Magnetization versus temperature curve shows both zero field cooled and field cooled traces at an applied field of 200 Oe.....	86
7-11	Hysteresis curves before and after plasma annealing at 700°C for AlGa <sub>N</sub> :Gd with T <sub>Al</sub> = 1025°C (26% Al). ....	87
8-1	Schematic showing structure for GaGdN/Al MQW.....	92
8-2.	Hysteresis curve is shown for a 33x 25Å/100 Å GaGdN/AlN MQW.....	93
8-3	XRR spectrum is shown for the 10 periodicity GaGdN/AlN sample with layer thicknesses of 9/5.4nm.....	94
8-4	Magnetization versus applied field is shown for a 10 periodicity 90Å/52Å GaGdN/AlN structure. ....	95
8-5	Magnetization versus applied field is shown for 10 repetitions of 90Å/80Å GaGdN:Si/AlN layers.....	96
8-6	Magnetization versus applied field loop shown for 5x 180Å/80Å GaGdN:Si/AlN layers taken at 300K.....	97
8-7	Magnetization versus temperature traces for field cooled and zero field cooled curves are shown for 5x GaGdN:Si/AlN 180Å/80Å layers. ....	98
8-8	Figure 8-3. XRR spectrum is shown for the 10 periodicity GaN/AlGa <sub>N</sub> :Gd sample with layer thicknesses of 8.7/18.54nm.....	99
8-9	Hysteresis loop is shown for 10 repetitions of 18.5/8.7nm AlGa <sub>N</sub> :Gd/GaN layers taken at 300K. ....	100

Abstract of Dissertation Presented to the Graduate School  
of the University of Florida in Partial Fulfillment of the  
Requirements for the Degree of Doctor of Philosophy

INFLUENCE OF GADOLINIUM AS A DOPANT IN III-NITRIDE DILUTE MAGNETIC  
SEMICONDUCTORS

By

Jennifer Kristine Hite

December 2006

Chair: Cammy Abernathy

Major Department: Materials Science and Engineering

With the current interest in spintronics, many attempts have been made toward incorporating spin-based functionality into existing semiconductor technology. One such approach uses dilute magnetic semiconductors (DMS), formed by the introduction of metal ions into III-Nitride hosts, taking advantage of existing wide bandgap device technology. Several transition metal doped DMS materials have been developed to display room temperature ferromagnetism, but the impurity band contributed by large concentrations of TM dopants has made device development difficult.

Instead, using the rare earth metal Gd as an exceedingly dilute dopant in GaN has demonstrated room temperature hysteresis. It has been established that this ferromagnetic behavior is a bulk property, dependent on both dopant flux and crystal quality. In addition, Fermi level manipulation is possible through the addition of Si, resulting in some improvement in magnetic saturation. The magnetic properties are also dependent on nitrogen incorporation, and optimized levels have been determined. Both GaGdN and GaGdN:Si experience some magnetic degradation when thermally annealed under various conditions, falling to around 75% of their as grown values.

High energy proton irradiation of GaGdN has also been examined. The films responded to irradiation with decreasing band edge photoluminescence along with a large loss of magnetic signal at the highest energy. Annealing under nitrogen plasma produced a complete magnetic recovery of the irradiated samples, but not the as grown material.

Introducing Gd into AlGa<sub>1-x</sub>N<sub>x</sub> has also been investigated. The resulting AlGa<sub>1-x</sub>N<sub>x</sub>:Gd material has also shown room temperature ferromagnetism which is dependent on Al content. Conductivity and coercivity of these samples are also correlated to Al concentration. Some thermal instability has been observed, but a strong magnetic signal is still detected.

From these results, it can be concluded that Gd should be an excellent candidate for incorporation into spintronic devices. No device has yet been developed, but the effects of reduced dimensionality have been explored by fashioning these Gd-doped DMS films into heterostructures. At thicknesses as low as 90 Å for GaGdN, hysteresis equivalent to the bulk material has been discerned, which is the last hurdle for this material before attempting to integrate it into device structures.

## CHAPTER 1 INTRODUCTION TO DILUTE MAGNETIC SEMICONDUCTORS

One of the signatures of a growing civilization is to increase the standard of living of each succeeding generation. Advances in technology have normally spurred the developments that implement this progression. The prehistoric cavemen inventing the wheel, spinning jennys and cotton gins in the 1800s, industrialization in the 1900s are all examples. Our current progress is based on advances in semiconductors and magnetic storage, as seen in the laptops, cell phones, memory sticks, and PDAs that run our lives. The continuation of this lifestyle mandates the development of devices that are smaller, faster, and use less power. The last great leap in microelectronics occurred with the introduction of the transistor in 1948, which manipulated electron charge in semiconductors, instead of the actual electrons used in vacuum tubes.<sup>1</sup> Over the last decade, the field of spintronics, or spin transport electronics, has risen to the forefront as the next breakthrough in electronics.

Where conventional microelectronic devices use the charge of electrons to carry information, the field of spintronics creates an additional degree of freedom by manipulating the spin of electrons.<sup>1-5</sup> This inherent characteristic of electrons has two states—spin up and spin down—and is the source of some of the advantages of spintronics, for spin states require much less work to manipulate than does charge. In addition to the previous goals, this field proposes to deliver non-volatile devices.<sup>3</sup> It also allows for possible integration of electrical, photonic, and magnetic functions all on the same chip.

Practical application of spintronics has already become commercially viable in the area of digital storage and is now a billion dollar per year industry.<sup>6</sup> Magnetoresistance, or resistance depending on relative magnetic spin, is responsible for its growth. In 1997, IBM utilized giant magnetoresistance (GMR) in read heads.<sup>1</sup> In this sandwich-type structure of metallic alloys, after application of a magnetic field, the degree of spin alignment (or randomization) controls the

resistance to current flow. More sensitive devices require new magnetic alloys with smaller magnetic domains.<sup>1-3</sup>

Introducing an insulator in the middle of the sandwich takes the GMR structure to the next step of using the quantum aspect of spin. This type of device is known as a magnetic tunnel junction. The insulator enables spin polarized current to be completely cut off if the spins of the abutting layers are antiparallel and is a possible source of non-volatile devices.<sup>1-6</sup> Magnetic random access memory (MRAM) has been developed along these lines and is currently utilized by the military, as well as applied to the cellular phone industry.

Although the GMR devices have been a commercial success, their basis on ferromagnetic metals makes them unsuitable for devices that require gain, such as light-emitting diodes (LEDs) and transistors.<sup>7</sup> Additionally, the microelectronic industry is geared towards manufacturing semiconductors, not metals. This has led to increasing interest in duplicating the MR response in semiconductors. Trying to bridge the gap by introducing semiconductors into the metallic GMR structures is not a viable option since spin transport between metals and semiconductors is extremely inefficient. An all semiconductor structure has the capability to solve these issues.<sup>2,4</sup>

In the search for an all semiconductor spintronic device, dilute magnetic semiconductors (DMSs) have become increasingly popular. Fabricating a DMS involves introducing a low concentration of magnetic ions which incorporate substitutionally throughout the crystal lattice of the semiconductor. There are several hurdles to producing an efficient DMS material. Some of these include obtaining room temperature ferromagnetism, efficient spin injection, and long spin relaxation times.<sup>1-8</sup> Various work has progressed on these materials, and some compound semiconductors have shown remarkable control over these parameters. Using compound semiconductor based DMS also brings the advantages of tunable band gaps, lattice matching, and optically active material which expand the influence of this material.<sup>9,10</sup>

## CHAPTER 2 EXPERIMENTAL AND THEORETICAL BACKGROUND

### **Experimental Progress in DMS**

In forming a DMS, the first hurdle to be surmounted for practical application is obtaining material with room temperature ferromagnetism (FM). Materials with Curie temperatures below room temperature are conceivable, but would require extra cooling via sources like liquid nitrogen and liquid helium, making them impractical for mobile devices or everyday use. After obtaining room temperature FM, the spin properties such as transport and lifetime must be studied and the magnetization optimized. For further use in devices, the material should exhibit controllable Fermi levels (via doping), lattice matching, and radiation hardness.

### **Materials Research**

The first magnetic semiconductors studied were the europium chalcogenides and II-IV semiconductors in the 1960s and 70s. The Eu-chalcogenides proved difficult to grow due to large lattice mismatch between the substrates (Si and GaAs) and crystalline film.<sup>11</sup> In addition, these materials were grown with concentrated dopant concentrations, with  $\text{Eu}^{2+}$  on every lattice site.<sup>2,4,12</sup> The II-IV semiconductors were found to be hard to dope p- or n-type, and the resulting magnetization was of spin glass, paramagnetic, or antiferromagnetic nature.<sup>4,11</sup> In addition, neither of these materials exhibited ferromagnetism above  $\sim 100$  K.<sup>13</sup>

Producing DMS from III-V semiconductors has shown great promise, with room temperature ferromagnetism shown in Mn doped GaP,<sup>14</sup> GaN,<sup>15-17</sup> and AlN.<sup>18,19</sup> As there is already an industry base for fabricating III-V heterostructures, this material is extremely well suited for introduction into device structures. The following sections will focus on studies conducted in III-V DMS materials.

### **III-As**

The first III-V material to show hole-induced ferromagnetic order was Mn-doped InAs. Low temperature growth via MBE was necessary to retard the formation of MnAs clusters and magnetic

ordering depended on the carrier type. Single phase n-type InMnAs exhibited only paramagnetic behavior, while p-type showed ferromagnetism with a  $T_C$  of 7.5 K.<sup>20,21</sup> Although this Curie temperature made it unsuitable for practical device applications, an anomalous Hall Effect was observed in a InMnAs/GaSb heterostructure along with light induced ferromagnetism.<sup>21,22</sup> After this discovery, research shifted to the benchmark material GaAs, which had been extensively studied in heterostructure devices. GaMnAs has the same difficulties as InMnAs in avoiding MnAs cluster formations, so the same low temperature regime must be employed. In addition to this difficulty, the highest  $T_C$  achieved has been a low 110 K.<sup>12</sup> Due to this apparent temperature plateau, most groundbreaking research on GaAs has ceased, especially after much higher  $T_C$  values have been discovered in DMS III-nitride materials.

### **III-N**

Within the III-Ns, GaN and AlN have been thoroughly researched due to their applications in ultraviolet, optical, and high temperature electronics. Doping either of these materials without precipitating secondary phases is difficult, and must be performed under non-equilibrium conditions. In this group, the most widely studied DMS is GaMnN, with reported Curie temperatures ranging between 10 and 940 K depending on growth and annealing conditions.<sup>15,-17,23,24</sup> In general, this system has shown an upper limit on the Mn concentration, above which the films show paramagnetic behavior.<sup>15-17,23</sup> In GaMnN, there arises an additional question of whether the material is an alloy, or if Mn clusters within the film may be causing the magnetization.

In response to issues with Mn doping, various other transition metal dopants have been investigated. One of the more promising of these is Cr. GaCrN has been shown to exhibit ferromagnetic behavior above room temperature, and has even had a reported  $T_C$  over 900°C.<sup>25-28</sup> Unlike GaMnN, issues of clustering have not been seen in GaCrN films, and the material has been shown to be a truly ternary film.<sup>25-29</sup> While the Cr atom sits substitutionally in the lattice, the magnetic moment increases with concentration, but once these sites are saturated, interstitial Cr is

believed to cause a degradation in magnetic signal.<sup>25,28</sup> Of additional interest, the magnetic signal has also been shown to be thermally stable past 700°C, which is much higher than that for GaMnN.<sup>27</sup> These films have also exhibited paramagnetic behavior, or a “paramagnetic tail”, at low temperatures.<sup>25-29</sup>

Lanthanide series elements, also known as rare earth metals, have also shown promise. Rare earths have long been studied as dopants in GaN, due to the possibility of developing tunable light emissions from intra-transitions in the *f* suborbital. Not as much attention has been focused on developing them as DMSs until recently. Eu-doped GaN has been reported to possess room temperature ferromagnetism. However, both paramagnetic and ferromagnetic behaviors have been observed. This is believed to arise from the presence of Eu in both trivalent and divalent valence states.<sup>30,31</sup> Although the majority of the dopant has been observed in the trivalent form, the Eu<sup>+2</sup> state has been found prevalently at the GaN surface and is believed to be the one responsible for the ferromagnetic behavior.<sup>32</sup> This valency issue can be avoided when using Gd, another rare earth dopant with a trivalent valence state.<sup>33</sup> GaGdN has also exhibited room temperature ferromagnetism in both implanted material and in epitaxial films grown on SiC substrates.<sup>2a,34-37</sup> Interest in this material has intensified since recent calculations of the moment per metallic ion of epitaxially grown Gd at low dopant concentrations report the material to have an extremely large moment of 4000  $\mu_B/\text{Gd}$ .<sup>36</sup> This is significantly greater than the value for bulk Gd (8  $\mu_B/\text{Gd}$ ) or any other ferromagnetic compounds formed with Ga or N, such as GdN (7  $\mu_B/\text{Gd}$ ). Further work by this group has reported the moment of Gd ions in unannealed implanted GaGdN films to be an order of magnitude larger than epitaxially grown material, implying that defects may contribute to the large magnetic ordering in this system.<sup>38</sup>

## Experimental Devices

The plausibility of using III-V DMS materials for spintronic applications has been experimentally proved by TMR and MR behavior of tri-layer structures such as GaMnAs/AlGaAs/GaMnAs<sup>39</sup> and GaMnAs/AlAs/GaMnAs.<sup>40</sup> However, the TMR behavior in these heterostructures is lost at increasing temperatures (>20K), making them unviable for practical applications.<sup>39,40</sup> In the III-N realm, a spin LED structure has been attempted, using a GaMnN/GaN/InGaN structure, which emitted a small signal of polarized light when under a strong applied magnetic field.<sup>41</sup> As for dopants other than Mn, a GaCrN/GaN/GaCrN tunnel diode has shown magnetoresistance, but not tunneling, leading to the conclusion that GaN is not a sufficient tunnel barrier. Instead, it has been theorized that AlN or AlGaN might form an adequate barrier.<sup>42</sup> In fact, first order calculations predict efficient spin transport from GaCrN through an AlN barrier.<sup>43</sup> To this effect, ferromagnetic AlMnN<sup>18,19</sup> and AlCrN<sup>44,45</sup> have been produced by molecular beam epitaxy, resulting in room temperature ferromagnetism for single crystal films.<sup>19,44,45</sup> However, no resulting devices have been reported yet.

## DMS Theory

Through all the previous research on DMS materials, one universal theory for the behavior of these systems has been developed. The current models can be separated into two different approaches: free carrier mediated and percolation. With the introduction of rare earths into DMS matrices, these models are being stretched even further.

### Free Carrier Mediated Model

Starting with a mean field approximation, in which the DMS material is taken to be an alloy with a random metallic atom sitting substitutionally on the lattice, Zener developed a model explaining ferromagnetism for transition metals in the 1950s. This model was based on indirect coupling between an incomplete *d* shell and conduction electrons.<sup>46</sup> However, it neglected the itinerant character of the magnetic electrons, as well as Friedel oscillations. Years later, Zener's

model was re-examined by Dietl *et al.* who reasoned that for semiconductors the separation between carriers is larger than that between spins, resulting in the Friedel oscillations averaging to zero.<sup>47</sup> In this form, the Zener model becomes equivalent to the Ruderman-Kittel-Kasuya-Yosida (RKKY) interaction model and relies on a high carrier density (on the order of  $10^{20} \text{ cm}^{-3}$ ). Dietl *et al.* further used the Zener model to predict the  $T_{CS}$  for various III-V and II-IV materials doped with Mn, resulting in predicted  $T_{CS}$  for both GaN and ZnO above room temperature.<sup>47,48</sup> In addition, it was determined that increasing the hole concentration had a correlating effect in increasing the Curie temperature. Although this model has been modified to fit some DMS material, it does not explain ferromagnetic behavior for insulating DMS materials.

### **Percolation Model**

For low carrier concentration systems, in which the carrier concentration is much lower than that of the magnetic ions, mean field approximation does not apply, and a different model must be developed.<sup>49,50</sup> The most prevalent is the polaron percolation model. In this theory, localized carriers undergo exchange interactions with magnetic dopants to form bound magnetic polarons (BMPs).<sup>51</sup> Although the direct interactions between ions may be ferromagnetic (as in the case for Mn), the indirect interaction between the carrier and ion allows for ferromagnetism to exist.<sup>52</sup> As the reach of these BMPs expands and becomes aligned, the material attains ferromagnetism. An impurity band of carriers has been theorized to form from the BMPs, with any electronic transport enabled by holes hopping through this band.<sup>51,53</sup> When using Mn as a dopant, this theory promotes the idea that increasing the Mn concentration will cause a decrease in ferromagnetism, due to increasing anti-ferromagnetic Mn-Mn interactions. Further theoretical analysis indicates that the disorder of magnetic ions also affects the ferromagnetism of the DMS.<sup>52-54</sup>

### **Extension to Rare Earth Dopants**

The majority of theoretical work has focused on Mn or other *d* suborbital transition metals. When dealing with Lanthanide series dopants, the additional *f* shell interactions complicate matters.

Focusing on Gd within GaN, Dhar et al. have proposed a percolation-like explanation for the observed ferromagnetism.<sup>36,37</sup> Dalpian and Wei have taken a different approach to understanding the mechanism behind the large ferromagnetism observed in GaGdN.<sup>56</sup> By performing *ab initio* band structure calculations, they predict an electron-stabilized model for this ferromagnetism. According to their calculations, the addition of Gd introduces coupling between the *s* and *f* suborbitals and allows for larger spin splitting at the conduction band than at the valence band. This introduces new localized states below the conduction band. Once these new states are filled by additional donor electrons, perhaps from the high levels of oxygen present in the GaGdN films, they become spin polarized. With sufficient new states filled, this model can explain the large magnetic moment observed per Gd ion at low dopant concentrations.<sup>56</sup> LDA models concur with the necessity of a mechanism beyond pure percolation theory, as the magnetic interactions of rare earth ions with host states are much weaker than those of *3d* impurities with valence and conduction band edges.<sup>33</sup> In the case of electron stabilized ferromagnetism, addition of shallow donors, such as Si, should also help stabilize magnetic ordering. Although none of these models focus on explaining the role defects or trap levels plays on the ferromagnetism of the material, it can be reasoned that for an electron-stabilized system, any additional competition for electrons would decrease the magnetic moment of the films.

## CHAPTER 3 EXPERIMENTAL GROWTH CONDITIONS AND CHARACTERIZATION OF DILUTE MAGNETIC SEMICONDUCTORS

In developing dilute magnetic semiconductors for device applications, single crystalline films with low defect densities are necessary. One of the most well-established methods to achieve this is with molecular beam epitaxy (MBE). This is due to several advantages over other epitaxial growth methods, mainly the ability to grow at low growth rates, low substrate temperatures, and with abrupt interfaces, the first two of which are especially important in incorporating metal dopants into the lattice. The ability to produce abrupt interfaces allows for the extension to heterostructures as well as novel structures, such as quantum dots and wells.

### **Molecular Beam Epitaxy Approach**

MBE growth can be described as the reaction of molecular beam constituents with a heated crystalline surface, which is enabled by ultra high vacuum conditions. The molecular beams are produced by heating solid sources in Knudsen effusion cells. An externally controlled shutter covers the cell opening and is responsible for the abrupt start or cessation of growth. After impinging on the surface, the atomic species undergo absorption and migration to collide and deposit on the substrate. Control over the growth is achieved by manipulating the substrate temperature or the Group III/V ratio, which is, in turn, dictated by the Group III flux or the Group V flux. Epitaxial growth can occur in one of three modes: layer-by-layer (Frank-van der Merwe mode), layer-plus-island (Stranski-Krastanow mode), or island (Volmer-Weber mode) growth, which are illustrated in Figure 3-1.

MBE growth described herein was carried out in a Varian Gen II system (Figure 3-2). This system consists of a loadlock, buffer chamber, and growth chamber where up to 8 source cells can be attached. In addition, a reflection high energy electron diffraction system lies in situ to monitor the films during growth. A mass spectrometer can also be attached which is employed during leak checking or to identify any other gaseous species present during the growth process. The remainder of this section will specify the MBE apparatus and growth procedures.

## **Solid Sources**

Using solid sources allows for more flexibility when identifying appropriate transition metals for doping purposes. The group III cell sources are either aluminum (Al) or Gallium (Ga), with purity levels of 7N each. In respect to purity, 99.99999% purity corresponds to 7N, where the number of nines (x) is counted as xN. Reloading these cells involves venting the entire chamber, which is normally performed once a year. Solid sources are also used for the dopants: 6N silicon, 4N gadolinium (Gd), and 5N chromium. The low purity for Gd stems from the difficulty in separating rare earth metals.

## **Group V Sources**

For III-Ns, there are several sources for nitrogen; the most established of these are ammonia or nitrogen gas. Bottled nitrogen is the safer of the two, and at 6N purity, was the group V source for material in this work. An Oxford RF plasma head operating at 13.56 MHz is used to ionize the nitrogen entering the chamber. This plasma head is coupled to a mass flow controller which maintains a constant gas flow into the growth chamber.

## **Sample Preparation and Loading**

Three main sources of substrate may be employed: silicon (Si), silicon carbide (SiC), or sapphire ( $\text{Al}_2\text{O}_3$ ). Each of these possesses a different lattice match to the III-Ns. The films described in this dissertation were grown on sapphire unless otherwise stated on top of which a GaN buffer layer is grown by either metal organic chemical vapor deposition (MOCVD) or low temperature MBE (LTMBE). Since it has been shown that the choice of buffer layer has a large impact on the resulting overlayer, especially with regards to roughness and magnetic characteristics,<sup>17,27</sup> a 2  $\mu\text{m}$  MOCVD GaN buffer was utilized. To remove the native oxide of the buffer layer, the cleaning process entails a 3 minute immersion in hydrochloric acid (HCl), 25 minute ultraviolet ozone (UV- $\text{O}_3$ ) exposure, and 5 minute buffered oxide etch immersion. After a deionized water rinse and drying under nitrogen, the samples are ready to be mounted on molybdenum blocks using a thin layer of

indium. The indium allows for efficient and uniform heat transfer between the block and sample. Samples are then loaded on a trolley and placed in the loadlock. They are transferred into the buffer chamber after the loadlock pressure has been reduced to  $10^{-7}$  Torr. Once inside the buffer chamber, the samples are enveloped in near UHV, protecting them from oxygen and moisture and can remain there until the growth run is imminent.

### **Growth Procedure**

Prior to growing, the two cryoshrouds of the growth chamber are filled with liquid nitrogen ( $\text{LN}_2$ ). The cryoshrouds enhance the vacuum level and increase the purity of the grown layers. Then the effusion cells are heated to the desired temperature and the fluxes of the solid cells are taken with an ion gauge placed in the path of the beam. A three prong arm transfers the sample block into the growth chamber. Nitrogen is introduced into the chamber, and the plasma is lit and tuned at 300 W. Next, the sample is rotated  $180^\circ$  to face the cells, and the substrate is heated to the required temperature. Lighting the plasma before heating the substrate ensures a nitrogen overpressure to maintain stoichiometry in the GaN buffer, securing an optimal surface on which to begin growth. The sample rotation is set to 10 rpm to provide uniform coverage. Once all this has occurred, the shutters are opened to begin growth. To end growth, the shutters are closed, and the substrate temperature is set to zero. When the substrate temperature cools down to  $300^\circ\text{C}$ , the substrate is rotated towards the buffer chamber and the plasma is turned off. The nitrogen flow to the chamber is also turned off. Once the chamber pressure has decreased to about the same level as the buffer chamber, the sample block is transferred back into the buffer chamber.

### **Sample Characterization**

After the epitaxial films have been grown and removed from the chamber, they are dismantled from the blocks and prepared for characterization. The magnetic, electrical, structural, and chemical properties of the resulting films are studied in order to determine the effect of the parameters varied

during growth. The remainder of this section gives a brief review of some of the more important characterization tools used in this work.

### **Superconducting Quantum Interference Device**

Magnetic measurements were performed using a Quantum Device Magnetic Properties Measurement System Superconducting Quantum Interference Device (SQUID) magnetometer. In order to prepare a sample for SQUID, a 5 mm<sup>2</sup> section is cleaved off and the indium is completely removed from the back. Two types of measurements are obtained from SQUID magnetometry. The first is a magnetization versus applied field curve at a constant temperature, from which saturation magnetization and coercivity for ferromagnetic materials can be determined. If the material exhibits ferromagnetic behavior, then a magnetization vs. temperature curve at a set applied field is called for. This type of measurement can be used to indicate the Curie temperature ( $T_C$ ) of the material. This test is also known as a Field Cooled/Zero Field Cooled (FC/ZFC) measurement, where the sample is cooled to 10 K under a set applied field while measuring the samples magnetization (FC) and then measured under zero field as the sample warms back to room temperature (ZFC). The magnetic field is applied parallel to the sample surface for all measurements.

### **X-ray Diffraction**

X-ray diffraction (XRD) is used to structurally analyze the samples, specifically to determine whether or not second phases are introduced into the material by the metallic dopants. The XRD measurements were performed in a Philips APD 3720 system that uses a copper (Cu) x-ray source. The source predominantly emits Cu  $K_{\alpha 1}$  x-rays with a 1.54056 Å wavelength for diffraction, although  $K_{\alpha 2}$  and  $K_{\beta}$  x-rays are emitted as well. The XRD has a sensitivity of <0.05% by volume, so is slightly impractical for very low concentration dopants. In addition, high resolution XRD (HRXRD) was performed on multilayer samples via a Philips X'pert High Resolution X-ray

Diffraction system in order to determine layer thicknesses. It can also be used to determine chemical composition of ternary compounds.

### **Auger Electron Spectroscopy**

For chemical composition, Auger electron spectroscopy (AES) is utilized. The measurements were performed in a Perkin Elmer 6600 which is also equipped with an Ar sputtering gun and can determine chemical composition of constituents greater than 1 at%. Since AES is a surface sensitive analytical tool, surface measurements can be skewed by surface oxygen or carbon, thus the sputtering gun was employed to tunnel into the bulk material before measurements were taken. The analysis is accomplished by examining peak heights using published elemental sensitivity factors.

### **Secondary Ion Mass Spectroscopy**

Secondary Ion Mass Spectroscopy (SIMS) is the most exact method of determining chemical composition throughout the film, and is the most sensitive for low level dopants. Samples for dynamic SIMS analysis were sent out to Evans Analytical Group which used  $O_2^+$  and  $Cs^+$  ions to bombard the sample surface. The sputtered material consists of ions and neutral atoms. The ions are electrostatically sent into a mass analyzer. The mass analyzer selects the desired ions and directs them into the detector. As the primary ion beam sputters into the sample, material from different depths is sent into the detector, thus monitoring the concentration of a particular element at different depths. The primary beam is rastered to create a flat-bottomed crater. Ions are acquired only from the center of the crater, thus ensuring that each data point comes from a unique depth. The secondary ion signal intensity from different depths is then used to construct a concentration depth profile. For samples containing Gd, a reference sample of ion implanted Gd into GaN was prepared and measured.

### **Transmission Electron Microscopy**

Structural analysis is also accomplished with transmission electron microscopy (TEM). TEM requires a great deal of sample preparation to make them thin enough (~ 200 nm) for an electron

beam to pass through the sample. The most useful ability of TEM for these samples is the ability to obtain high resolution images of the matrix lattice and boundaries. In addition TEM can detect small clusters of dopants that are otherwise imperceptible to other methods.

### **Hall Effect**

The Hall Effect is a powerful tool in determining the electrical characteristics of a material. From it, the carrier type, carrier concentration, and resistivity can be established. To prepare a Hall sample, an 8 mm<sup>2</sup> piece is taken from the main sample and indium dots are soldered onto the corners. The measurements are made at room temperature with a 0.36 Tesla magnet that allowed for both Van der Paaw and Hall measurements to be performed.

### **Atomic Force Microscopy and Scanning Electron Microscopy**

Surface morphology is examined using atomic force microscopy (AFM) or scanning electron microscopy (SEM). SEM gives high resolution images of the sample surface, and can also be used with cross-sectional samples to determine sample thickness. AFM also records images of the sample surface, but with additional software it provides root mean square (RMS) roughness values for the surface. Although both methods have similar lateral resolution, at smaller scales some issues can arise in AFM due to tip conformation or tip imaging, giving SEM an advantage. On the other hand, interpreting distances in the z-scale, which is easily obtained using AFM, is nearly impossible via SEM.

### **Reflection High Energy Electron Diffraction (RHEED)**

As previously mentioned, the MBE growth chamber is equipped with a Reflection High Energy Electron Diffraction (RHEED) apparatus permitting *in situ* analysis of the structural surface of the films, relaying information on crystal structure, crystal orientation, and the degree of surface roughness. The system consists of an electron gun and phosphorescent screen. The gun intersects the sample surface at a 1-2° grazing angle, undergoes diffraction from the top couple of monolayers of the surface, and is reflected onto the phosphor screen. In epitaxial growth, RHEED is used most often

to determine surface roughness and growth mode. Streaky lines are indicative of the 2D layer by layer growth that is most desired in crystalline films. Spots signify 3D islanding growth, while rings denote polycrystalline growth, and no pattern is produced by amorphous films.

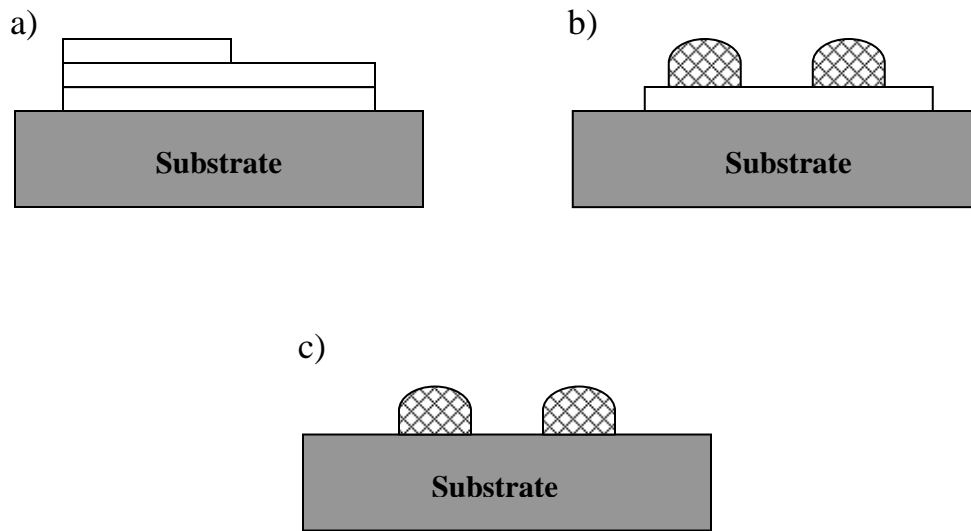


Figure 3-1. Different MBE growth modes: (a) Frank-van der Merwe, (b) Stranski-Krastanow, and (c) Volmer-Weber.

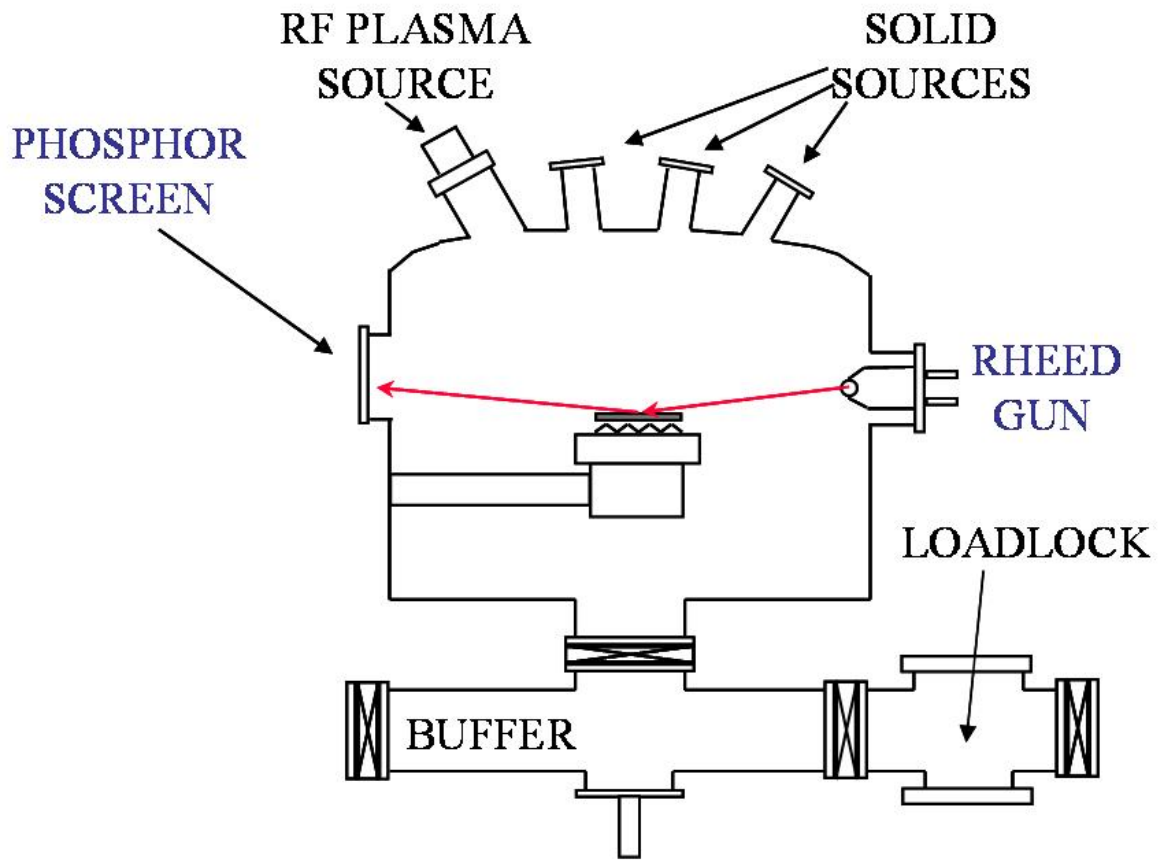


Figure 3-2. The Veeco Gen-II MBE system arrangement

## CHAPTER 4 GROWTH AND DOPING EFFECTS ON GALLIUM GADOLINIUM NITRIDE

Though previous work has shown GaGdN to behave ferromagnetically, depending on the Ga/Gd ratio,<sup>57</sup> there is still much work to be done to understand this system. In order to do so, this study concentrates on two focal points. The first of which is to determine if the ferromagnetic behavior of the material is a bulk or surface/interface phenomena. This is accomplished by comparing the magnetization of material with varying thicknesses. Since the magnetization is normalized by volume, the measured signal from bulk properties should be constant, while those from surface phenomena would constantly decrease with increasing thickness. Secondly, the consequences of co-doping the material will be explored. Changing the electrical nature of the GaGdN by introduction of other dopants would be highly useful in device applications. The effect of extra donors may also shed some light on the mechanism involved in the ferromagnetic behavior of this material.

### **Growth Conditions and Characterization**

Previous optimization of GaGdN in the MBE chamber determined the ideal growth conditions for GaGdN to be at a substrate thermocouple temperature of 700°C and a Gd cell temperature ( $T_{\text{Gd}}$ ) of 1050°C.<sup>57</sup> These were the base conditions, along with a flow rate of 1.6 sccm, used during this study while varying thicknesses of GaGdN and GaGdN co-doped with silicon. Additional doping was achieved by varying the Si cell temperature ( $T_{\text{Si}}$ ) from 1000 to 1200°C, as measured by the cell thermocouple.

Film growth was monitored *in situ* by reflection high energy electron diffraction (RHEED). Streaky RHEED patterns were observed for most of the films, indicating two dimensional (2D) growth, with 1 x 3 reconstruction (Figure 4-1). Thicker films and high Gd-cell temperature films tended to become spotty. The samples were also characterized using powder x-ray diffraction (Figure 4-2), which found no second phases, and atomic force microscopy, in which the root mean square

roughness was about 1.8 nm in GaGdN, and slightly smoother in the Si co-doped films (Figure 4-3). Transmission electron microscopy (TEM) images of the film also showed a lack of secondary phases along with a highly ordered interface and lattice structure (Figure 4-4). Photoluminescence spectra were taken of the GaGdN (Figure 4-5) and showed the same band edge transitions and yellow luminescence band as undoped GaN, but exhibited an additional peak at 1.7 eV which can be attributed to *f* suborbital transitions.

The concentration of Gd within the films was investigated via secondary ion mass spectrometry (SIMS). Similar to previous reports<sup>36,37</sup> this concentration was extremely low, falling under the SIMS background level of  $2 \times 10^{17}$  atoms/cm<sup>3</sup>. The oxygen content in these samples was on the order of  $10^{19}$  atoms/cm<sup>3</sup>. This is analogous to previous TM-doped films grown on the same system. The oxygen concentration in undoped GaN is approximately  $10^{18}$  atoms/cm<sup>3</sup>, suggesting that the Gd cell is the source of the oxygen. SIMS did not find any other magnetic species in the samples.

The Gd-doped films were extremely resistive, in contrast to the undoped GaN which shows a carrier concentration of about  $10^{16}$  cm<sup>-3</sup>. This is a surprising contrast given the higher oxygen concentration in the GaGdN. The trivalent Gd ion (Gd<sup>3+</sup>) has seven unpaired electrons in the unfilled 4f shell which is shielded by the completely filled 5s and 5p shells, i.e. the electronic structure of Gd is  $4f^7 5d^1 6s^2$ . Thus, it is not a deep acceptor in GaN and would not compensate the background n-type carrier concentration. The cause of the reduced carrier concentration remains unknown, but is likely due to a change in the point defect concentration incorporated during growth due to the presence of Gd at the growth surface.

### **Thickness Study**

To rule out interface effects as the source of ferromagnetism in the samples, GaGdN films were grown at thicknesses varying between 0.1  $\mu\text{m}$  and 0.6  $\mu\text{m}$ , at  $T_{\text{Gd}} = 1050$  °C. If interfacial effects were influencing the ferromagnetism, then the magnetic signal as a function of volume should

steadily decrease with increasing film thicknesses. Instead of steady degradation, the magnetization takes a sudden drop at the 0.1  $\mu\text{m}$  thickness, but then appears to level off as demonstrated in Figure 4-6. The high degree of magnetism seen at the 0.1  $\mu\text{m}$  thickness has been repeated, and can be attributed to better crystal growth, as increasing thickness corresponded with a trend towards three dimensional growth. The measured coercivity for these films stayed fairly constant with measured values between 38.5 and 43.17 Oe, also shown in Figure 4-6. Dhar *et al.* have reported thickness independence as measured by a moment per area basis in their films.<sup>37</sup>

These films also appear to have  $T_{CS}$  beyond room temperature, as shown by the absence of change in hysteresis at high and low temperature in the magnetization vs. applied field curves for the GaGdN films. A sample of this is shown for a 0.1  $\mu\text{m}$  film in Figure 4-7. The magnetization vs. temperature shown in the inset of Figure 4-7 supports the same conclusion as evidenced by the lack of closure between the field cooled and zero field cooled lines.

The mechanism behind the ferromagnetism of this system is still under consideration. Due to the high resistivity of the material, the free carrier mediated theory cannot be used to explain the magnetic behavior. Dhar *et al.* and Dalpain *et al.* have recently proposed models to explain the ferromagnetism in this dilute doped system, both of which are based on long range polarization of the area surrounding each Gd atom.<sup>36,37,56</sup> However, Dalpain has further suggested the phenomenon requires shallow donor impurities to occupy  $f$  states created by the Gd below the conduction band.<sup>56</sup> This is interesting, especially noting the high concentration of oxygen in both our films and those of Dhar *et al.*<sup>36,37</sup> These models also allow for the signal peak seen in optimization studies due to overlapping Gd spheres of influence, and the decline in moment at higher Gd cell temperatures. Lambrecht<sup>58</sup> has pointed out that it is not necessary for the Gd levels to be below the oxygen-induced levels in the case of a degenerate semiconductor with most of the oxygen donors ionized, since their electrons would reside in a spin-split conduction band. He has suggested that oxygen or other donors

do not merely provide the electrons for the spin-split states but participate actively in the spin-splitting itself of the conduction band minimum.<sup>58</sup>

### **Si Co-Doping Effects**

Co-doping with Gd and Si was carried out to see if extra shallow donors would affect the ferromagnetism of the material. The films were grown at  $T_{Si}$  between 1000 and 1200°C and a thickness of 0.15  $\mu\text{m}$ , maintaining the Gd cell temperature at 1050°C. Two dimensional growth with 1 x 3 reconstruction (Figure 4-1) was recorded and resulted in conductive n-type material. At  $T_{Si} = 1000^\circ\text{C}$ , the material was still slightly resistive, but carrier concentration markedly improved from there, increasing an order of magnitude with each 100°C change in Si cell temperature, reaching  $1.45 \times 10^{18} \text{ cm}^{-3}$  with the highest concentration of Si. Meanwhile, the Hall resistivity dropped to 0.04  $\Omega \text{ cm}$ . The changes in electrical characteristics with Si incorporation are shown in Figure 4-8. The films also exhibited ferromagnetic behavior. The magnetic saturation and remnant magnetization increased linearly with cell temperature, while the coercivity showed the opposite trend (Figure 4-9). The coercivities of the co-doped material ranged from 40 to 45 Oe. This is within the same values as those of the purely Gd-doped films, but in a smaller range. Remnant magnetization and coercivity for the higher  $T_{Si}$  films were comparable to the 0.1  $\mu\text{m}$  thick GaGdN films. The value of paramount interest, however, is the high  $M_S$  value found in the co-doped material grown at higher Si cell temperatures. For the film grown at  $T_{Si} = 1100^\circ\text{C}$ ,  $M_S$  was in the range the 0.1  $\mu\text{m}$  thick GaGdN films, and at the higher cell temperature the saturation magnetization (Figure 4-10) was greater than any of the purely Gd-doped films. Looking at the magnetization vs. temperature curves, the decreasing gap between the field cooled and zero field cooled curves in Figure 4-10, show that the film may be nearing its  $T_C$ .

## **Summary**

In conclusion, GaGdN films have been grown which are ferromagnetic above room temperature and reject interfacial effects as the root of this behavior. The incorporation of Gd into the films is extremely low and results in highly resistive films. The ferromagnetic behavior of this material follows models of long range spin polarization. In addition, co-doping with Si shows larger overall magnetic signal and results in a conductive, n-type material.



Figure 4-1. RHEED image of 1 x 3 reconstruction seen in GaGdN:Si grown at  $T_{Si} = 1200^{\circ}C$ . Similar patterns were observed during GaGdN growth.

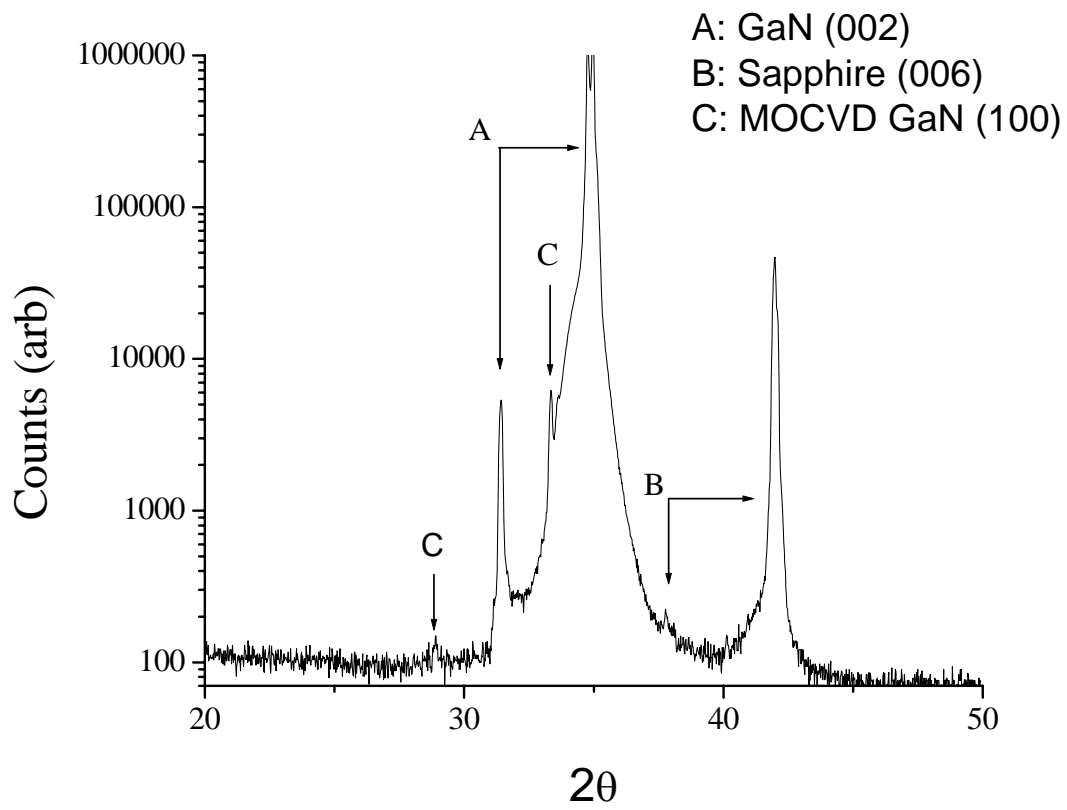


Figure 4-2. XRD of GaGdN is shown for a 1500Å thick film grown at  $T_{Gd} = 1050^{\circ}\text{C}$ .

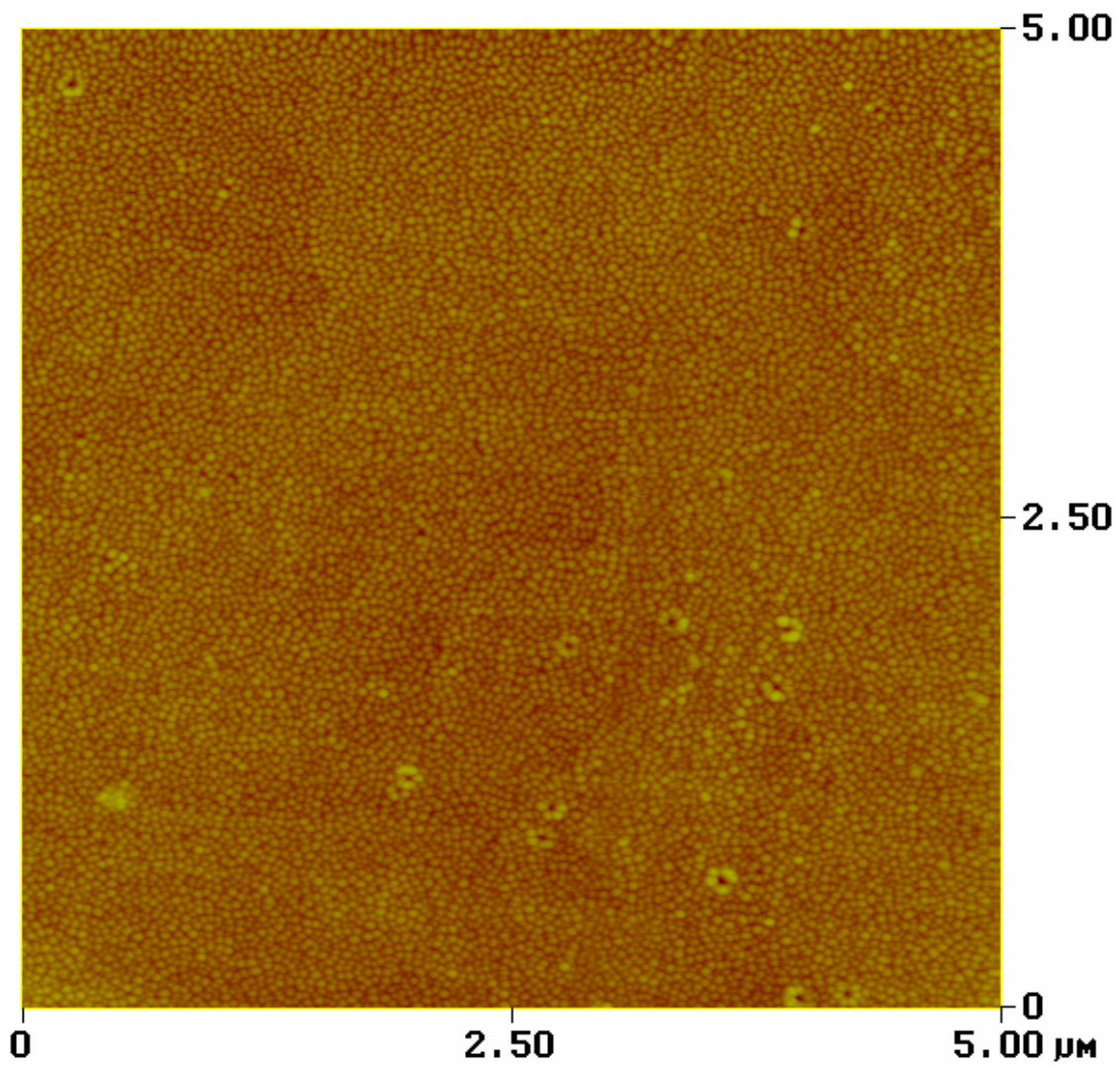


Figure 4-3. AFM image of GaGdN:Si shown for a 1500Å sample grown at  $T_{Si} = 1000^{\circ}\text{C}$  and  $T_{Gd} = 1050^{\circ}\text{C}$ . The rms roughness of this sample was 1.6 nm.

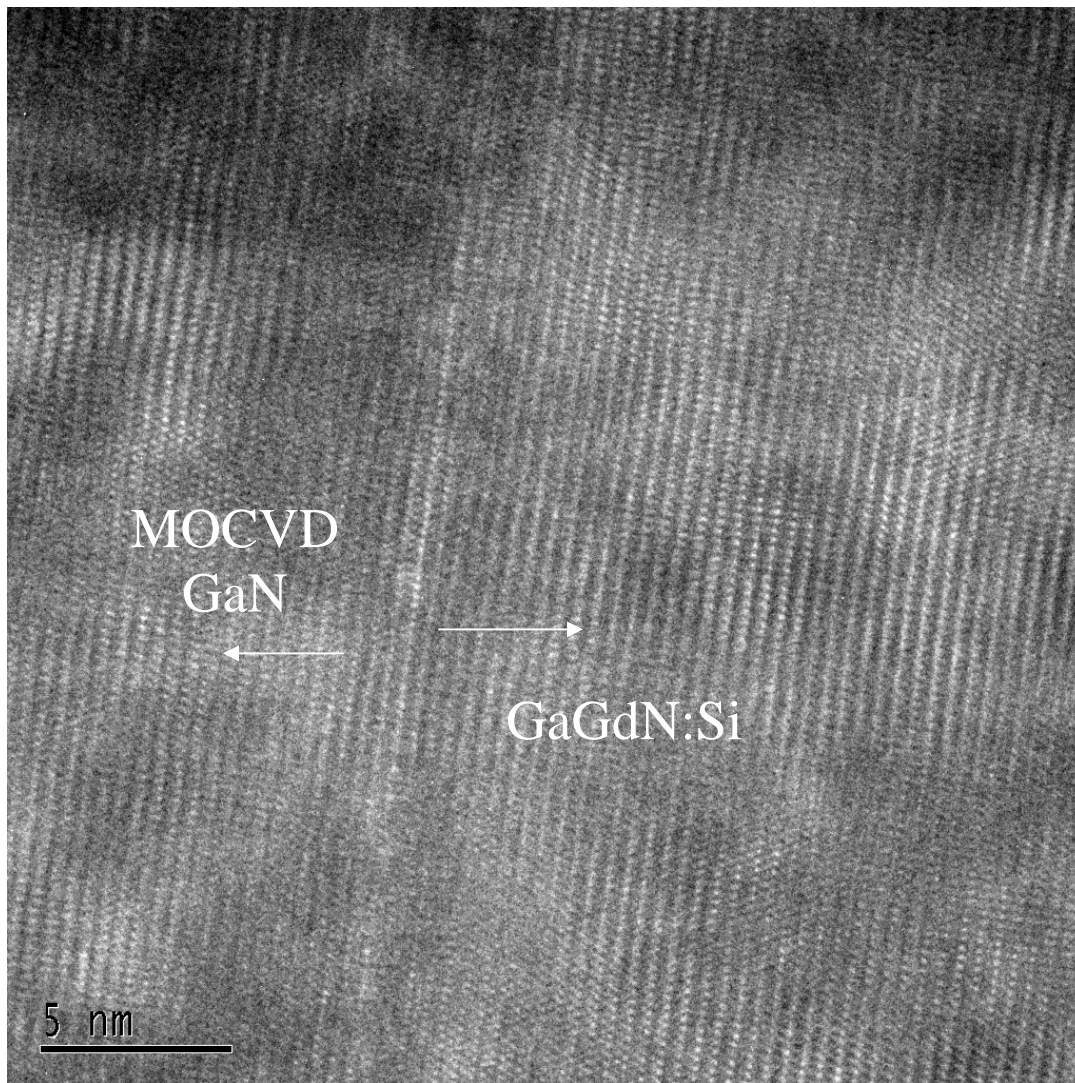


Figure 4-4. TEM images of GaGdN:Si showing highly ordered lattices. The GaGdN:Si sample was grown to a thickness of  $1500\text{\AA}$  using  $T_{\text{Gd}} = 1050^\circ\text{C}$  and  $T_{\text{Si}} = 1200^\circ\text{C}$ .

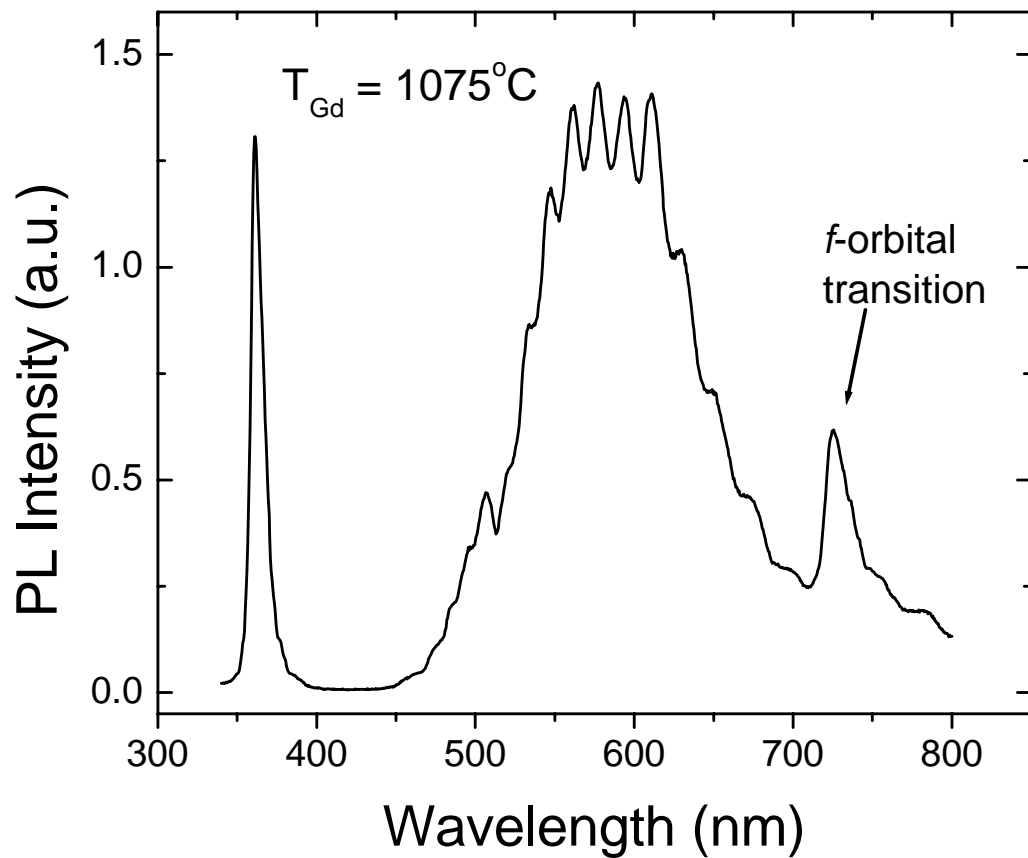


Figure 4-5. PL spectra of GaGdN grown to 1500Å at  $T_{\text{Gd}} = 1075^{\circ}\text{C}$ . The additional peak at 725 nm, or 1.7 eV, is attributed to Gd intra-f transitions.

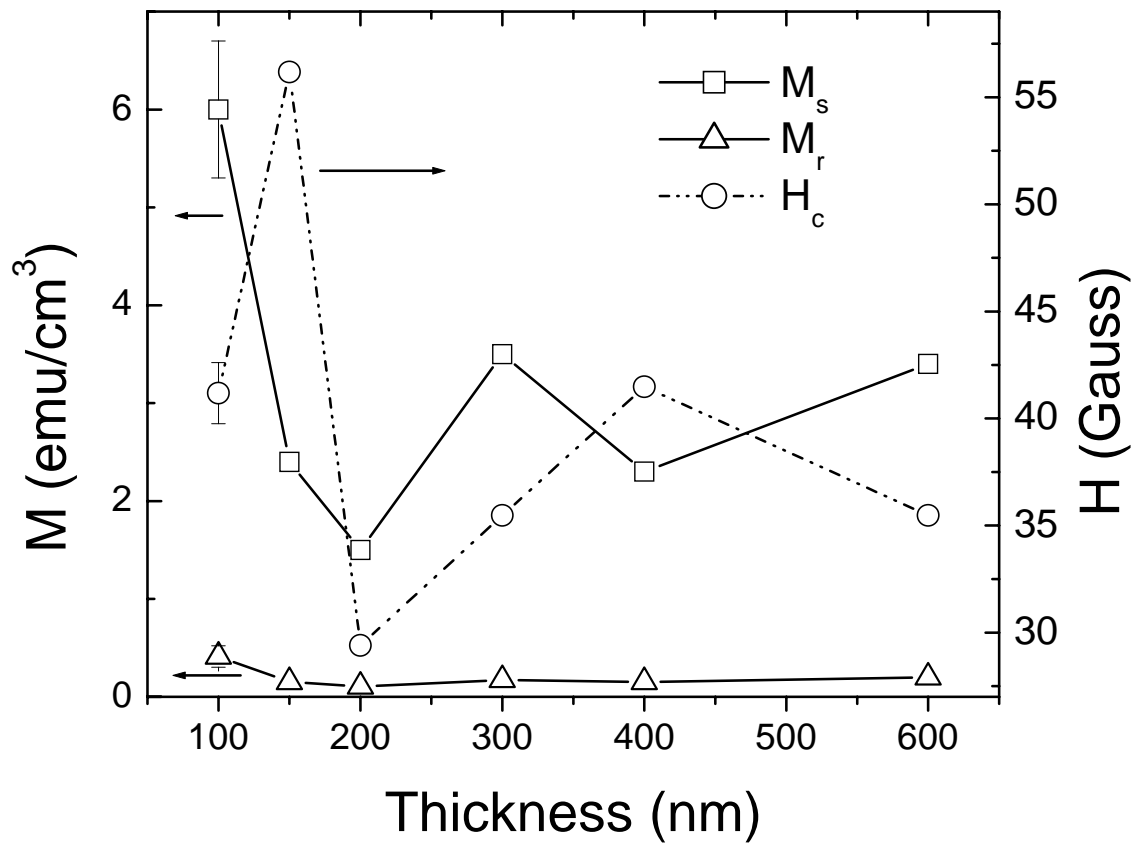


Figure 4-6. Estimated saturation magnetization and coercivity vs. GaGdN thickness shown.

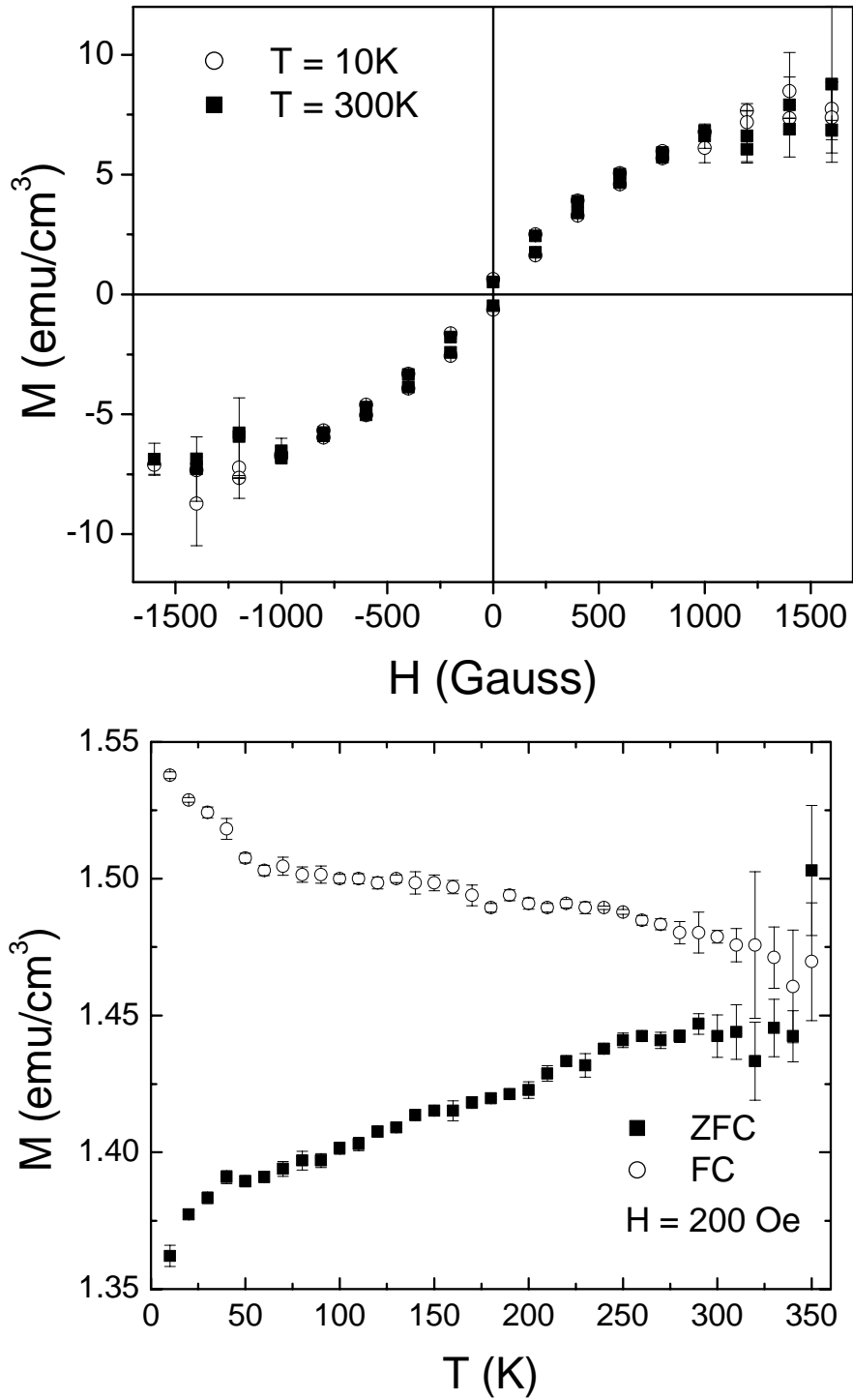


Figure 4-7. Magnetization vs. applied field taken at 10 and 300K shown at top. Bottom shows magnetization vs. temperature under a constant field of 200 Oe. Both curves represent a 1000Å thick GaGdN film grown at  $T_{\text{Gd}} = 1050^\circ\text{C}$ .

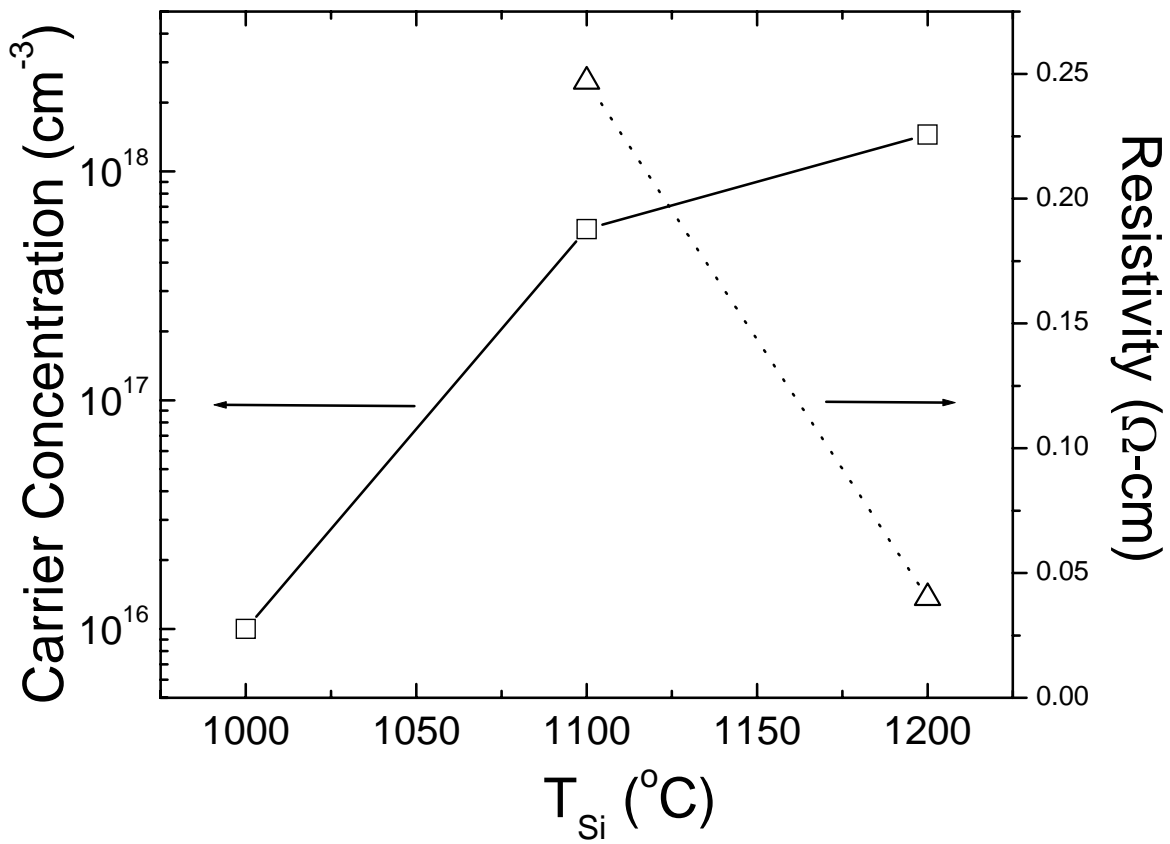


Figure 4-8. Electrical data as a function of Si cell temperature. At  $T_{Si} = 1000^\circ\text{C}$ , the carrier concentration was estimated to be  $10^{16}$  atom/ $\text{cm}^3$  and the resistivity was high.

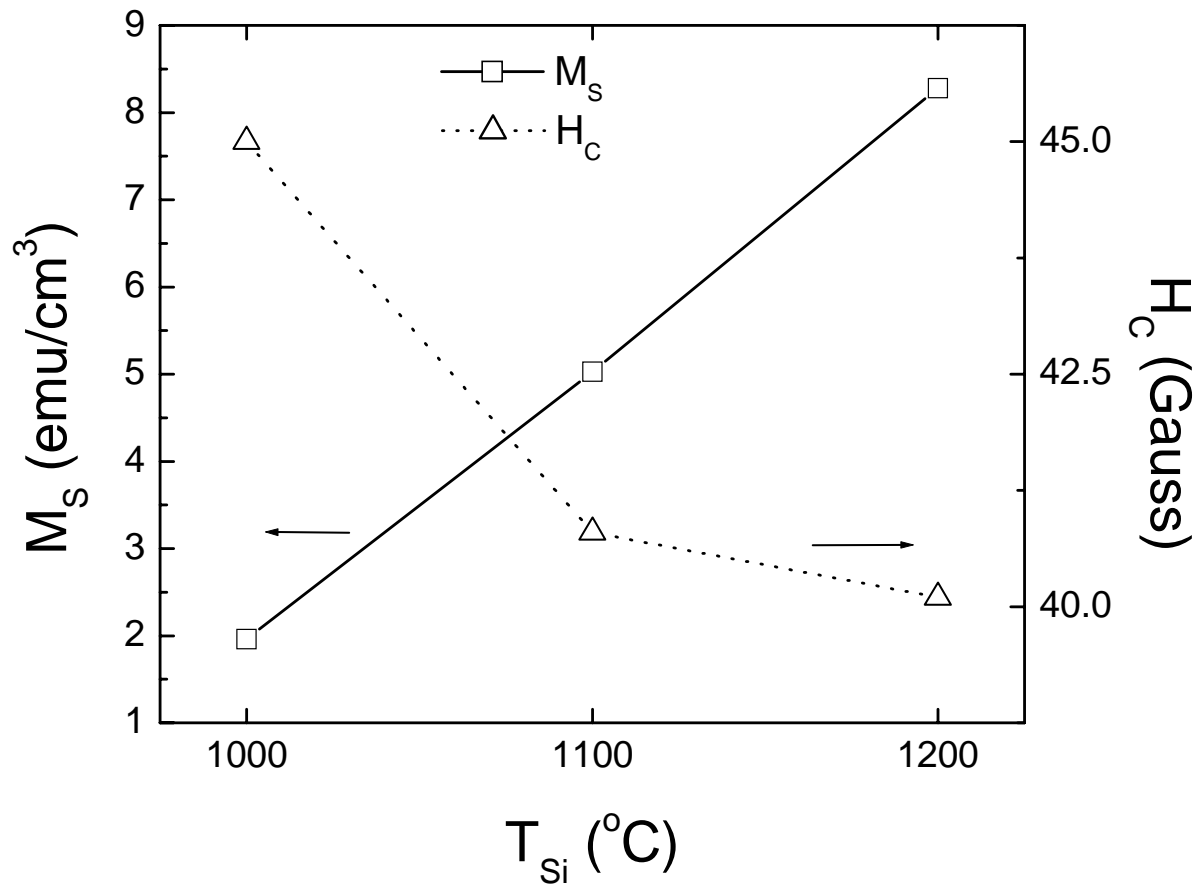


Figure 4-9. Estimated saturation magnetization and coercivity vs. Si cell temperature shown. Magnetization values were taken at 1000G during room temperature measurements.

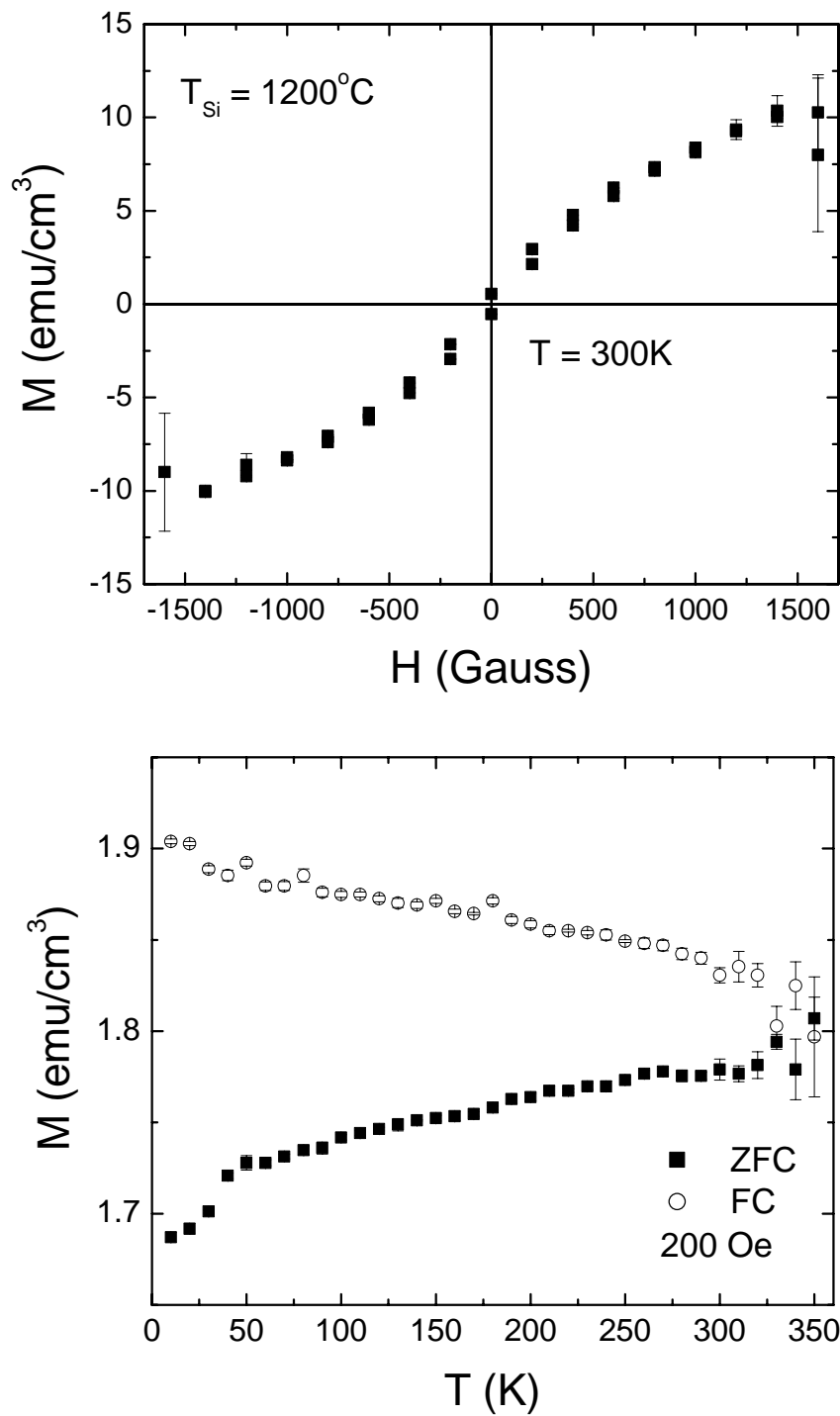


Figure 4-10. Magnetization vs. applied field taken at 300K for GaGdN:Si is shown at top. Bottom shows magnetization vs. temperature under a constant field of 200 Oe. Both curves represent a material grown at  $T_{\text{Si}} = 1200^\circ\text{C}$ .

## CHAPTER 5 EFFECTS OF RADIATION ON GALLIUM GADOLINIUM NITRIDE

Interest in III-Ns has rapidly increased as their unique abilities allow them to be used in applications requiring short wavelength optical emission or electronic operation at high powers or temperatures. The ability of III-N electronic devices to operate in harsh environments makes them attractive for use in space-based systems. However, outside the protective umbrella of the earth's atmosphere, high energy particle bombardment may cause significant degradation in device performance. The main culprit in this is high energy protons, which make up the majority of cosmic radiation, and are captured by the earth's magnetosphere forming the inner Van Allen belt. Although the majority of the belt lies outside most satellite orbits, a portion of the belt known as the South Atlantic anomaly dips to only 250 km above sea level off the coast of Brazil, posing a hazard for low orbit satellites. This effect is particularly severe in narrower gap semiconductor systems, and as a result has been shown to be responsible for reducing the useful lifetime of satellite systems. Since III-nitride systems, such as GaN, have higher displacement energy as an empirical function of their larger bonding energy, they are also more resistant to radiation damage.

The majority of radiation studies on GaN have focused on determining the nature of native defects in the lattice,<sup>59-61</sup> but a few device-based studies have also been completed.<sup>62-65</sup> Intentional exposure to a high energy proton beam has been shown to cause slight degradation of the light emitting capabilities of InGaN-based LEDs, along with a decrease in carrier concentration,<sup>62</sup> while lower energy protons have shown a similar trend with little change in the electrical properties.<sup>63</sup> These effects have been explained by the formation of new recombination centers and traps due to proton induced displacement damage. In addition, GaN-based HEMTs have also shown reduced performance in transconductance and threshold voltage after proton irradiation at high energies and

dosages (1.8 MeV at  $<10^{14}$  cm<sup>-2</sup> and 40 MeV protons at  $5 \times 10^9$  cm<sup>-2</sup>) which are most likely due to carrier removal and scattering by radiation-induced deep traps.<sup>64-66</sup> Optically, the effects of irradiation of GaN on band edge photoluminescence have been shown to be dependent on carrier type. Irradiation of p-GaN increases band edge luminescence, while the opposite effect is seen in n-GaN. This has been attributed to radiation assisted depletion of traps.<sup>67</sup>

There is also significant interest in the potential of ferromagnetic semiconducting materials in the technology of spintronics. The use of spin-based transport opens up the possibility of creating devices that are nonvolatile and which have increased processing speed, decreased power consumption, and increased integration density.<sup>6,68,69</sup> Within III-N materials, the addition of dopants such as Mn, Cr, and Gd in epitaxially grown III-N materials have resulted in dilute magnetic semiconductors exhibiting room temperature ferromagnetism.<sup>19,27,30,34-36,45,70,71</sup> As work progresses on achieving spintronic devices, it is important to study the effects of radiation on DMS materials. In addition, understanding the effect of particle irradiation on magnetic behavior may help to shed light on the mechanisms responsible for the magnetic ordering observed in these materials. In this chapter, the effects of high energy (>10 MeV) proton irradiation on the magnetic and optical properties of some DMS materials, namely GaCrN and GaGdN, will be discussed.

### **Experimental Procedure**

GaCrN and GaGdN were grown by gas source molecular beam epitaxy (GSMBE) on commercially available GaN substrates. The films were grown at a substrate temperature of 700°C as set by the thermocouple and under a nitrogen flow rate of 1.6 sccm. The cell temperature of the Ga ( $T_{\text{Ga}}$ ) was 785°C, while the dopant cell temperatures were at 1075°C and 990°C for Gd and Cr, respectively. The films were grown at a rate of 100 nm/hour to thicknesses of 1500Å. RHEED patterns obtained near the end of the growth were spotty, indicative of signs of surface roughening. Besides choice of transition metal dopant, these materials also differed in their dopant concentration. The Cr content was approximately 3 at%, while the Gd was drastically lower at less than 1 at%, and

was estimated to be on the order of  $10^{16}$  atom/cm<sup>3</sup>. These films were then irradiated with 10 and 40 MeV protons at a fluence of  $5 \times 10^9$  cm<sup>-2</sup> at the Texas A&M Cyclotron. This flux was chosen to simulate the total radiation gathered by 10 years in space. At these energies, the projected range of the protons ( $> 40$   $\mu$ m) is much greater than the thickness of the epitaxial films, so they are expected to traverse into the substrate. The samples were also annealed under N<sub>2</sub> plasma within the MBE chamber after irradiation to determine whether the materials would recover from irradiation damage.

Photoluminescence (PL) spectra at room temperature were taken before and after radiation using a HeCd excitation source. Magnetic behavior of the material was determined using a Quantum Design Magnetic Properties Measurement System superconducting quantum interference device (SQUID) magnetometer. To facilitate comparison between the films, background effects were subtracted out and the data was further normalized to volume. All measurements were performed with the applied field parallel to the sample surface.

### **Optical Effects**

The PL spectra of the as grown films are shown in Figures 5-1 for GaCrN and 5-2 for GaGdN. These spectra are similar to undoped MBE GaN samples, with a broad yellow luminescence band at 2.2 eV and band edge transitions between 3.4 and 3.45 eV. The only other notable feature was an extra peak at about 1.7 eV in the GaGdN spectra. Zhou et al. saw a similar peak for GaGdN attributed to f level transitions, only the entire spectra was blue shifted, perhaps from the larger concentration of Gd (6%) used in that study.<sup>72</sup> In addition, the GaGdN signal was much larger than the GaCrN, probably due to the higher crystal quality of the GaGdN. Irradiation dampened the emission signal of the irradiated samples from that of the as grown films. After irradiation, the emission from the band edge decreased with increasing irradiation energy for both materials along with a slight red shift. GaCrN showed a less marked change in band edge emission than the GaGdN. At the 10 MeV exposure level, the GaGdN band edge emission was cut in half, falling even lower

after the 40 MeV exposure. These results are illustrated in the plot of photon energy and band edge luminescence normalized to as grown values (Figure 5-3). In the yellow luminescence band, the GaCrN followed the same trend as in the band edge, while the defect band of GaGdN showed a stronger luminescence after 40 MeV than after 10 MeV. This is the same response as has been reported in n- and u-GaN.<sup>67</sup> The much larger Cr concentration, which forms an impurity band, may be the reason GaCrN is less sensitive to irradiation than GaGdN.

### **Magnetic Effects**

A summary of the magnetic saturation of the films is contained in Table 5-1. After irradiation, the GaCrN films show uniform degradation in magnetic saturation, dropping to half of the original value, illustrated in Figure 5-4. The GaGdN films also decline, primarily at 40 MeV where signal is only about 17% of the as grown value (Figure 5-5). This contrast is further illustrated in the hysteresis loops for GaGdN before and after exposure to 40 MeV shown in Figure 5-6. Representative loops for GaCrN are shown in Figure 5-7.

After undergoing a 30 minute anneal at 500°C under nitrogen plasma, the irradiated films show a drastic recovery in magnetic saturation, becoming slightly larger than the as grown values (Figures 5-4 and 5-5). To illustrate the largest change, the hysteresis loops for GaGdN exposed to 40 MeV before and after annealing are shown in Figure 5-8. A similar magnitude improvement in magnetization is also observed after annealing for all samples except the non-irradiated GaGdN. For all samples, the remnant magnetization values of the annealed samples are slightly larger, while the coercivities of the annealed samples are slightly reduced. Examining the magnetization vs. temperature zero field cooled and field cooled traces (Figures 5-9 and 5-10), also demonstrates the increase in magnetization from annealing the irradiated samples. Figure 5-9 not only shows an increase in overall magnetization after annealing, but it also indicates that irradiation may be associated with a decrease in  $T_C$ , which is recovered by annealing. The as grown traces are not shown

in this figure, but they were comparable to the annealed values. The GaCrN traces also show improvement in  $T_C$  after annealing, which is illustrated in Figure 5-10.

### **Mechanism**

It is unlikely that the proton exposure is imparting sufficient energy to the lattice to create significant atom displacement. It is more likely that the radiation is emptying existing deep level traps, which then act as non-radiative recombination centers. The large increase in carrier concentration after radiation exposure also argues for depopulation of traps over creation of defects. The cause of magnetization in DMS films like GaCrN and GaGdN has been explained by several theories, including localized polarization of the matrix by the magnetic ions.<sup>46-54</sup> The depopulation of a deep trap within the material can rationalize the experimental results, as the additional competition for electrons would reduce the number of electrons, and their spins, that could be incorporated into the polarization field of Gd or Cr atoms, thus reducing the overall magnetic moment of the samples. In this case, the dramatically lower Gd concentration would make the GaGdN material more susceptible to this effect than GaCrN. An additional theory suggests the ferromagnetism of GaGdN is electron stabilized.<sup>56</sup> Following this theory, additional competition for electrons by the depopulated traps would make GaGdN more sensitive to radiation. The response to annealing shows that this is a recoverable process, and that a great deal of energy is not required to remove the electrons from their traps. With this reasoning, increasing the energy of the protons should correspond to a decrease in magnetization and emission, which fits the experimental data.

### **Summary**

In conclusion, GaCrN and GaGdN films have been irradiated with high energy protons causing a decrease in both magnetic signal and PL emission which was much more drastic in the case of GaGdN. Further annealing allowed the magnetization to recover to original levels. Irradiation damage in the form of depopulation of deep traps has been reasoned to explain these behaviors.

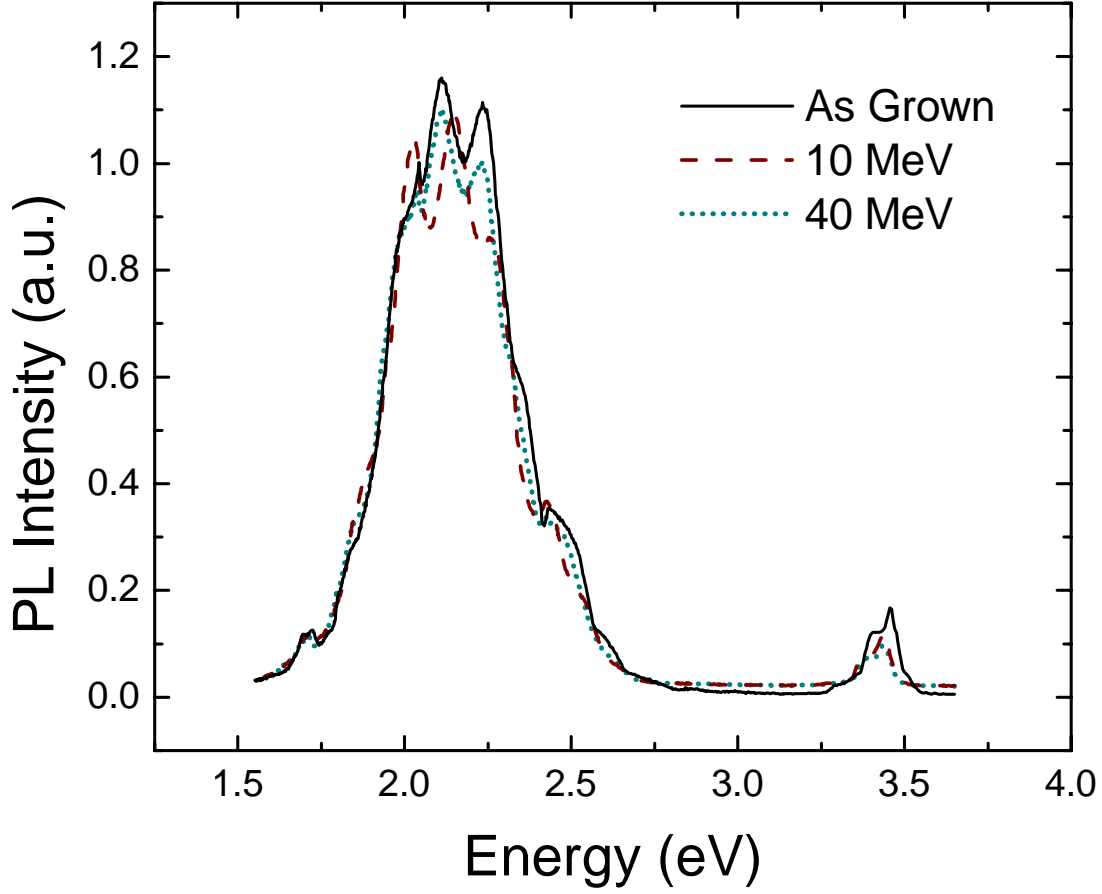


Figure 5-1. PL spectra of GaCrN after exposure to 0, 10, and 40 MeV protons.

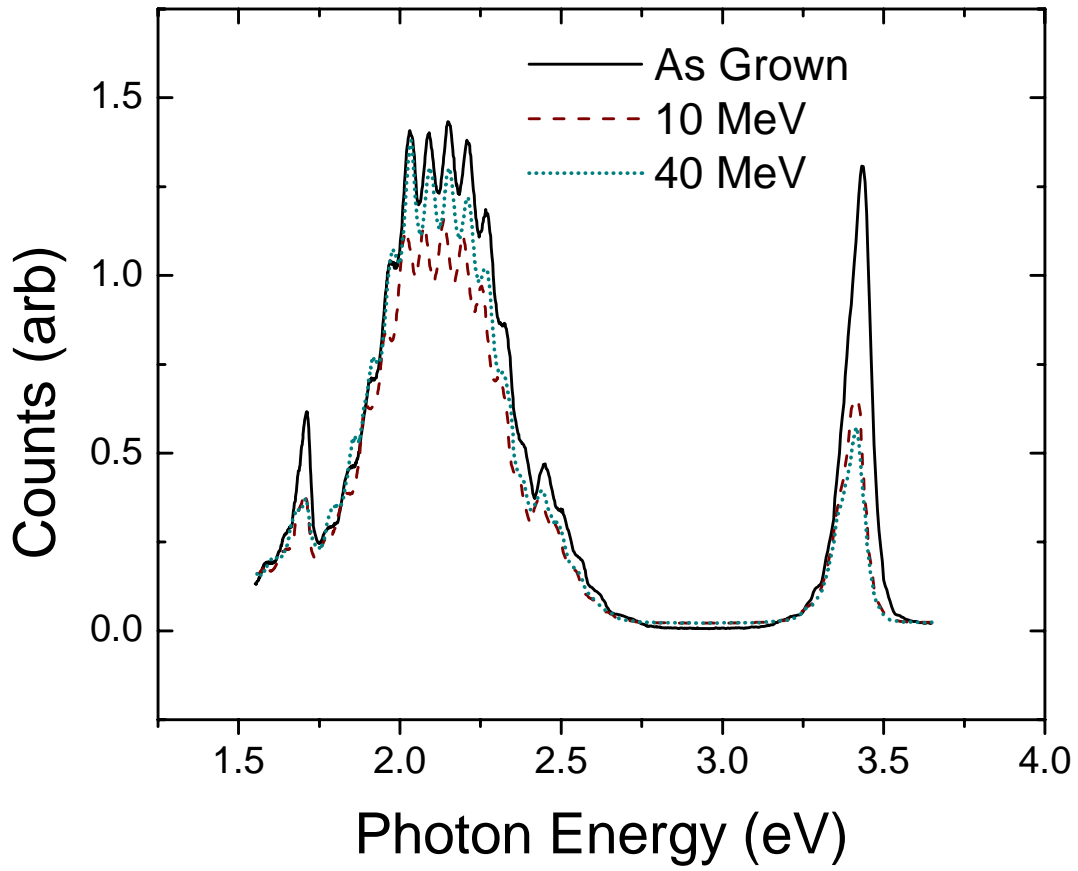


Figure 5-2. PL spectra of GaGdN after exposure to 0, 10, and 40 MeV protons.

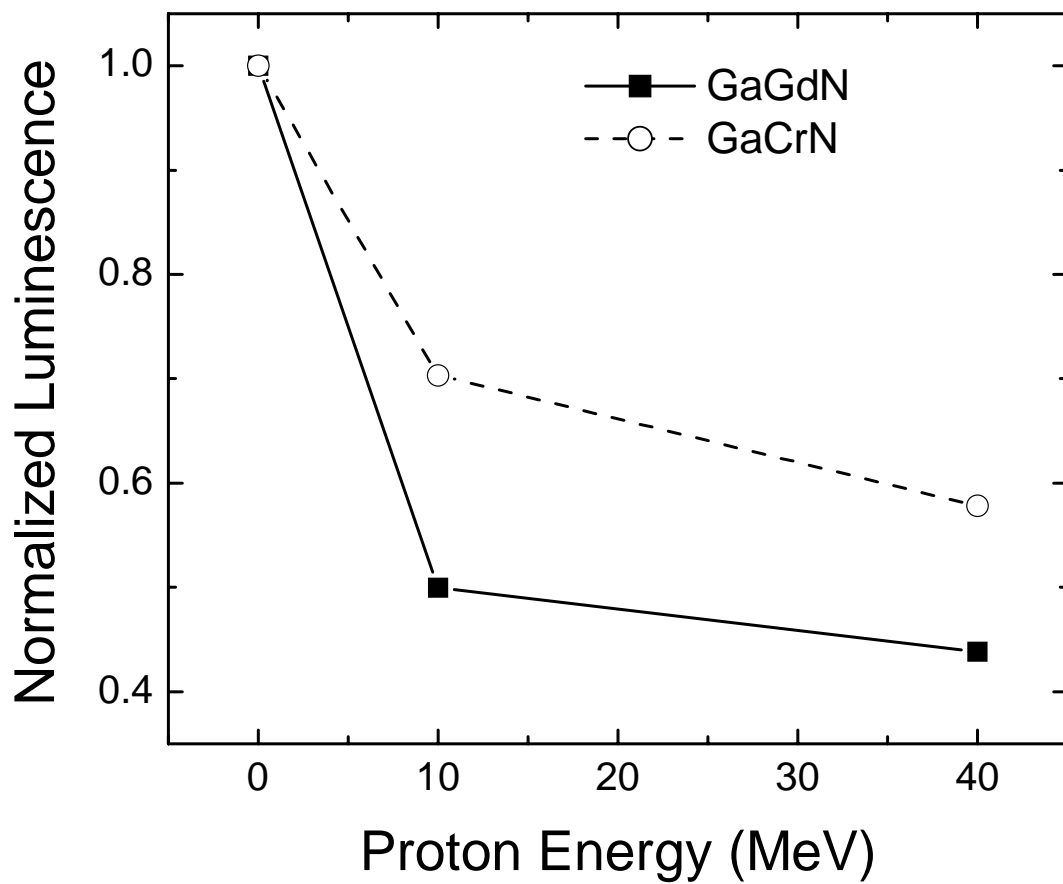


Figure 5-3. Band edge luminescence normalized to as grown values vs. photon exposure energy is shown. The normalizing values were 1.3074 for GaGdN and 0.1674 for GaCrN.

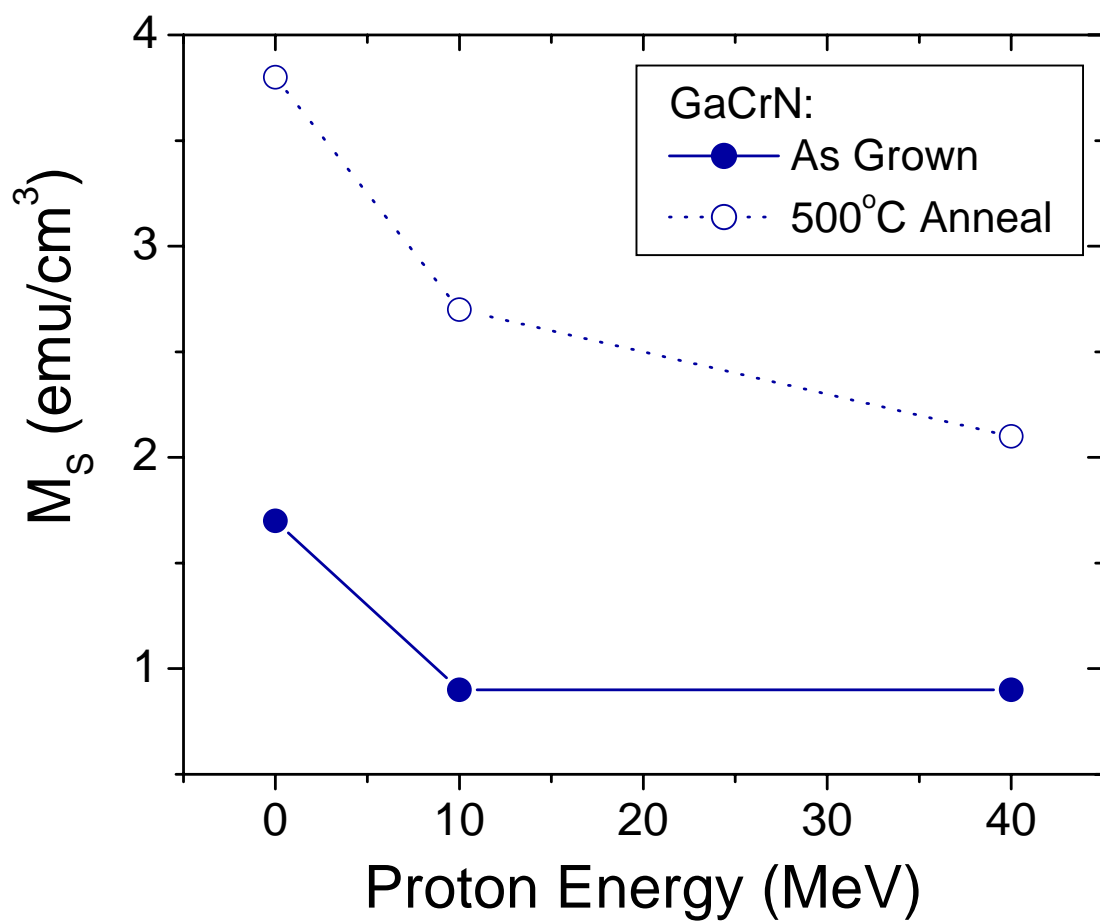


Figure 5-4. Saturation magnetization vs. proton energy shown for GaCrN both before and after plasma annealing at 500°C. Saturation magnetization values were taken at 1000 G from room temperature magnetization vs. applied field curves.

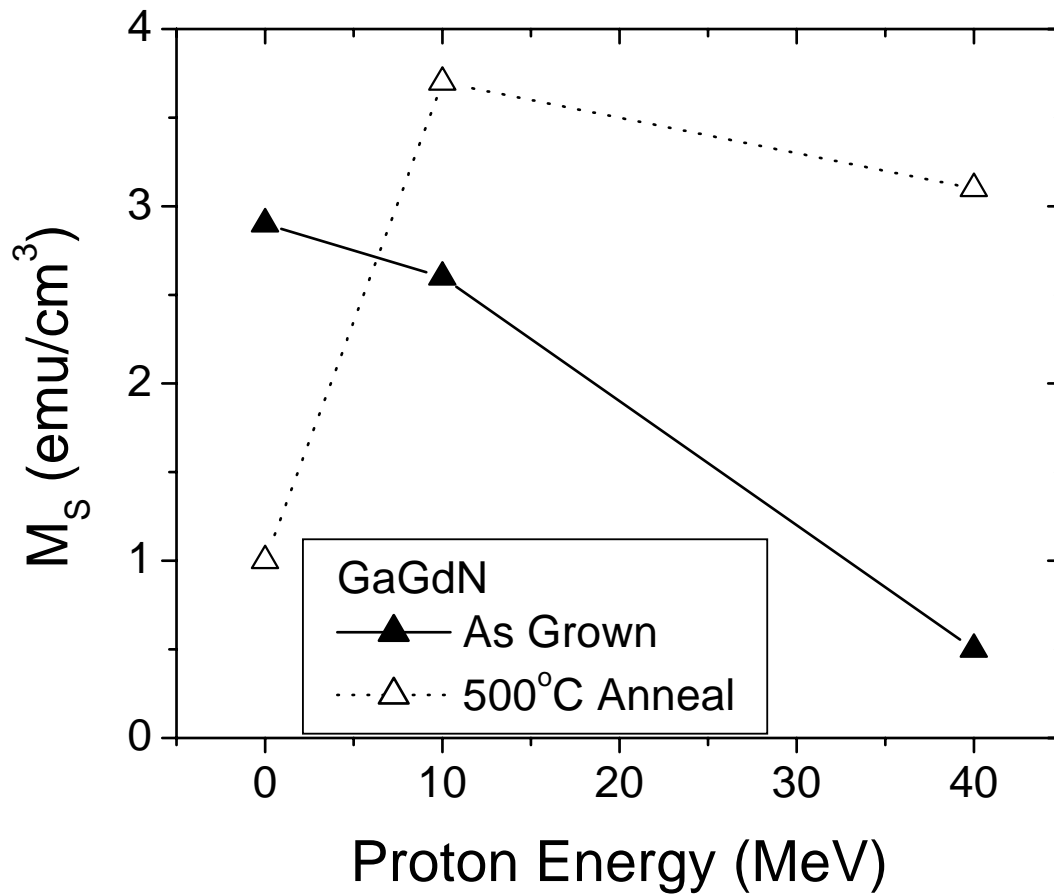


Figure 5-5. Saturation magnetization vs. proton energy shown for GaGdN both before and after plasma annealing at 500°C. Saturation magnetization values were taken at 1000 G from room temperature magnetization vs. applied field curves.

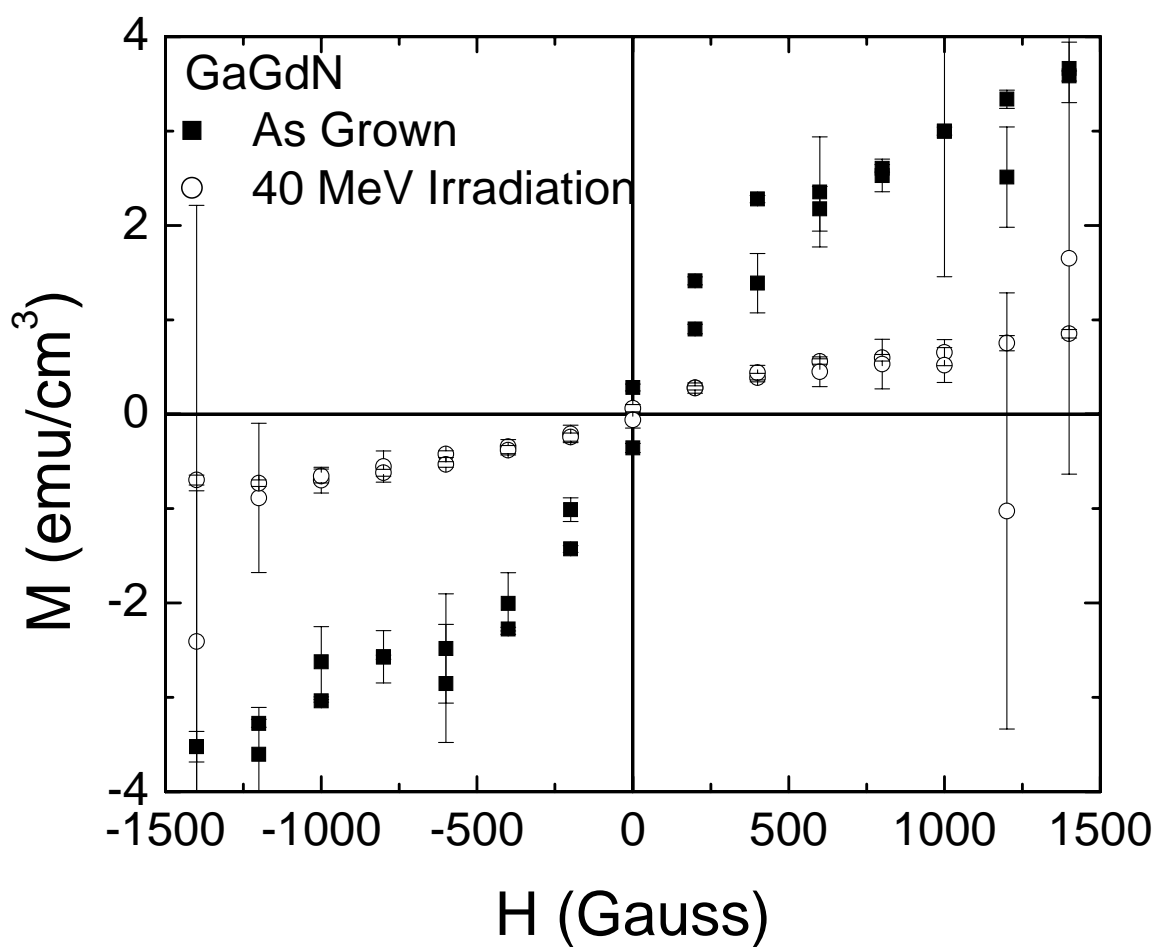


Figure 5-6. Hysteresis loops for as grown and irradiated GaGdN samples. Curves were taken at 300K, and saturation magnetization was estimated at 1000 G.

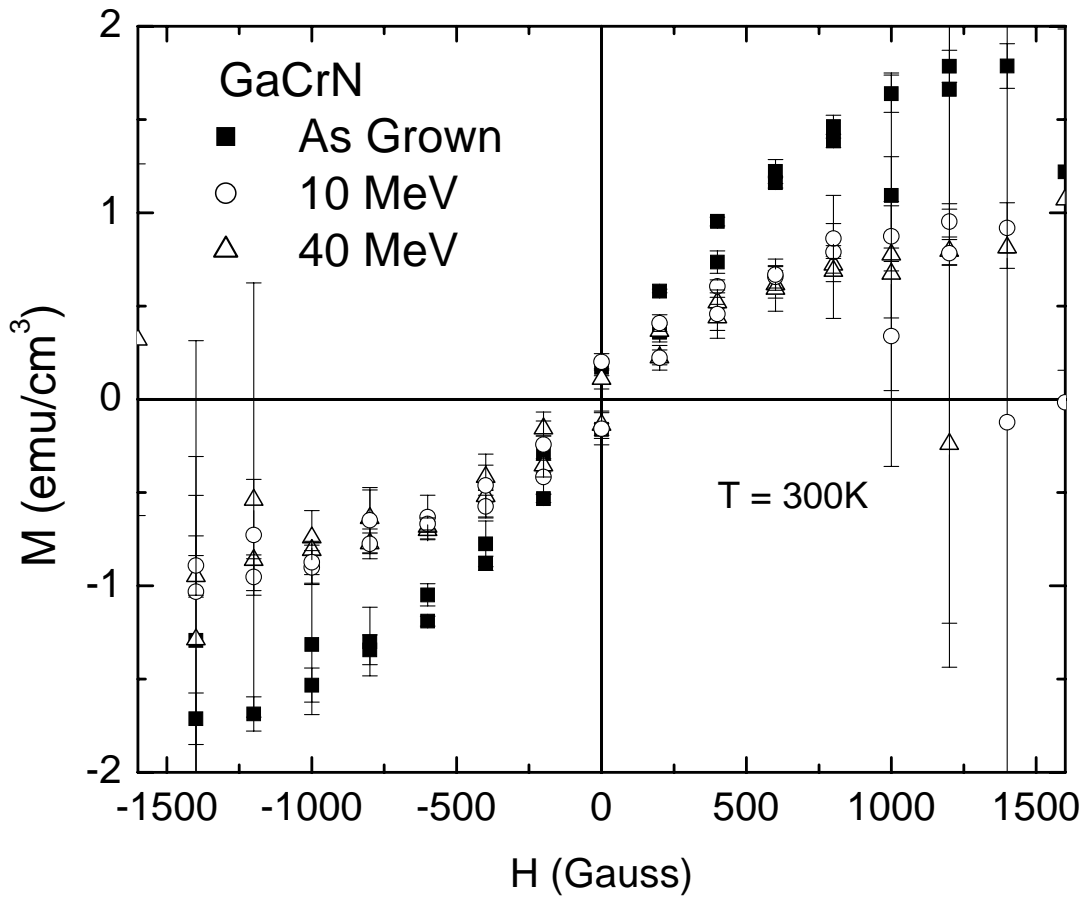


Figure 5-7. Hysteresis loops for as grown and irradiated GaCrN samples. Curves were taken at 300K, and saturation magnetization was estimated at 1000 G.

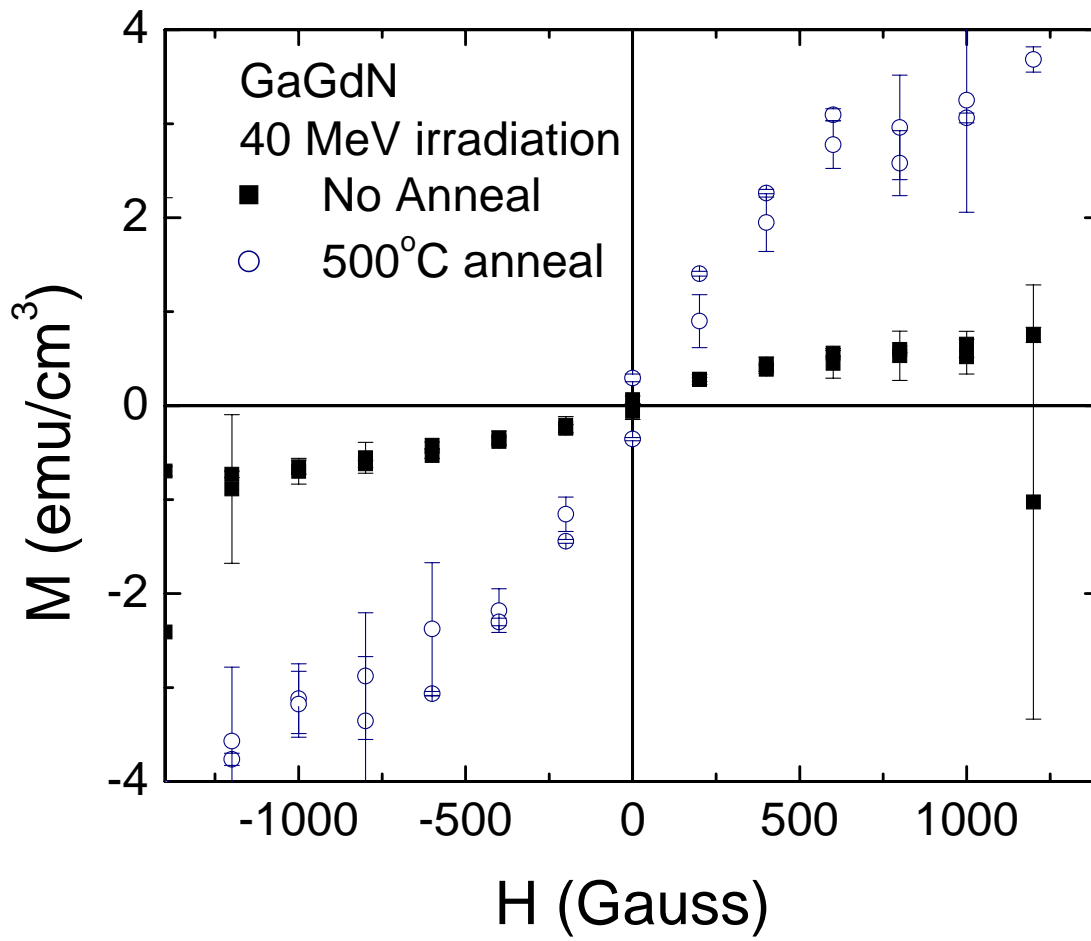


Figure 5-8. Magnetization vs. applied field curves taken at 300K are shown for pre- and post-N<sub>2</sub> plasma annealing for GaGdN irradiated with 40 MeV protons.

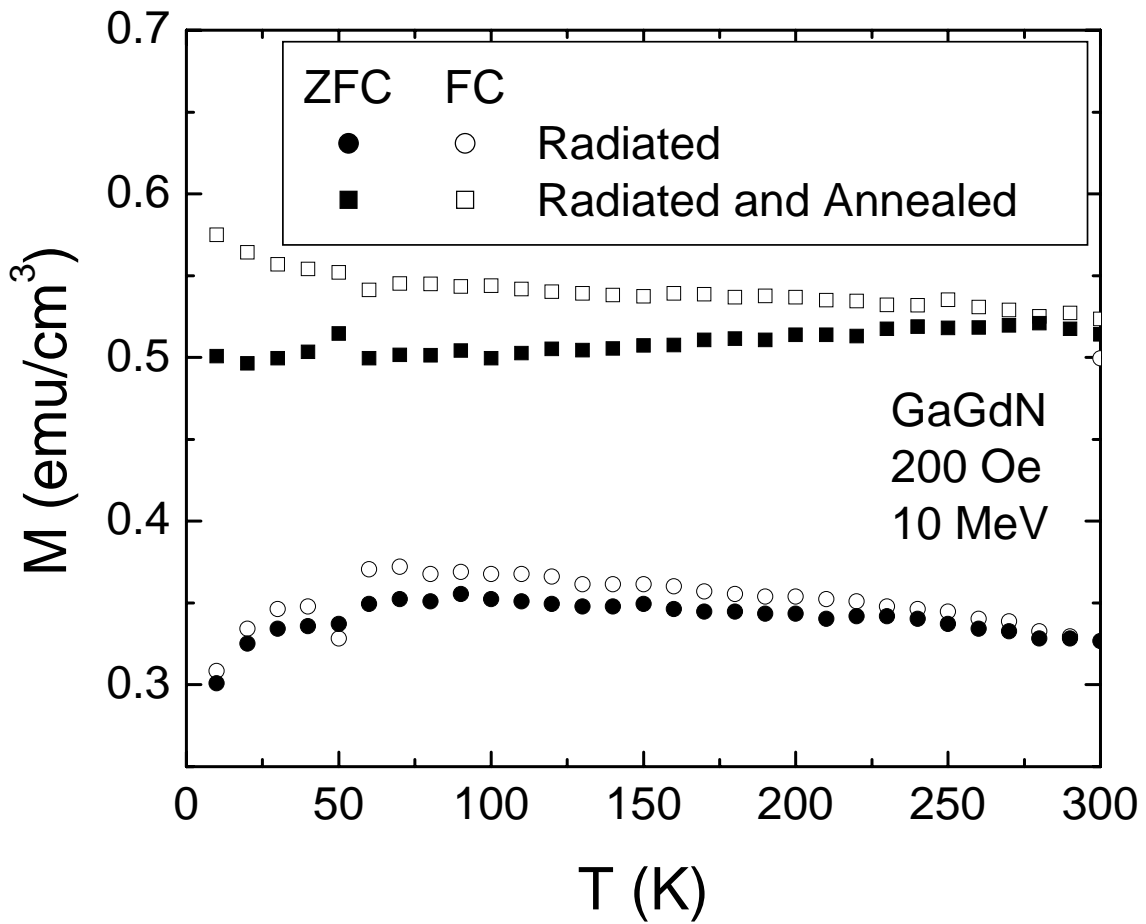


Figure 5-9. Magnetization vs. temperature curves showing zero field-cooled and field-cooled traces for GaGdN exposed to 10 MeV before and after annealing. Traces were taken at an applied field of 200 Oe. Irradiated traces are shown as circles, and those further annealed at 500°C are denoted as squares. The error in the measurements was rather uniform, with an average value around 0.33 emu/cm<sup>3</sup>.

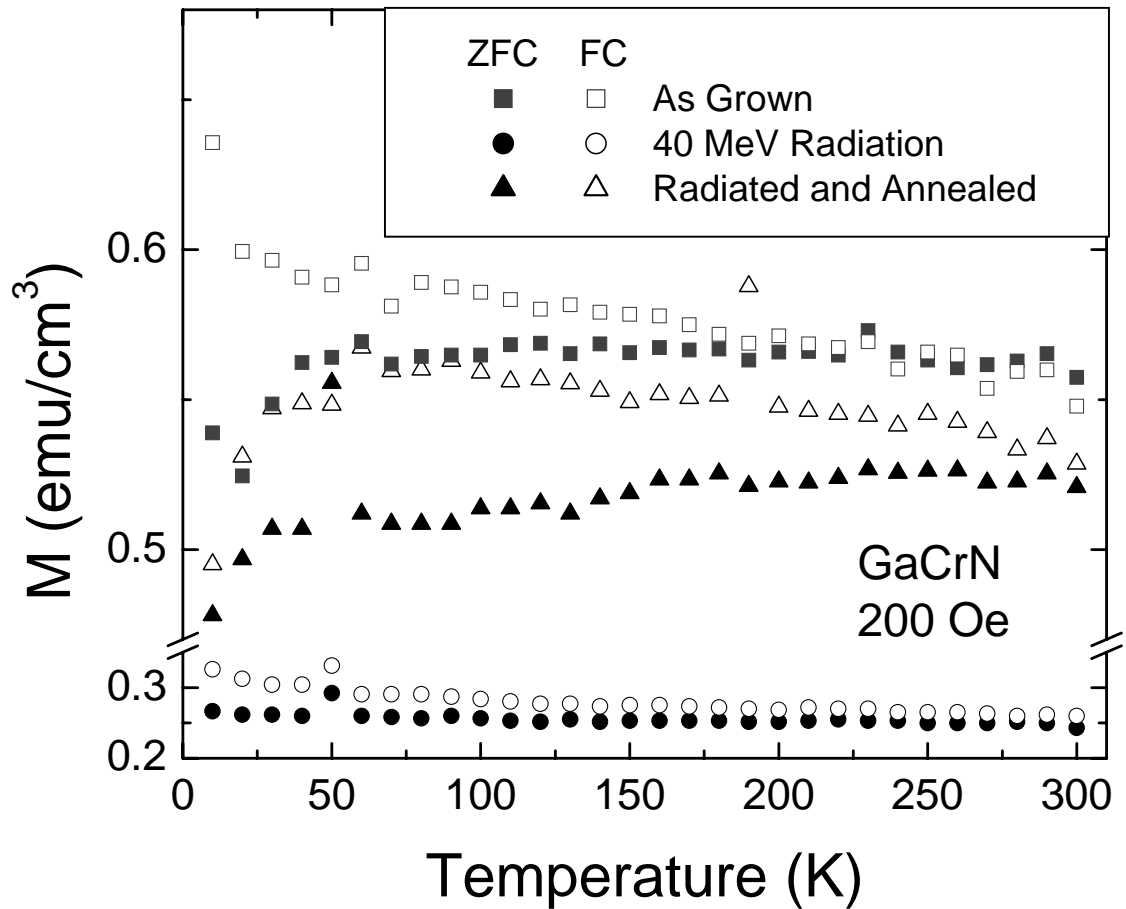


Figure 5-10. Magnetization vs. temperature curves showing zero field-cooled and field-cooled traces for as grown, irradiated, and annealed GaCrN. Zero field-cooled traces are shown by filled in symbols, while field-cooled data are open symbols. As grown traces are squares, irradiated are circles, and annealed are triangles.

## CHAPTER 6 THERMAL ANNEALING EFFECTS ON GALLIUM GADOLINIUM NITRIDE BASED FILMS

In processing nitride based semiconductors, thermal annealing at temperatures above 700°C is often required to activate ohmic contacts. Of the transition metal-doped GaN, GaMnN has been shown to be thermally unstable at these temperatures without additional oxygen codoping, while GaCrN was stable through 700°C.<sup>17,27</sup> Studying the behavior of these materials after thermal stress may help understand the process giving rise to ferromagnetism along with revealing promising material for device usage. The response of GaGdN to thermal annealing under nitrogen ambient and plasma, oxygen plasma, and ultra-violet ozone exposure will be presented in this chapter.

### **Experimental Procedure**

The thermocouple measured cell temperatures were 785, 1000, and 1100°C for Ga, Gd, and Si, respectively. The substrate temperature was held at 630°C while nitrogen flowed at rates between 1.4 and 2.0 sccm. The films were grown under 2D to 2D/3D reflection high energy electron diffraction (RHEED) patterns to thicknesses of 1000Å for GaGdN and 1500Å for GaGdN:Si. In addition, the RHEED showed a 1 x 3 pattern.

Magnetic measurements were taken up to room temperature with a Quantum Design Magnetic Properties Measurement System superconducting quantum interference device (SQUID) magnetometer. The magnetic field was applied parallel to the sample surface in all cases. The diamagnetic properties of the substrate and holder were subtracted out, and the data was further normalized to allow better comparisons between samples.

Annealing of the samples was investigated under various conditions. Rapid thermal annealing of both films was done under ambient nitrogen for 1 minute. Nitrogen and oxygen plasma annealing in MBE chambers for 30 minutes at substrate thermocouple temperatures from 500-900°C were also employed. Ultraviolet ozone exposure was carried out for 60 minutes after plasma annealing reduced the magnetic signal of the samples.

### **Rapid Thermal Annealing**

The thermal stability of the GaGdN and GaGdN:Si layers was investigated using a rapid thermal anneal (RTA) unit under nitrogen ambient for 1 minute. After annealing, the sample was then measured using the SQUID magnetometer and the saturation magnetization was normalized to the as grown values. These results are plotted in Figures 6-1 and 6-2 for GaGdN and GaGdN:Si, respectively. Although the magnetization of both films initially drops, even at 300°C for GaGdN, it then stabilizes at approximately 70 to 75% of the as grown value. This is vastly superior to that of GaMnN films annealed under similar conditions<sup>17</sup> and the slight drop is compensated by a larger overall saturation magnetization than that of annealed GaCrN films.<sup>27</sup> Further examination of the hysteresis loops reveals the coercivity of both films follows the same trend, shrinking slightly at low anneal temperatures followed by a rapid increase at higher ones (Figure 6-3). The addition of Si does seem to mitigate the effect of annealing, causing less loss of magnetization and preventing the coercivity from ballooning up to values over 100 Oe.

### **Nitrogen Incorporation and Annealing**

The original rapid anneal study had been conducted while under non-optimal conditions (under partial ambient air). The results of that investigation are plotted in Figure 6-4. Since some deterioration during annealing of GaN films has previously been attributed to loss of nitrogen, a nitrogen incorporation study was launched. By varying the nitrogen flow rate between growths of GaGdN, the incorporation of nitrogen was shown to have a large effect on the magnetization of the films. Figure 6-5 shows that the optimal magnetic signal occurred with a nitrogen flow rate of 1.8 sccm.

Annealing under nitrogen plasma for 30 minutes with a nitrogen flow rate of 1.3 sccm and substrate temperatures of 500 and 700°C was attempted to drive more nitrogen into the deficient sample grown at 1.4 sccm, resulting in an increase at 500°C. Further annealing at 700°C reversed the gains made by the previous anneal. The same study was attempted with the remainder of the GaGdN

samples (Figure 6-6). In both the optimal sample and the one grown under 1.6 sccm, annealing caused a decrease in magnetization. Normalizing these results to the as grown values of each sample (Figure 6-7) shows that plasma annealing the sample grown at 1.6 sccm fits the same trend and percentage of magnetization loss of the GaGdN annealed under a nitrogen RTA (Figure 6-1). Since the RTA annealed GaGdN sample was grown at the same nitrogen flow rate, this shows that loss of nitrogen is most likely not responsible for the magnetization loss seen in the thermal anneals.

### **Anneal Recovery**

Several methods were utilized to attempt a magnetic recovery of the annealed samples. In the radiation study from Chapter 5, it was observed that annealing under plasma effectively returned the sample magnetization to as grown levels. This effect was attempted by nitrogen plasma annealing at 500°C a sample that had undergone a 700°C RTA anneal. The only effect of further plasma annealing, even at a lower temperature than during that RTA anneal, was a further degradation of magnetic signal. These results are shown in Figure 6-8.

As it has been purported that oxygen levels may contribute to the ferromagnetic behavior in GaGdN, one sample was exposed to a rapid thermal anneal at 700°C, followed by annealing under oxygen plasma for 30 minutes at 500°C. This was just as unsuccessful at inducing magnetic recovery as annealing under nitrogen plasma. The hysteresis loops (Figure 6-9) show that annealing under oxygen plasma does not cause a recovery of magnetization.

In addition, a GaGdN sample was bombarded with ultra-violet ozone (UV-O<sub>3</sub>) for 60 minutes after reducing the magnetic signal by plasma annealing at 700°C. The plasma anneal in this case caused a slightly larger degradation than previous samples. The optical pumping of the sample by UV-O<sub>3</sub> did not result in any magnetic recovery (Figure 6-10). Studying this effect on a pristine GaGdN sample showed no real change in the magnetic properties of the film (Figure 6-11).

## Summary

In summary, thermal annealing and nitrogen incorporation influence the magnetization of GaGdN and GaGdN:Si. Samples grown with insufficient or overabundant levels of nitrogen are outliers in the general trend of decreasing magnetic strength with thermal annealing. The low magnetic ordering seen at low nitrogen levels can be attributed to an increased level of nitrogen vacancies, and may allow non-cation substitution sites for the Gd ions. At high nitrogen flow rates, the reduced magnetic signal most likely arises by a decrease in crystalline quality. The dependence of magnetic signal on optimal nitrogen incorporation is also supported by the drastic loss of signal when annealing samples under air. Since all attempts at annealing samples with sufficient nitrogen only resulted in decreasing magnetic signal, this trend may also account for the outlier of the annealed non-irradiated GaGdN found in the preceding irradiation study (Figure 5-5).

As for the mechanism involved, the energy imparted from annealing may act in a similar manner as that from radiation. For irradiation, it was suggested that high energy proton irradiation exposure caused depletion of a deep level trap, which in turn caused increased competition for free carriers, reducing the amount of electrons required to stabilize the ferromagnetism in this material. Thermal annealing does not act in the same manner, but may also be responsible for emptying traps within the films. If so, this may also account for the observed stabilization of magnetic properties with annealing by addition of silicon, by the addition of donor electrons.

GaGdN and GaGdN:Si still remain as viable options for device incorporation. Although they do show a decrease in magnetic strength with thermal annealing, it is only by 20-25%. As such, these films still exhibit higher magnetic signal than the previous thermally stable material (GaCrN), and have been tested to temperatures of 900°C, making them a reliable option for device processing.

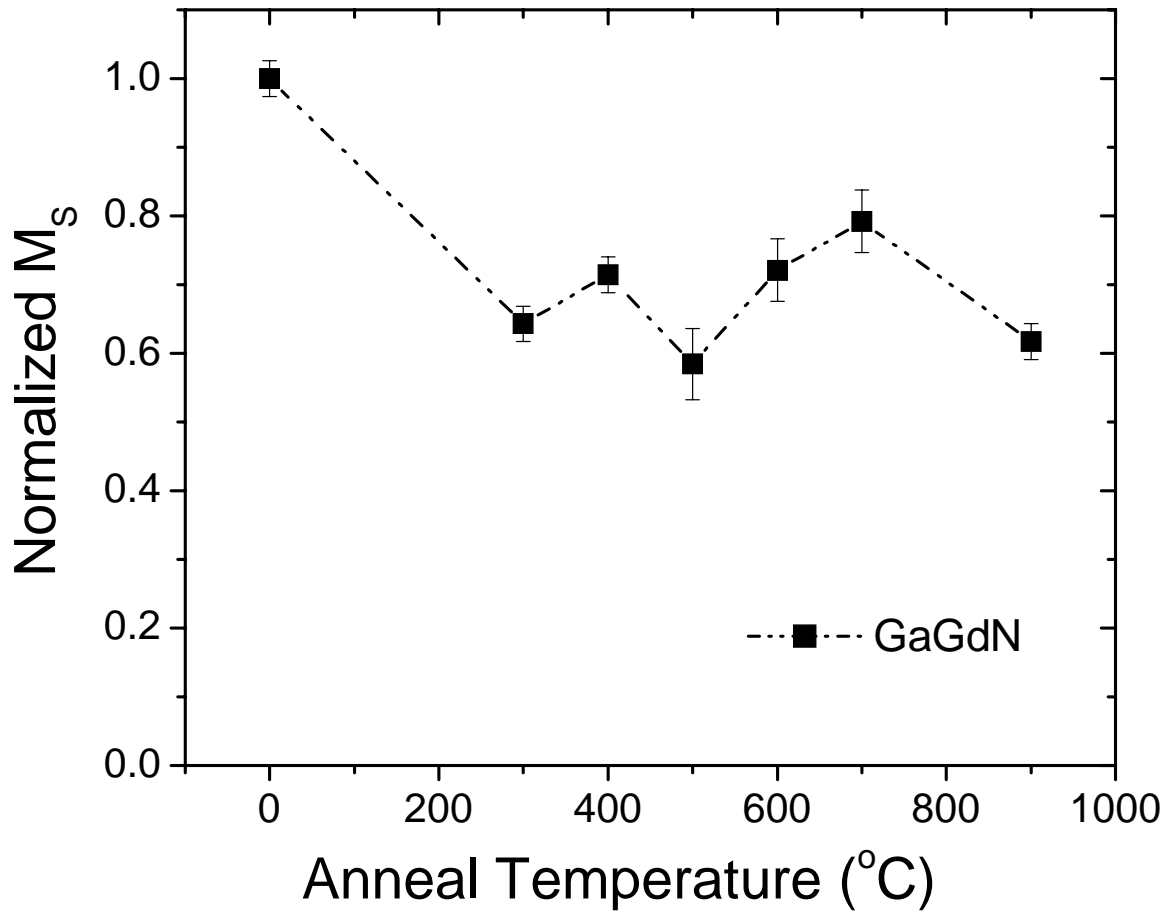


Figure 6-1. Normalized saturation magnetization of GaGdN plotted against RTA temperature. Saturation magnetization was estimated at 1000G from 300K hysteresis curves. The normalizing value for this data was  $7.7 \text{ emu/cm}^3$ .

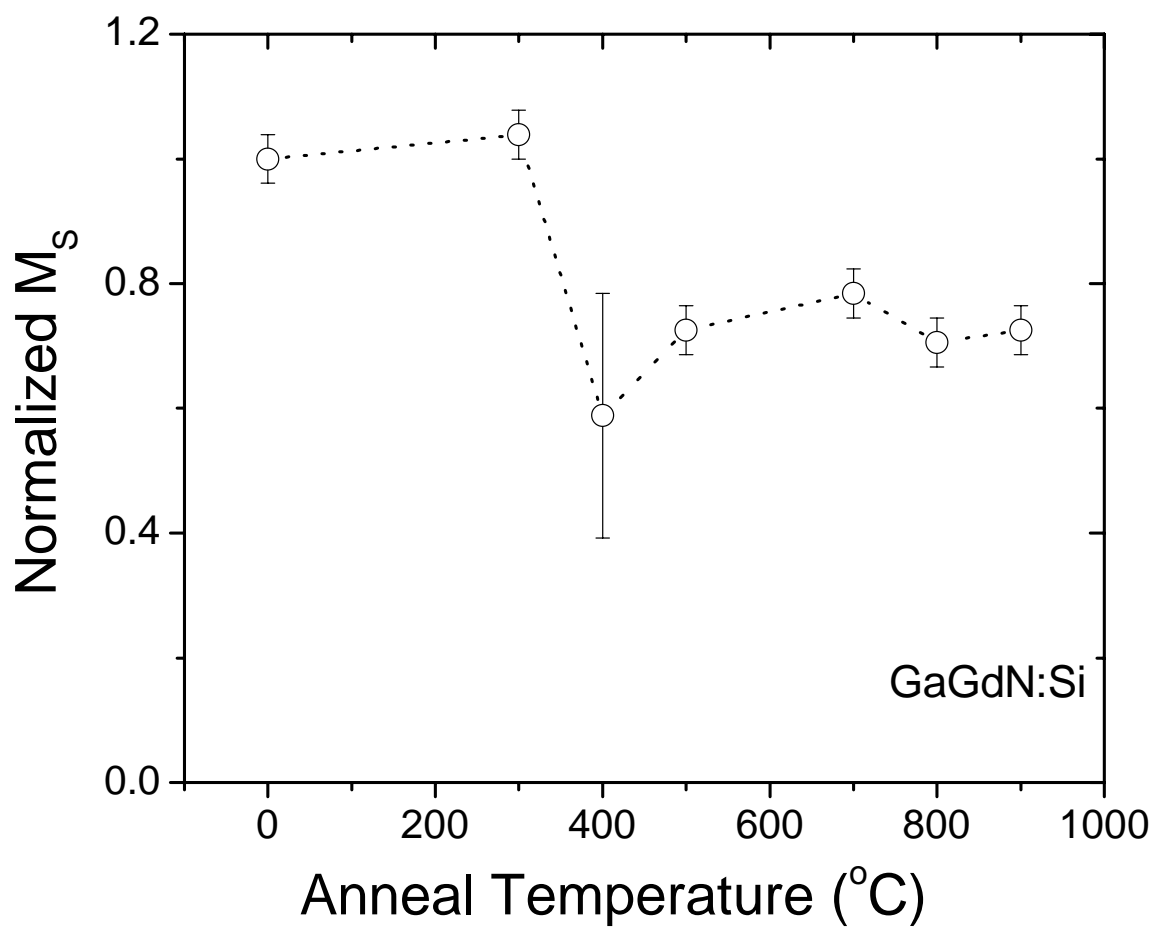


Figure 6-2. Normalized saturation magnetization of GaGdN:Si plotted against RTA temperature. Saturation magnetization was estimated at 1000G from 300K hysteresis curves. The normalizing value for this data was  $5.1 \text{ emu/cm}^3$ .

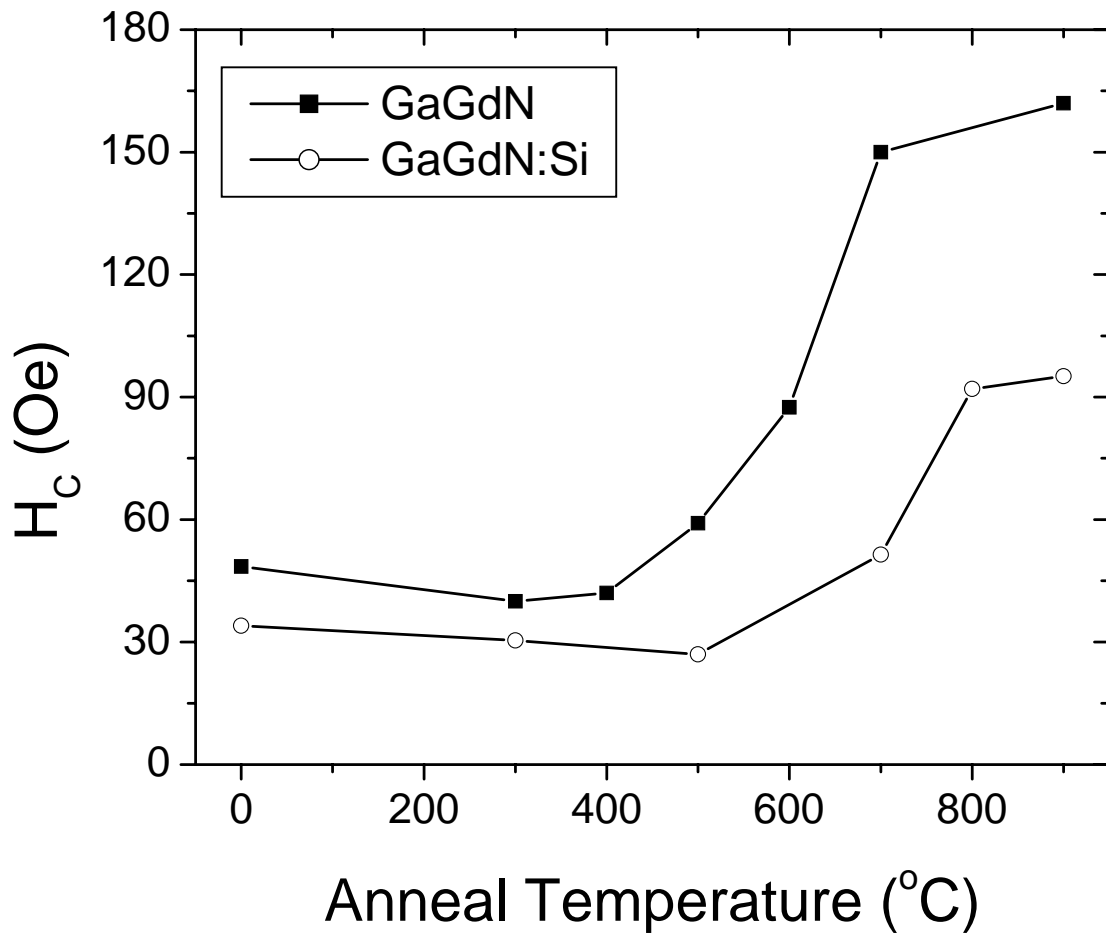


Figure 6-3. Anneal temperature versus coercivity values shown. Values taken from hysteresis curves at 300K.

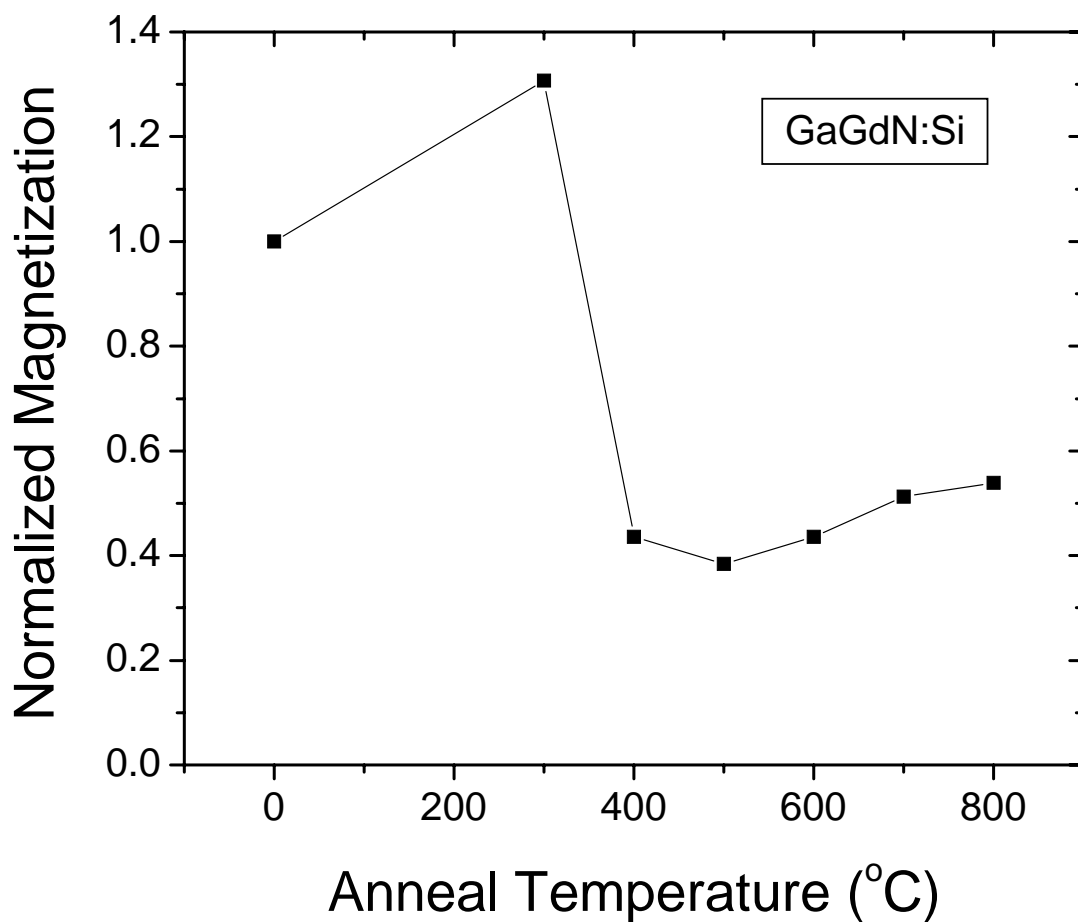


Figure 6-4. Normalized saturation magnetization of GaGdN:Si plotted against RTA temperature when under partial air. Saturation magnetization was estimated at 1000G from 300K hysteresis curves. The normalizing value for these values was  $3.9 \text{ emu/cm}^3$ .

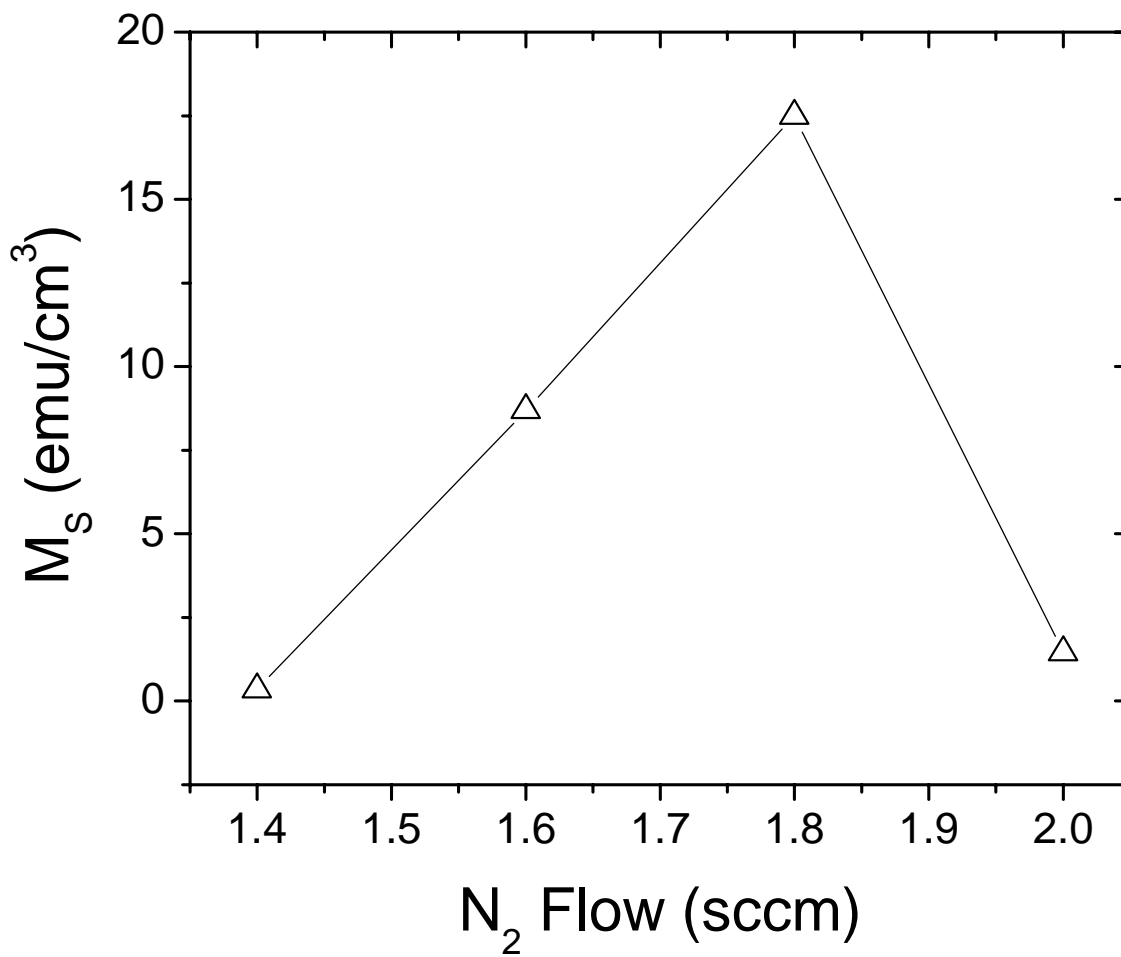


Figure 6-5. Saturation magnetization plotted against nitrogen flow rate during GaGdN growth.

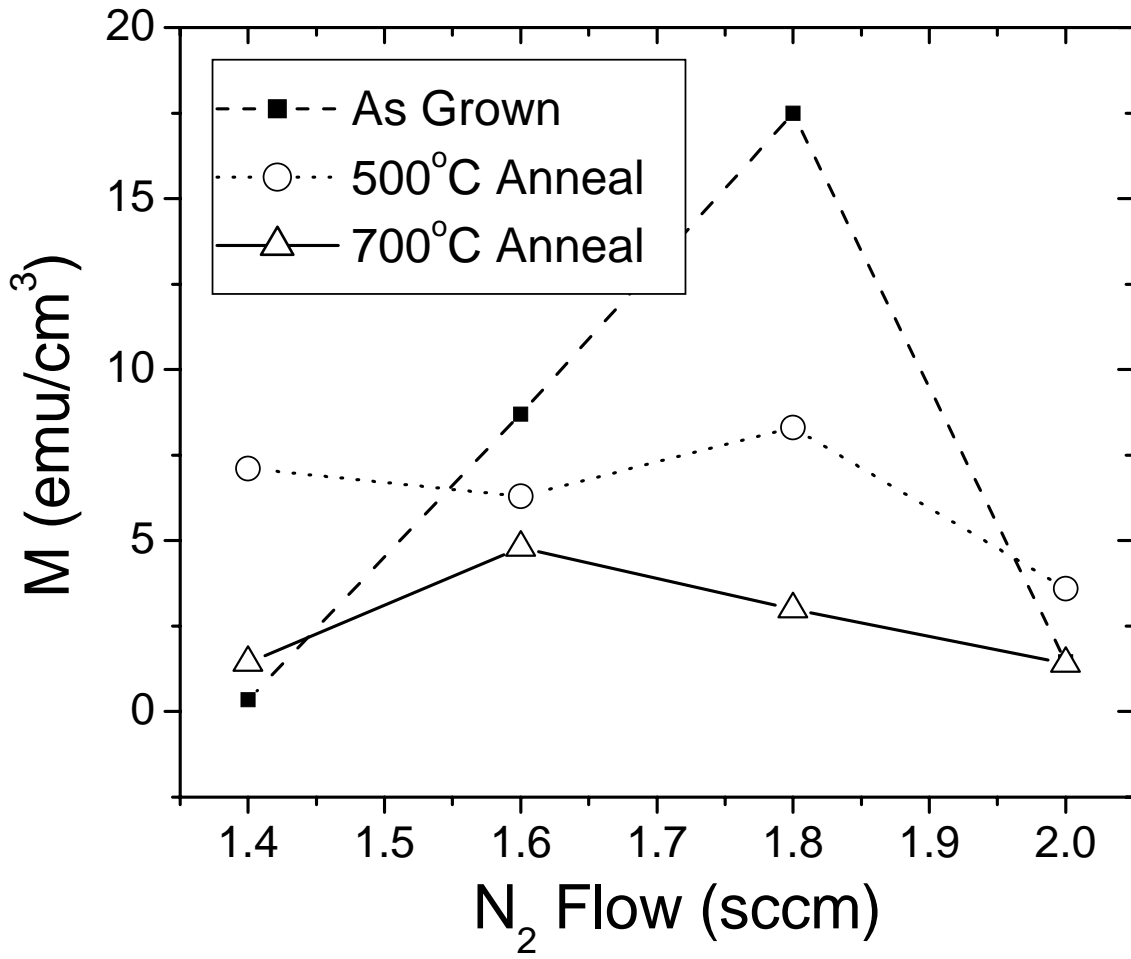


Figure 6-6. Nitrogen flow rate versus saturation magnetization shown for various plasma anneal temperatures.

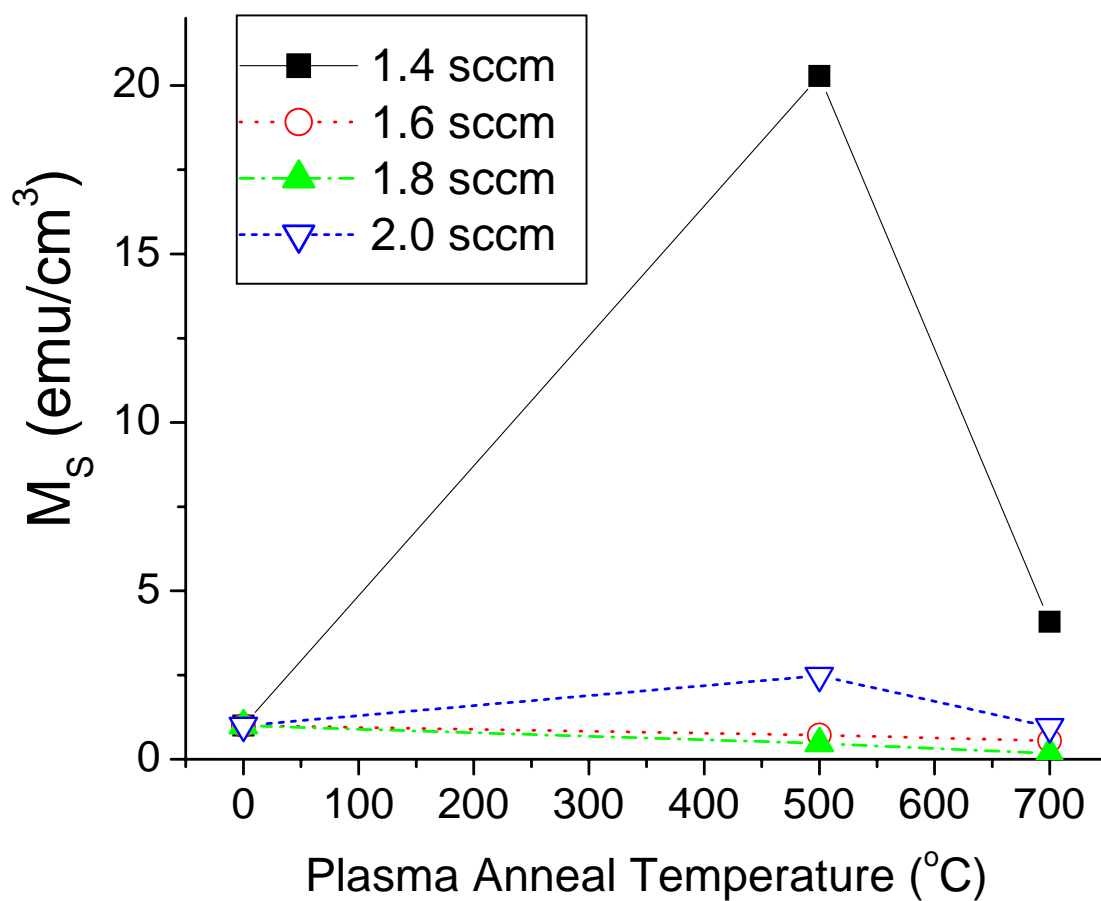


Figure 6-7. Normalized saturation magnetization versus nitrogen plasma anneal temperature for varying nitrogen flow rates during GaGdN growth. As grown values for normalization are from Figure 6-6.

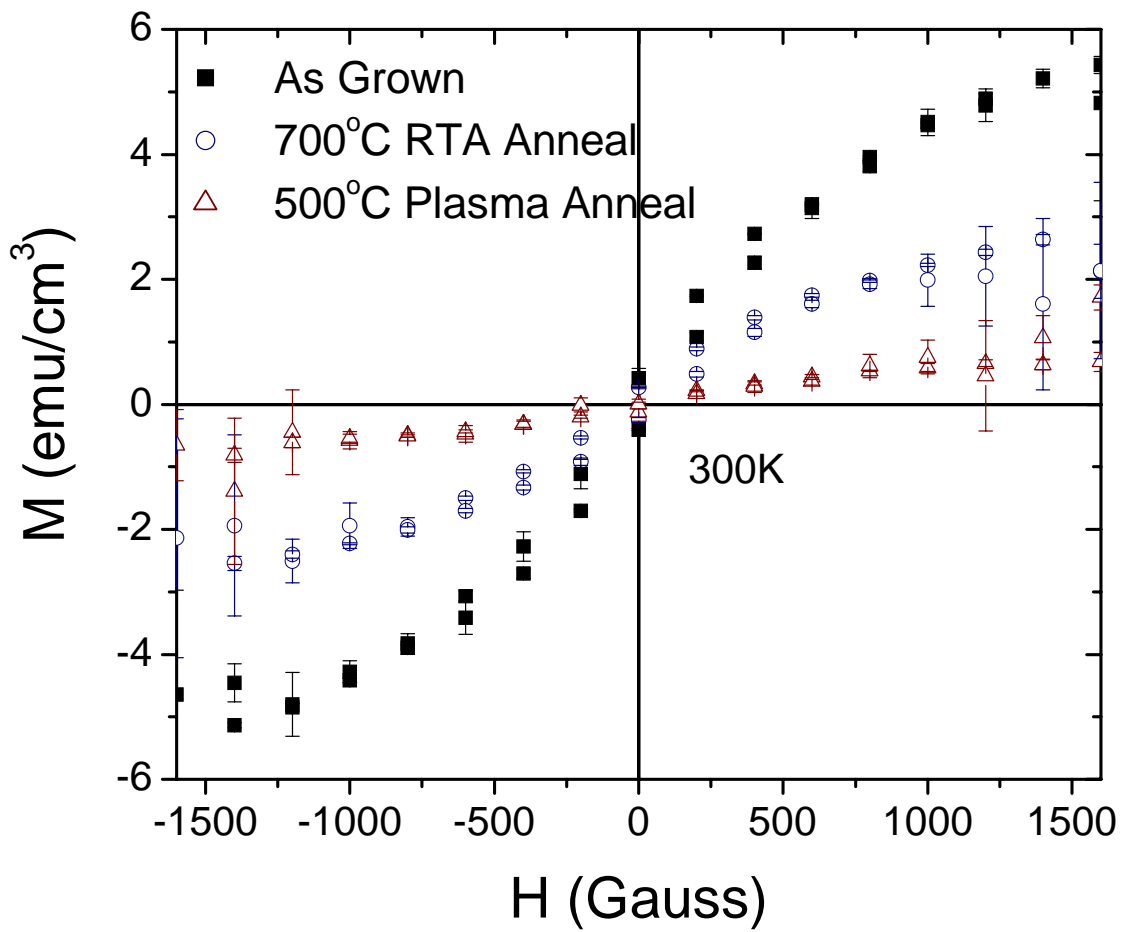


Figure 6-8. Hysteresis loops shown for GaGdN as grown, after a 700°C RTA, and further plasma annealing at 500°C. Curves were taken at 300K.

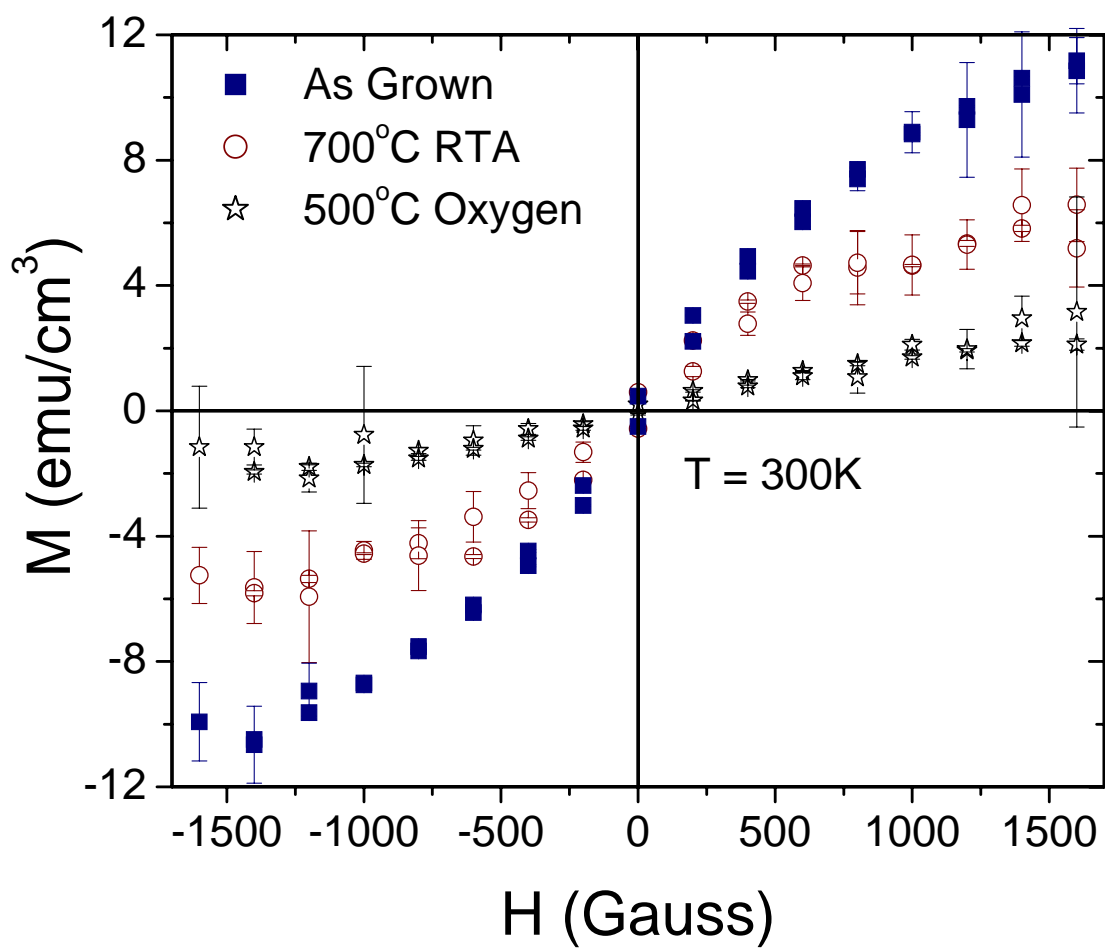


Figure 6-9. Magnetization versus applied field curves shown for GaGdN as grown, after RTA at 700°C, and further oxygen plasma annealing at 500°C.

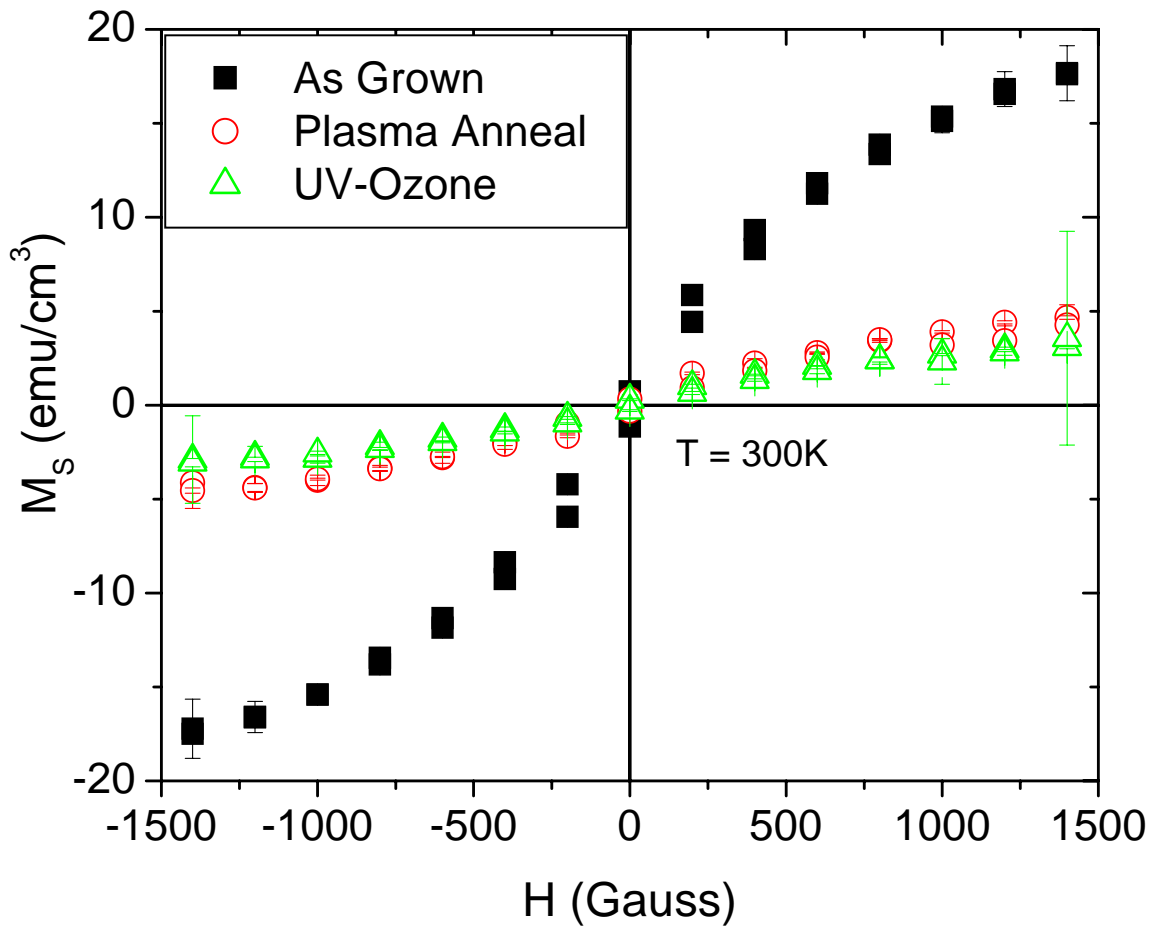


Figure 6-10. Hysteresis loops show magnetization for GaGdN as grown, after nitrogen plasma annealing at 700°C, and 60 min exposure to ultraviolet ozone.

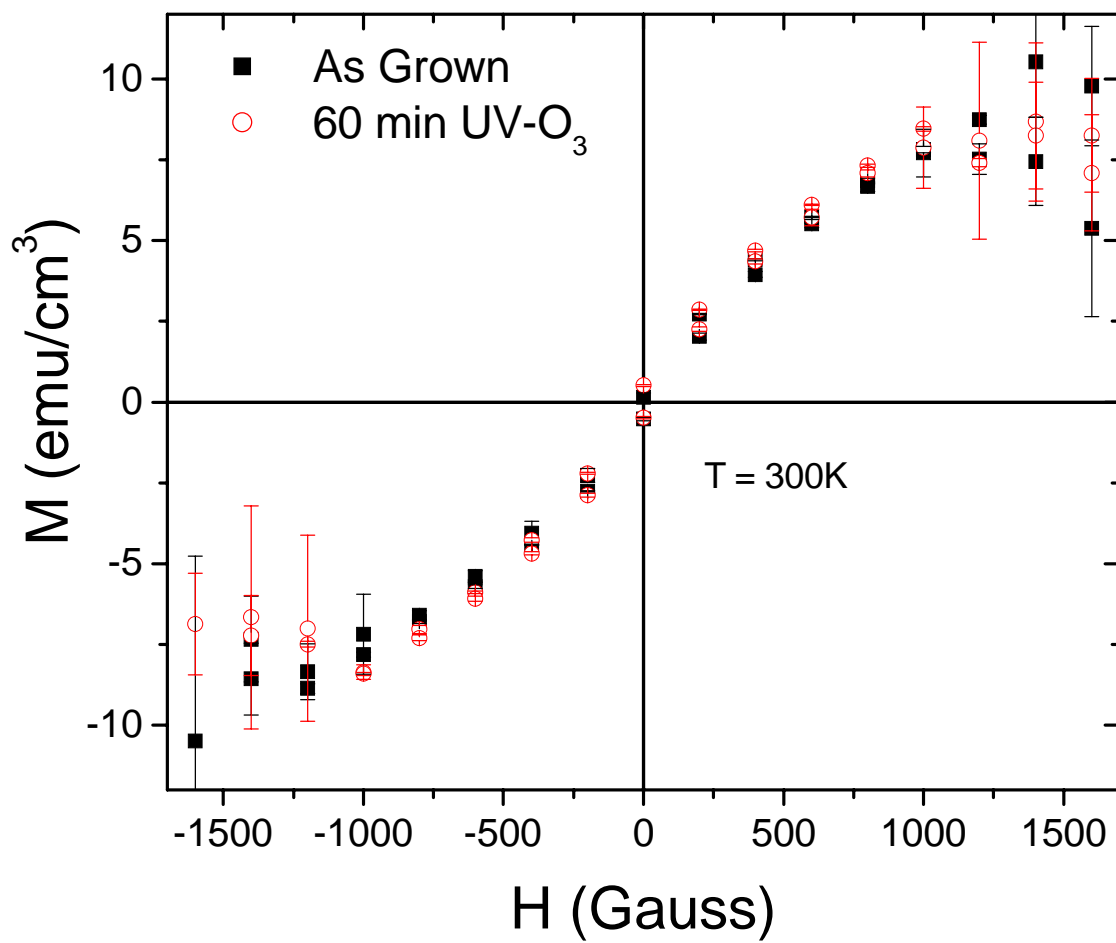


Figure 6-11. Hysteresis loops shown for GaGdN before and after 60 minutes of UV-O<sub>3</sub> exposure.

## CHAPTER 7 GROWTH AND CHARACTERIZATION OF GADOLINIUM-DOPED ALUMINUM GALLIUM NITRIDE

The same properties that make GaN materials such good device material –high thermal stability, wide band gap, and electronic stability also hold true for AlGaIn films. A combination of these two materials in AlGaIn/GaN heterostructures comprises a key component in several devices such as high electron mobility transistors,<sup>73-75</sup> violet and UV laser diodes,<sup>76</sup> and light-emitting diodes.<sup>77</sup> In addition, these heterostructures have an added advantage of being IR insensitive, which allows their use in UV photodetectors without the necessity of additional filters.<sup>78</sup> Further by changing of the ratio between Group III species allows for the selection of cut-off wavelength. In alignment with DMS interests, AlGaIn, with transition metal (TM) dopants, has been suggested as a possible candidate in spintronic devices such as polarized light emitters or spin transistors.<sup>79</sup> Toward this end, formation of ferromagnetic AlGaIn has been studied by implantation of TM ions. However, ferromagnetic behavior was only observed for n-AlGaIn:Co and p-AlGaIn:Mn. Of these two films, n-AlGaIn:Co exhibited the largest saturation magnetization ( $\sim 0.4 \text{ emu/cm}^3$ ) with a coercive field  $\sim 85$  Oe at room temperature.<sup>80</sup> Although ion implantation of AlGaIn with rare earth materials, such as Gd, has not been performed, the previously observed ferromagnetism in epitaxially grown AlN:Gd and GaGdN:Gd suggests that AlGaIn:Gd might show similar magnetic behavior.

### **Experimental Procedure**

During the AlGaIn:Gd growth, the substrate thermocouple was kept at 630°C, while the Al cell temperature ( $T_{\text{Al}}$ ) was varied between 1000-1100°C, as measured by the cell thermocouple. Nitrogen was introduced to the plasma head at a flow rate of 1.6 sccm. The dopant cell ( $T_{\text{Gd}}$ ) and Ga cell temperatures ( $T_{\text{Ga}}$ ) were held constant at 1050°C and 785°C between for all runs.

Reflection high energy diffraction was observed *in situ* in order to monitor the film growth. These films, for the most part, demonstrated 2D/3D growth, as evidenced by the RHEED patterns. However, films grown at  $T_{\text{Al}} = 1025^\circ\text{C}$  showed the smoothest growth. The 1 x 3 reconstruction seen

in the films grown at lower cell temperatures starts to fade at  $T_{\text{Al}} = 1075^{\circ}\text{C}$ , and completely disappears at  $T_{\text{Al}} = 1100^{\circ}\text{C}$ . A representative image of films grown at the lower temperatures is shown in Figure 7-1. As expected, increasing the aluminum content also caused an increase in the AlGa<sub>N</sub>:Gd growth rate, starting at 875 Å/hr for  $T_{\text{Al}} = 1000^{\circ}\text{C}$ , and increasing to 1600 Å/hr for  $T_{\text{Al}} = 1100^{\circ}\text{C}$ . A plot of these changes is shown in Figure 7-2.

### Results and Discussion

Atomic force microscopy was employed to determine the surface morphology of the films. The root mean square roughness of these films was found to be roughly 12 Å at the 1  $\mu\text{m}^2$  scan size (Figure 7-3) and 18 Å using a 5  $\mu\text{m}^2$  scan. Growth at  $T_{\text{Al}} = 1000^{\circ}\text{C}$  resulted in a slightly rougher surface, 18 Å and 24 Å, respectively, for 1  $\mu\text{m}^2$  and 5  $\mu\text{m}^2$  scans. With this one exception, these values show that the AlGa<sub>N</sub>:Gd films were slightly smoother than GaGdN. One previous study comparing the roughness of AlGa<sub>N</sub> based on Al composition reported that film morphology was independent of Al incorporation,<sup>81</sup> which agrees with these results.

The composition of these films was examined with Auger electron spectroscopy (AES). Focusing on the ratio of the Group III species, it can be seen from Figure 7-4 that there is a linear relation between  $T_{\text{Al}}$  and Al incorporation. The composition of Gd did not show up on the scan, and the oxygen levels were on par with that seen in undoped AlN films. A representative AES spectrum is shown in Figure 7-5.

Hall measurements were taken to determine the electric properties of the samples. The AlGa<sub>N</sub>:Gd films were n-type with higher conductivity than was measured in GaGdN samples. The general trend for this material was one of decreasing carrier concentration and conductivity with increasing Al content, with a major exception for the 20% Al sample. The effect on carrier concentration with Al composition is shown in Figure 7-6. At the lowest Al concentration (14%), the carrier concentration was  $1.2 \times 10^{18} \text{ cm}^{-3}$ , which gradually decreased to  $5.0 \times 10^{17} \text{ cm}^{-3}$  when the Al

content increased to 64%. It should also be noted that the 26% Al sample showed the highest carrier concentration, at  $1.45 \times 10^{18} \text{ cm}^{-3}$ .

Using SQUID magnetometry, the magnetic properties of the films were examined. Hysteresis was observed in all of the films at room temperature. The general shape of these hysteresis loops is shown in Figure 7-7. Not pictured is trace taken at 10 K, as they overlaid each other, indicating the Curie temperature ( $T_C$ ) is above room temperature. The graph of magnetization versus percentage of aluminum (Figure 7-8) shows a vaguely linear relation with an outlier at  $T_{Al} = 1125^\circ\text{C}$  (or 26% Al). From  $T_{Al}$  of 1050 through  $1100^\circ\text{C}$ , the magnetic signal increases with Al incorporation. An opposing trend exists for the coercive field, with the sample grown at  $T_{Al} = 1125^\circ\text{C}$  showing up as an outlier once again. This is demonstrated in Figure 7-9, with coercivities ranging from 60 to 35 Oe. Comparing this material with previous Gd-doped material, optimal AlN:Gd films ( $T_{Al} = 1075^\circ\text{C}$ ) have shown a saturation magnetization of  $11 \text{ emu/cm}^3$  and coercivity of  $\sim 34 \text{ Oe}$ ,<sup>57</sup> while GaN:Gd samples grown under the same substrate and nitrogen conditions hover around  $8 \text{ emu/cm}^3$  saturation and  $\sim 42 \text{ Oe}$  coercivity.

Magnetization versus temperature measurements were also taken. The zero field cooled and field cooled traces for AlGaN:Gd grown at  $T_{Al} = 1025^\circ\text{C}$  are shown in Figure 7-10. As distance between the two traces is still open at 300 K, it can be concluded that  $T_C$  for this material lies above room temperature.

Since processing of GaN-based devices often requires temperatures above  $700^\circ\text{C}$  to anneal ohmic contacts, the same thermal stability is required for AlGaN films that would be included in a GaN-based spintronic device. A quick investigation of the thermal stability of AlGaN:Gd in regards to its magnetic properties was carried out. By annealing a sample under nitrogen plasma, the question of dependence on nitrogen loss from rapid thermal annealing was eliminated. A sample grown with  $T_{Al} = 1025^\circ\text{C}$  (26% Al) was nitrogen plasma annealed at  $700^\circ\text{C}$  for 30 minutes. The result was a

degradation of over 50%, as seen in Figure 7-11. This is larger than that seen for GaGdN and GaGdN:Si, but with the large starting magnetization, this may not rule out use of this material.

### **Summary and Conclusion**

In conclusion, AlGa<sub>x</sub>N:Gd films were grown with varying Al concentrations with larger magnetic signal than observed for TM ion implanted AlGa<sub>x</sub>N. All except for one sample had lower saturation magnetizations than GaGdN or AlGdN, however, the outlier showed evidence of the best crystal growth as evidenced by a 2D RHEED pattern. It should also be noted that the AlGdN samples all exhibited 3D growth patterns. It has already been determined that crystal quality has a large effect on magnetization. Examining the band structures for GaN and AlN may hold the key to understanding the reason larger bandgap material is achieving higher magnetization even on samples with lower crystal quality. Since the band offset between GaN and AlN mainly resides in changes in the conduction band, the trap level that has been indicated as having a large effect on magnetization should sit at near levels in the material. With more distance between this trap level and the conduction band, it should be easier to fill in the larger band gap material (AlN). Correspondingly, we do see a gentle rise in magnetization with increasing Al composition, which fits well with this explanation. For the majority of the samples, coercivity decreased with larger Al concentration down to levels seen for GaGdN. The material is not extremely thermally stable, and shows slightly larger loss of magnetization than GaGdN.

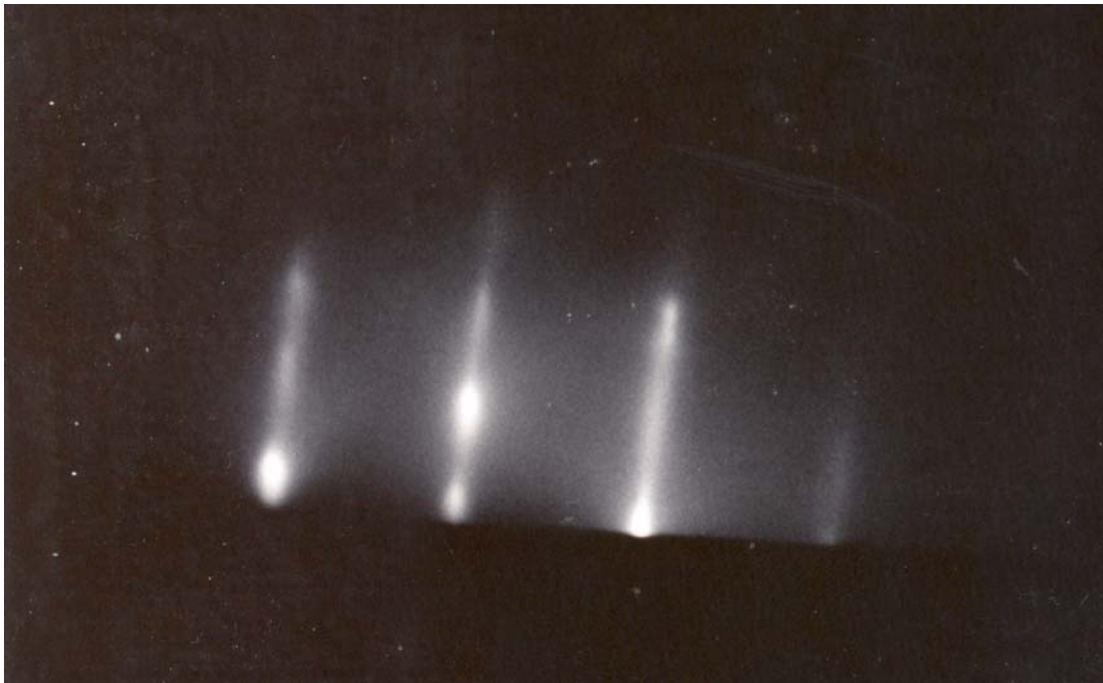


Figure 7-1. Images of RHEED pattern for  $T_{Al} = 1000^{\circ}C$ . Top shows the faint 1 x 3 pattern. Bottom shows the start of 2D/3D growth.

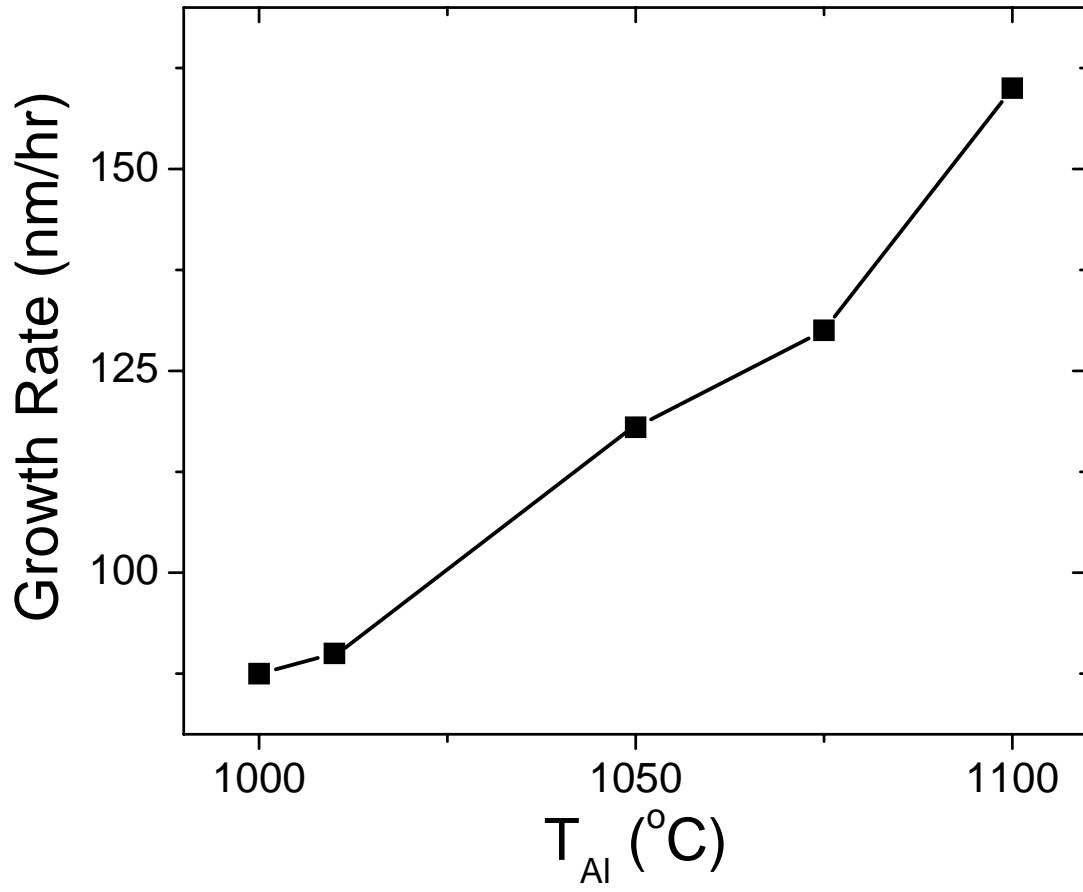


Figure 7-2. Growth rate of AlGaIn:Gd as a function of  $T_{Al}$  is shown.

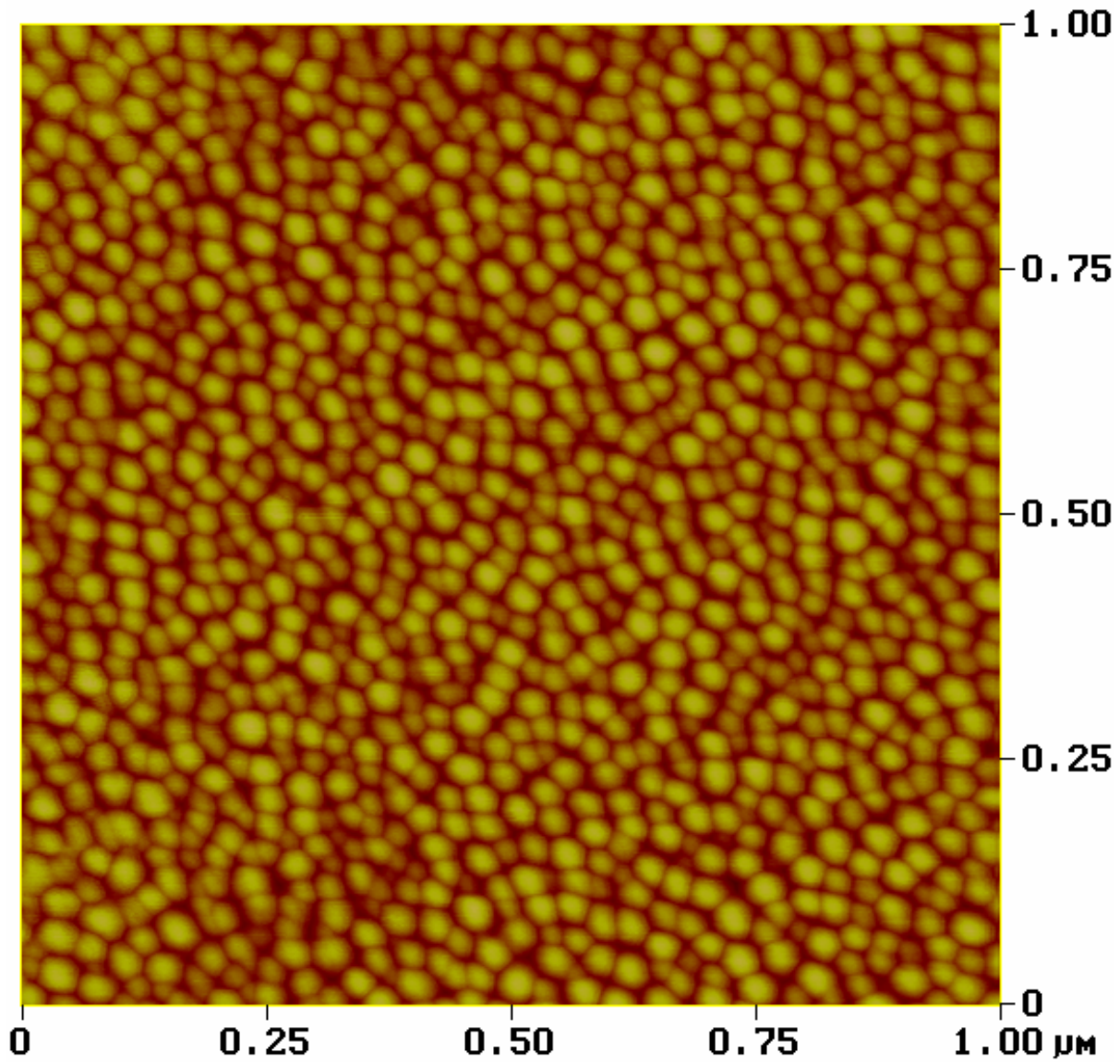


Figure 7-3. AFM image shows the surface of AlGaIn with  $T_{\text{Al}} = 1025^\circ\text{C}$  (26% Al). The rms roughness for this film was 1.2nm.

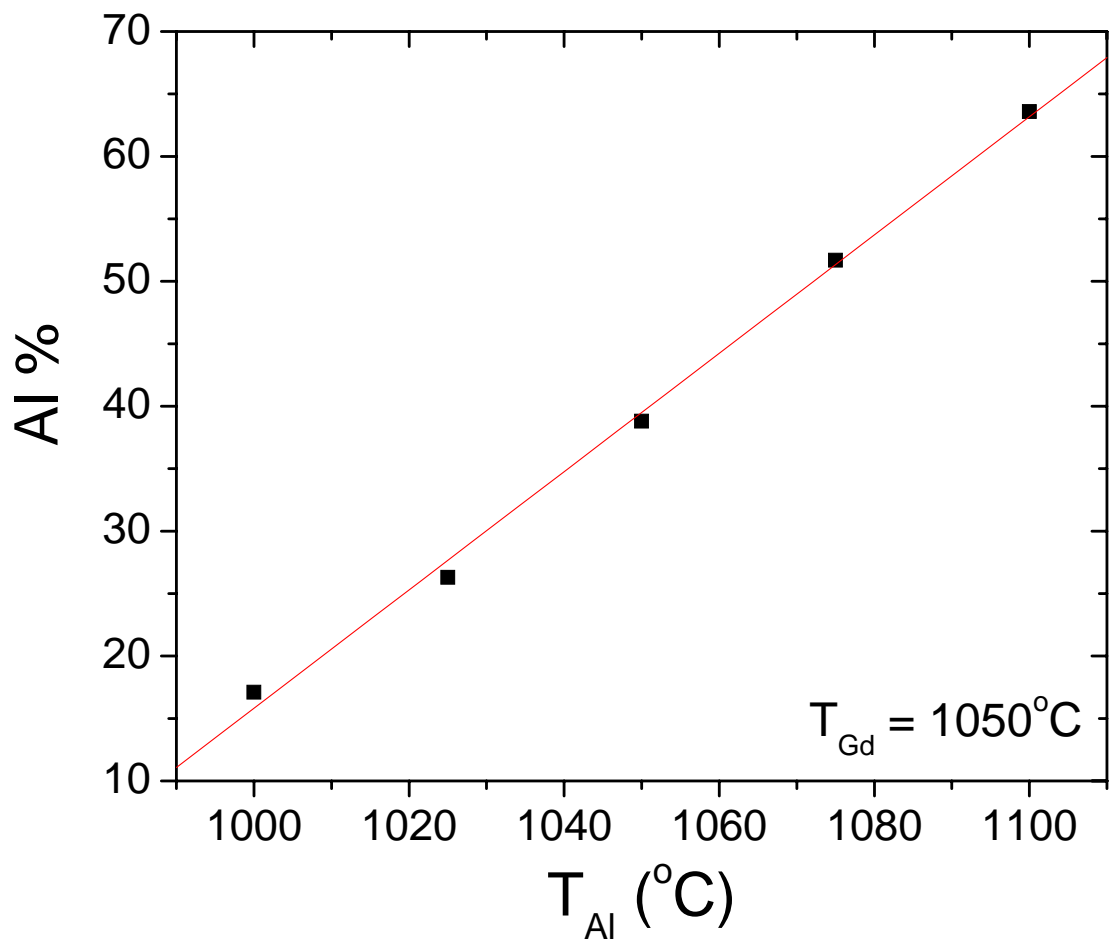


Figure 7-4. Composition of Al in  $Al_xGa_{1-x}N:Gd$  versus  $T_{Al}$  is shown along with the linear fit of the data.

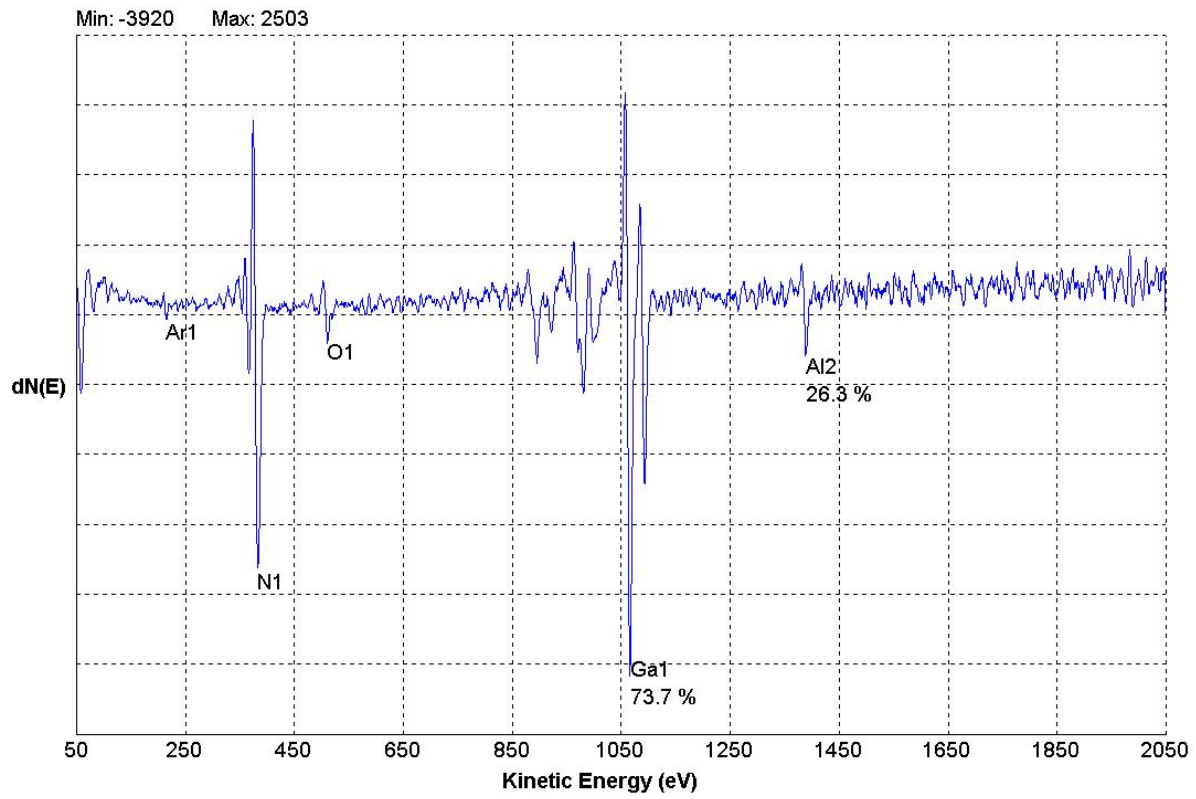


Figure 7-5. Indicative AES scan is shown for AlGaN:Gd at  $T_{Al} = 1025^{\circ}\text{C}$  after a 30 sec. sputter. Oxygen accounted for 2.3% of the total composition.

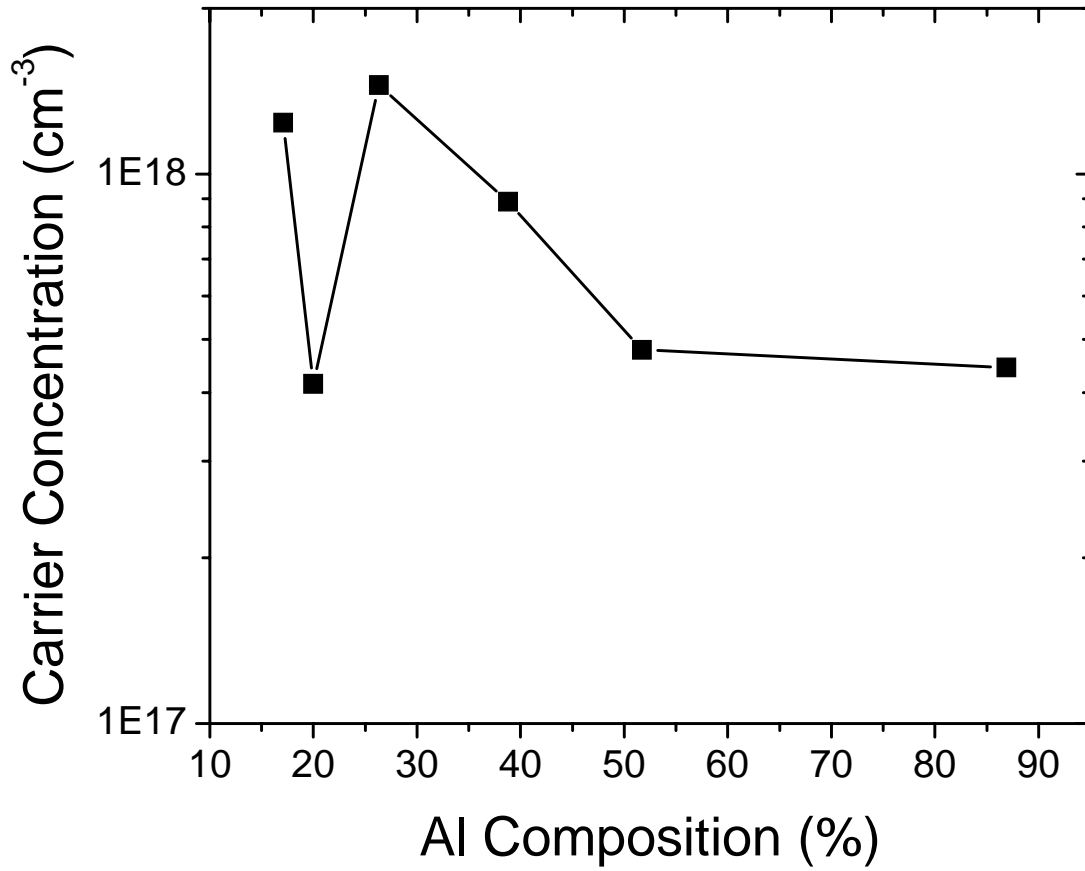


Figure 7-6. Carrier concentration as a function of Al composition is shown. The overall trend of decreasing carrier concentration, with the exception of an outlier at 20% Al ( $T_{Al} = 1010^{\circ}\text{C}$ ), can be observed.

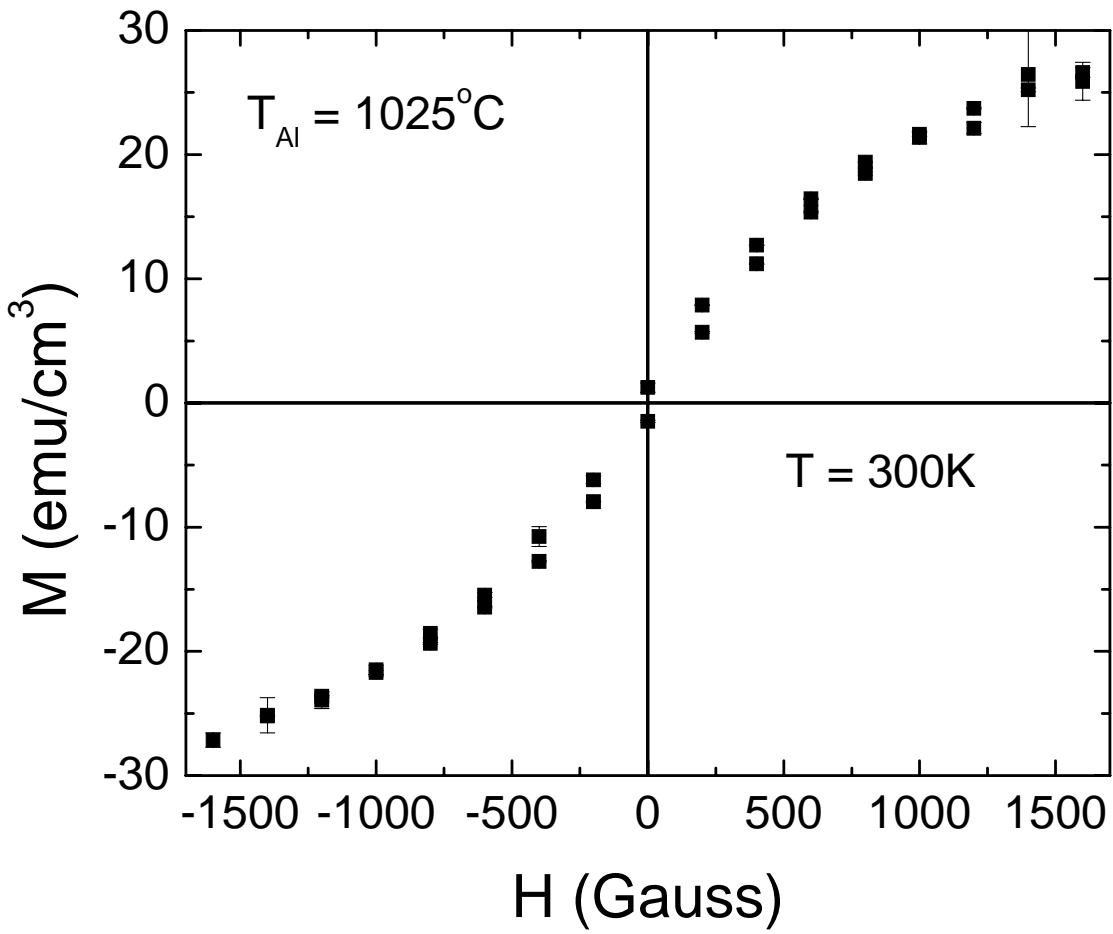


Figure 7-7. Magnetization versus applied field curve shown for  $T_{\text{Al}} = 1025^\circ\text{C}$  (26% Al). These measurements were taken at 300K.

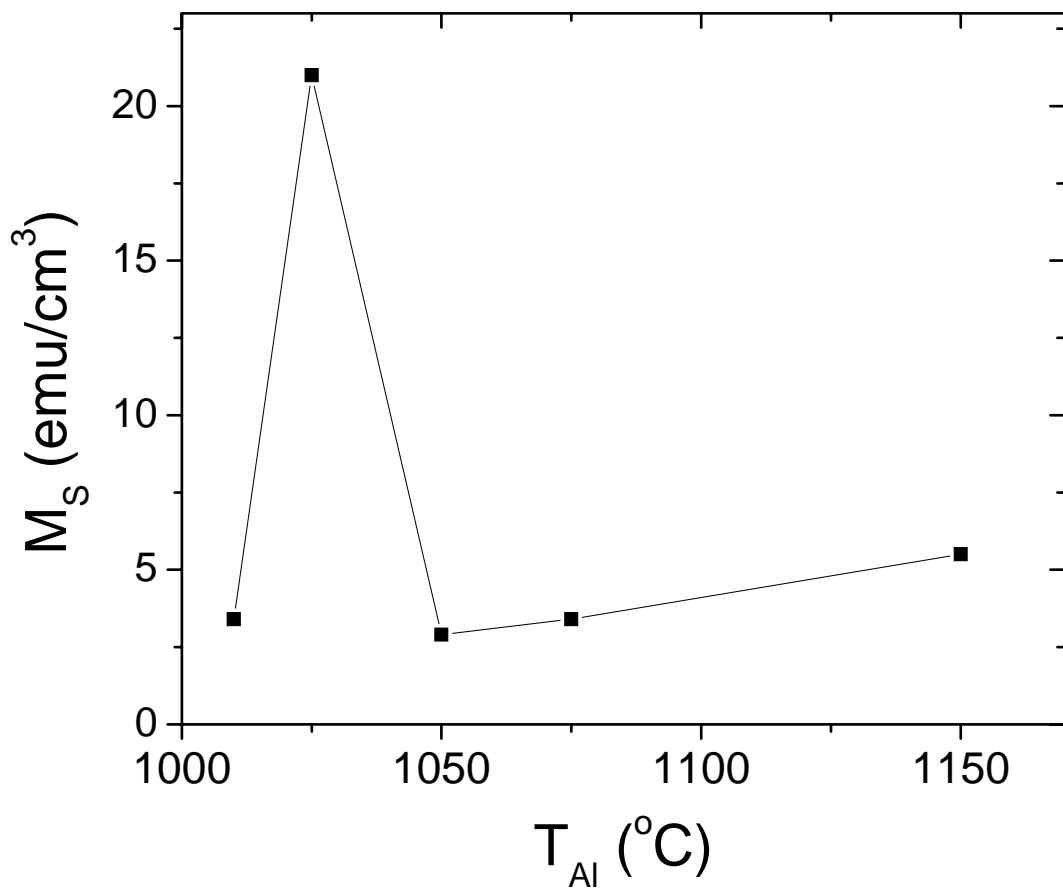


Figure 7-8. Saturation magnetization vs aluminum cell temperature is plotted. Magnetization measurements were taken at 300K and saturation magnetization was estimated at 1000G.

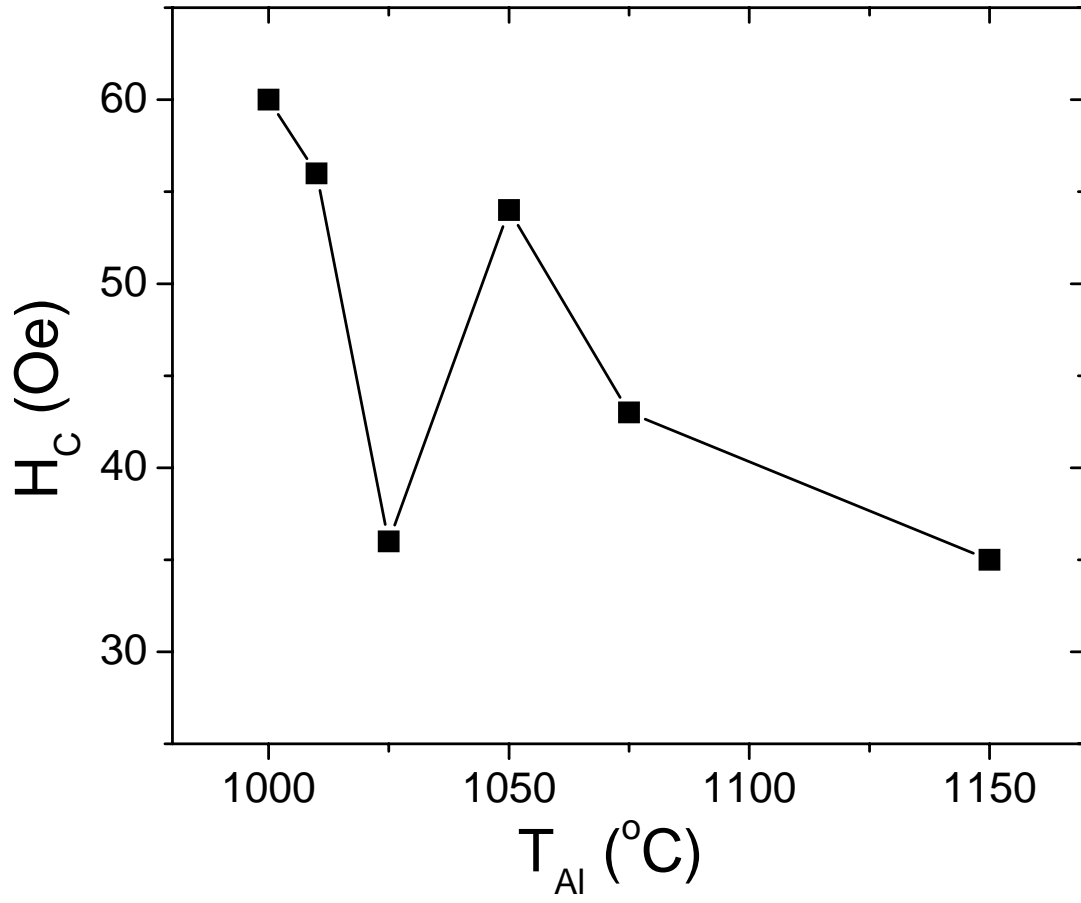


Figure 7-9. Coercive field shown plotted against  $T_{Al}$ . The magnetic properties were determined from hysteresis loops taken at 300K.

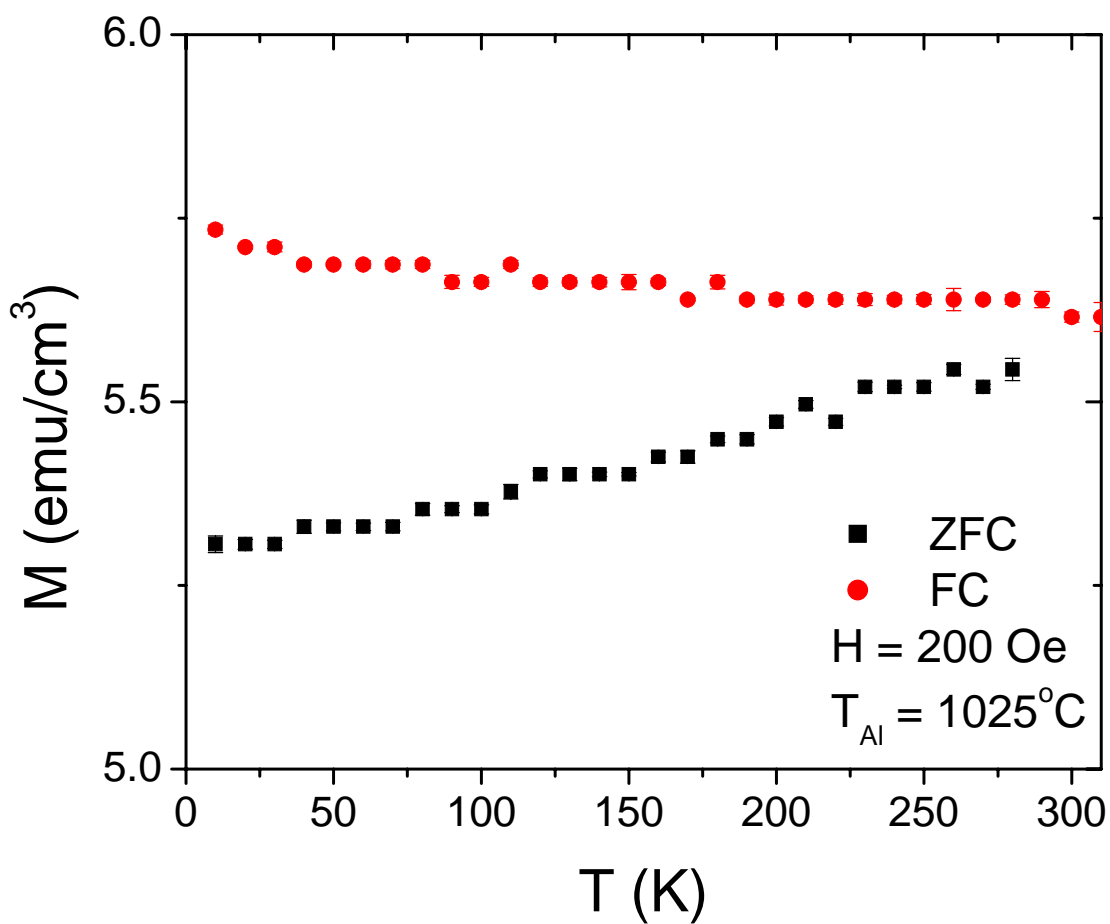


Figure 7-10. Magnetization versus temperature curve shows both zero field cooled and field cooled traces at an applied field of 200 Oe. The  $T_{Al}$  was  $1025^{\circ}\text{C}$  (26% Al).

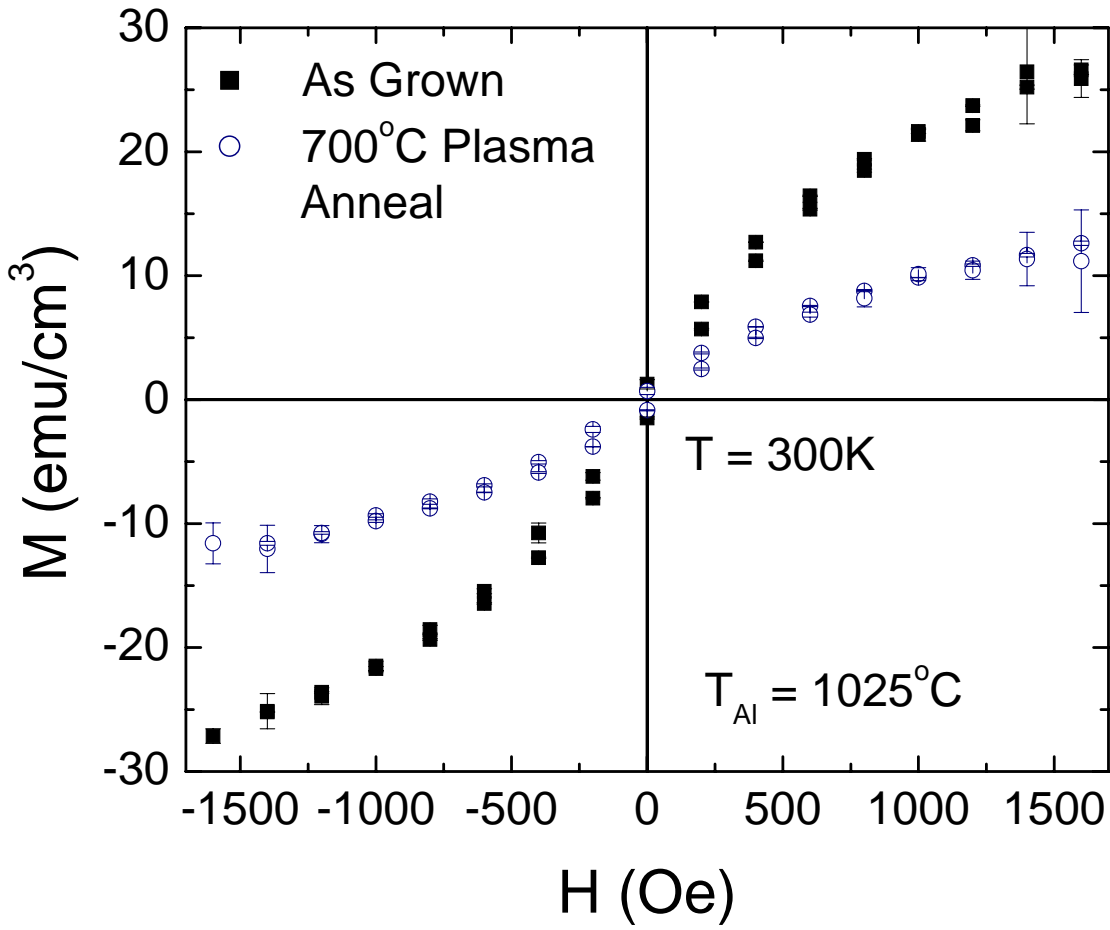


Figure 7-11. Hysteresis curves before and after plasma annealing at 700°C for AlGaIn:N:Gd with  $T_{\text{Al}} = 1025^\circ\text{C}$  (26% Al). Magnetic measurements were taken at 300K.

## CHAPTER 8 GADOLINIUM-BASED DILUTE MAGNETIC SEMICONDUCTOR HETEROSTRUCTURES

In the development of AlGa<sub>N</sub>/Ga<sub>N</sub> heterostructure devices, very thin layers sandwiched on top of each other in what are referred to as quantum wells are required. This is especially true for those devices based on the tunneling properties of electrons. The ability to reliably control the growth of such layers is one of the benefits of using molecular beam epitaxy (MBE).

The furthest extreme of quantum wells occurs when the film growth is constrained to form islands without allowing the islands to converge. Layering of this sort results in quantum dots, which have also been advanced as novel device structures. Reducing material down to quantum thicknesses (generally, those less than 100Å) may also affect the behavior of the films. This chapter will examine the feasibility of using Gd-doped dilute magnetic semiconductors (DMSs) as layers for quantum wells along with determining the limits within which the material retains its ferromagnetic behavior.

### **Experimental Procedure**

Several materials were examined in this study. They include GaGdN, GaGdN:Si, and AlGa<sub>N</sub>:Gd. The purely Ga<sub>N</sub>-based films were grown in a superlattice structure, layering the active DMS material between layers of AlN. To investigate the thickness effects on AlGa<sub>N</sub>:Gd, the DMS films were sandwiched between layers of undoped Ga<sub>N</sub>. The thickness of the buffering layer (u-Ga<sub>N</sub> or AlN) was chosen to prevent the material from acting like a digital alloy and to prevent leakage of the magnetic element. The cell temperatures for the DMS materials were measured at  $T_{\text{Ga}} = 785^{\circ}\text{C}$ ,  $T_{\text{Gd}} = 1050^{\circ}\text{C}$ ,  $T_{\text{Si}} = 1100^{\circ}\text{C}$ , and  $T_{\text{Al}} = 1025^{\circ}\text{C}$ , while nitrogen was introduced at a flow rate of 1.6 sccm. The Ga<sub>N</sub> buffer layers used in the AlGa<sub>N</sub>:Gd superlattice were also grown at the conditions of  $785^{\circ}\text{C}$   $T_{\text{Ga}}$  and 1.6 sccm nitrogen. The AlN buffer layers were grown with  $T_{\text{Al}} = 1150^{\circ}\text{C}$  and a nitrogen flow of 1.4 sccm. In order to allow the chamber pressure to stabilize after changing the nitrogen flow rate, a settling time of up to 3 minutes was inserted between layers.

The samples were studied during growth with RHEED. After growth the stack thickness was measured. SQUID magnetometry was used to establish whether the samples possessed hysteresis. Those samples retaining ferromagnetic behavior were also examined with XRR. By doing so, the exact thickness of the layers could be determined.

### **GaGdN/AlN Heterostructures**

The proposed structure for the GaGdN/AlN heterostructure study is shown in Figure 8-1. For these structures, the desired thickness for the AlN buffer layers was 100Å. The first attempt was extremely aggressive, with 33 GaGdN layers of 25Å for an overall active thickness of 825Å. Using in situ RHEED during growth, a pattern indicative of 2D growth was observed through the fifteenth repetition of GaGdN, but this became a 2D/3D pattern after the twentieth layer, and remained this way through the rest of the sample. Magnetic measurements of this sample showed no real ferromagnetic behavior (Figure 8-2). With such a small layer thicknesses, this is not extremely surprising. The gallium cell flux at these temperatures is about  $2.1 \times 10^{-7}$  Torr, while the flux from the gadolinium cell normally does not even register making it somewhere lower than  $3 \times 10^{-10}$  Torr. Comparing these fluxes makes it easier to see that the probability of a Gd atom impinging on the sample surface is extremely low. In addition, calculating the spacing between Gd atoms in GaGdN gives us a distance of 215Å at a Gd concentration of  $10^{17} \text{ cm}^{-3}$ , and at a Gd concentration of  $10^{16} \text{ cm}^{-3}$  this grows to 464Å.

Increasing the GaGdN layer to 90Å and using a periodicity of 10 layers had much better results. The RHEED pattern turned 2D/3D after 5 layers, which, relative to total DMS thickness, is an equivalent point to the previous structure. The XRR spectrum for this sample is shown in Figure 8-3. The AlN buffer layers were roughly 52Å thick, while the GaGdN layers were about 90Å. In addition, the AlN layers were much smoother than the intervening GaGdN ones, at 4Å versus 22Å. Although the curve is very sharp or clean (Figure 8-4), it does indicate some hysteresis with a

saturation magnetization of  $\sim 8.4 \text{ emu/cm}^3$ . Due to the thin layers of AlN, the behavior of this structure is similar to AlGa<sub>N</sub>:Gd films grown at  $T_{\text{Al}} = 1150^\circ\text{C}$  as in Chapter 7.

### **GaGdN:Si/AlN Heterostructures**

Since manipulating the Fermi levels to tune devices is helpful, and GaGdN:Si has also been shown to be ferromagnetic, the behavior of this film at quantum dimensions should also be investigated. This was first accomplished by using a periodicity of 10 layers of  $90\text{\AA}$  GaGdN:Si grown with  $T_{\text{Si}} = 1200^\circ\text{C}$  (all other conditions as previously reported) interspersed with  $80\text{\AA}$  AlN. The resulting stack exhibited ferromagnetic behavior, albeit at lower saturation magnetization ( $\sim 1.3 \text{ emu/cm}^3$ ) than in the bulk films (Figure 8-5). This can be explained by a lack of film optimization after adding a new substrate heater to the chamber. Re-optimizing found a peak in magnetization of GaGdN using the conditions  $T_{\text{Gd}} = 1050^\circ\text{C}$ ,  $T_{\text{Si}} = 1100^\circ\text{C}$ , with all other previous conditions unchanged. Using these conditions and 5 repetitions of GaGdN:Si layers of  $180\text{\AA}$  for a total active film stack thickness of  $900\text{\AA}$ , this growth also exhibited 2D/3D RHEED patterns about halfway through the growth. The magnetization versus applied field curve was much stronger in this case, and close to the bulk film signal (Figure 8-6). In addition, magnetization versus temperature measurements were performed (Figure 8-7). The zero-field cooled and field cooled traces show distinct differences from that of bulk growth GaGdN:Si, and appear to be closing at 300 K, showing the Curie temperature has been affected by the shrinkage of layer thickness.

### **AlGa<sub>N</sub>:Gd/GaN Heterostructures**

The other Gd-based DMS material that has shown promise is AlGa<sub>N</sub>:Gd. This material was also incorporated into a heterostructure with a periodicity of 10. Using XRR, the GaN buffer layers were measured to be roughly  $87\text{\AA}$  thick, while the AlGa<sub>N</sub>:Gd layers measured at  $185\text{\AA}$  (Figure 8-8). In contrast to the GaGdN/AlN MQW, the layers in this structure were all rather smooth and about the same roughness at  $\sim 19\text{\AA}$ . The RHEED patterns started to change to 2D/3D halfway through the growth, and remained so until the end of the growth. Measuring magnetization as a function of

applied field revealed that this material also exhibited ferromagnetic behavior (Figure 8-9). For these growth conditions, the overall magnetic saturation was about half of that of the bulk material.

### **Summary and Conclusion**

In summary, all of the Gd-based DMS films studied herein retained hysteresis when incorporated into thin layer heterostructures. Although hysteresis was observed with 33 repetitions of 25 Å GaGdN layers, 10 repetitions of 100Å this material does retain ferromagnetic behavior. GaGdN:Si required re-optimization to match the magnetic strength seen in bulk material. AlGaIn:Gd also retained hysteresis at these thinner film thicknesses.

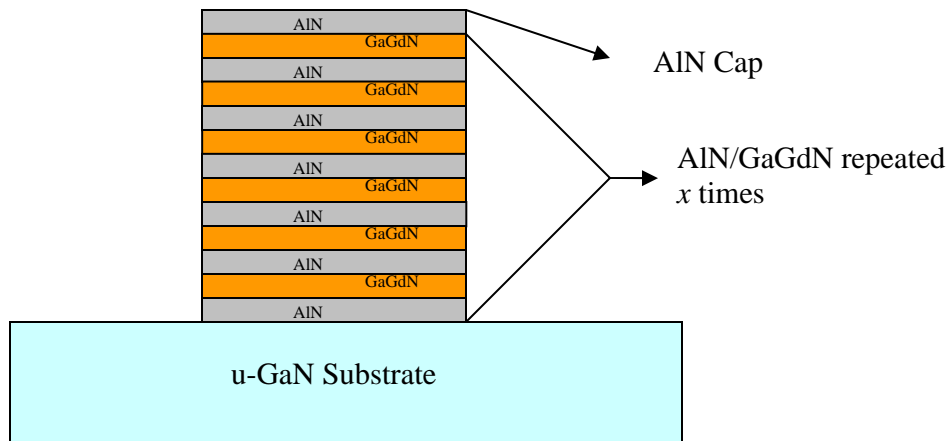


Figure 8-1. Schematic showing structure for GaGdN/Al MQW.

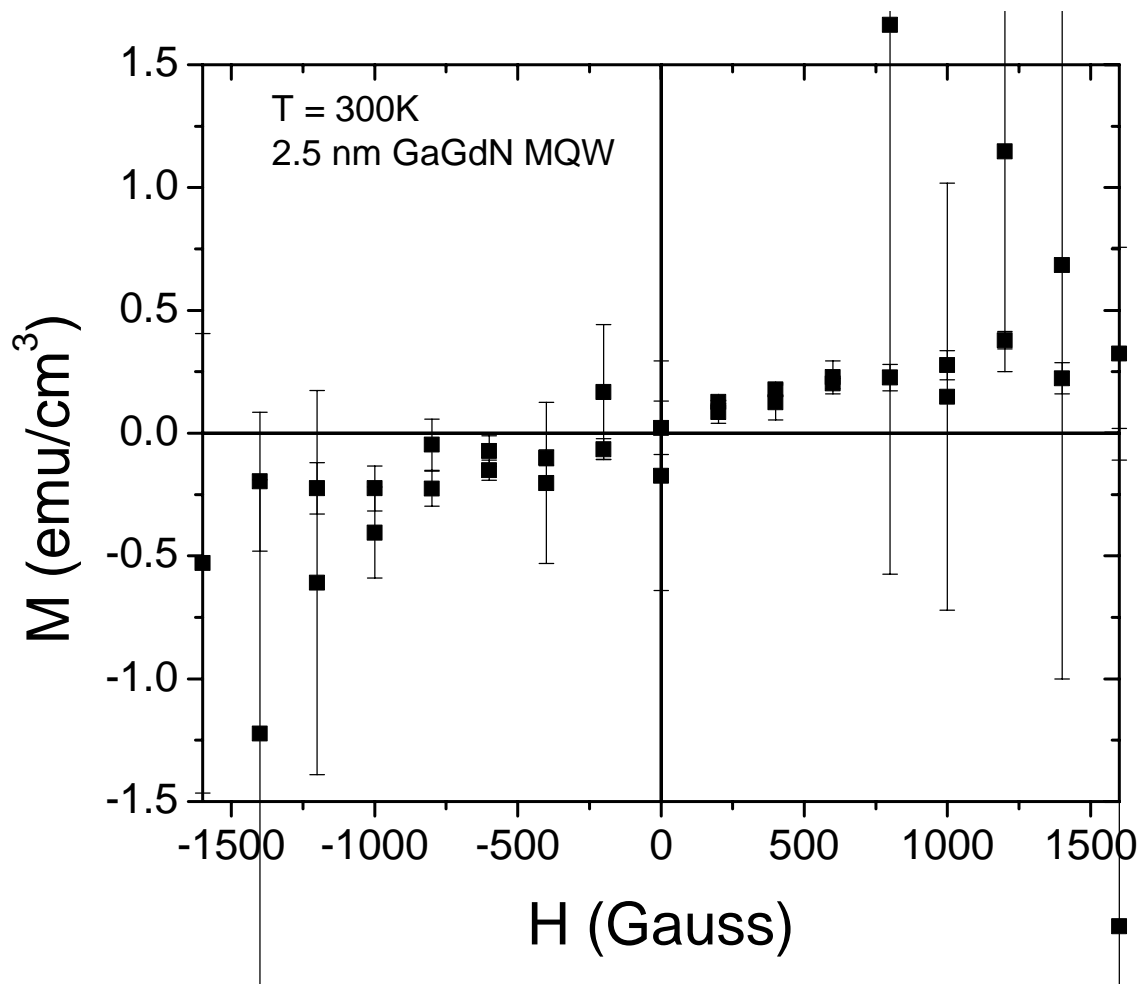


Figure 8-2. Hysteresis curve is shown for a 33x 25Å/100 Å GaGdN/AlN MQW.

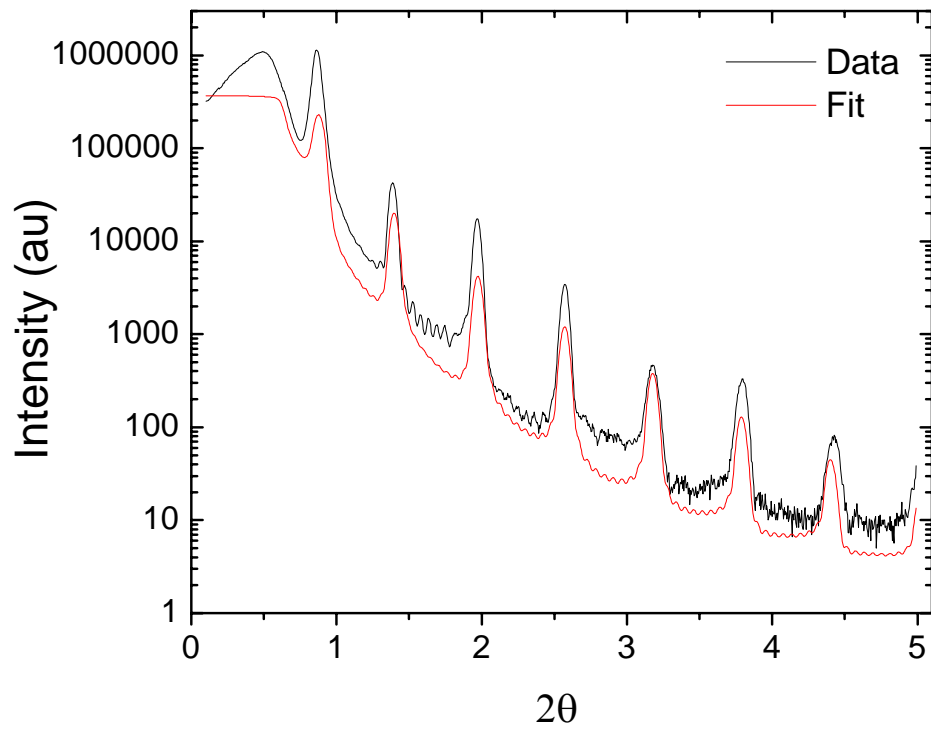


Figure 8-3. XRR spectrum is shown for the 10 periodicity GaGdN/AlN sample with layer thicknesses of 9/5.4nm. The data is shown in black, while the fit curve is in red.

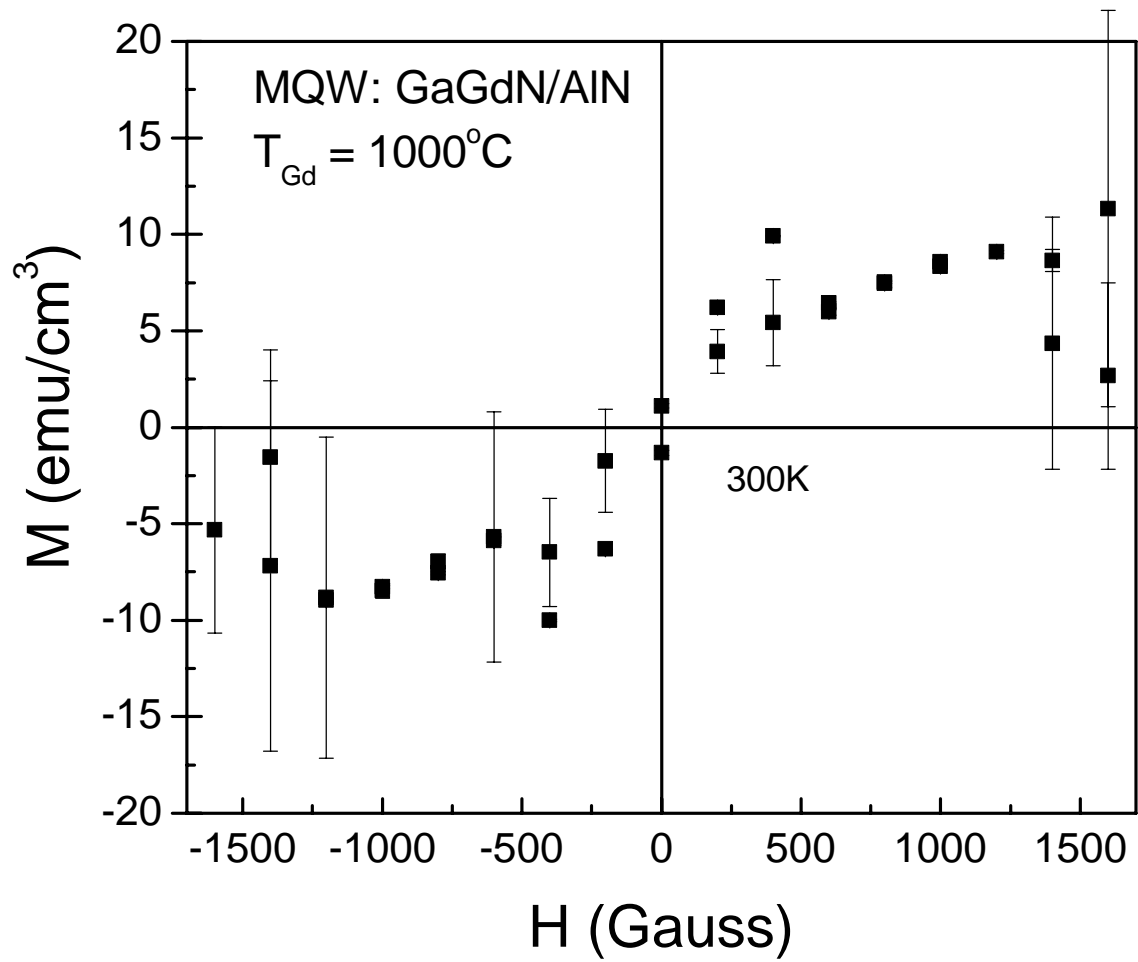


Figure 8-4. Magnetization versus applied field is shown for a 10 periodicity 90Å/52Å GaGdN/AlN structure.

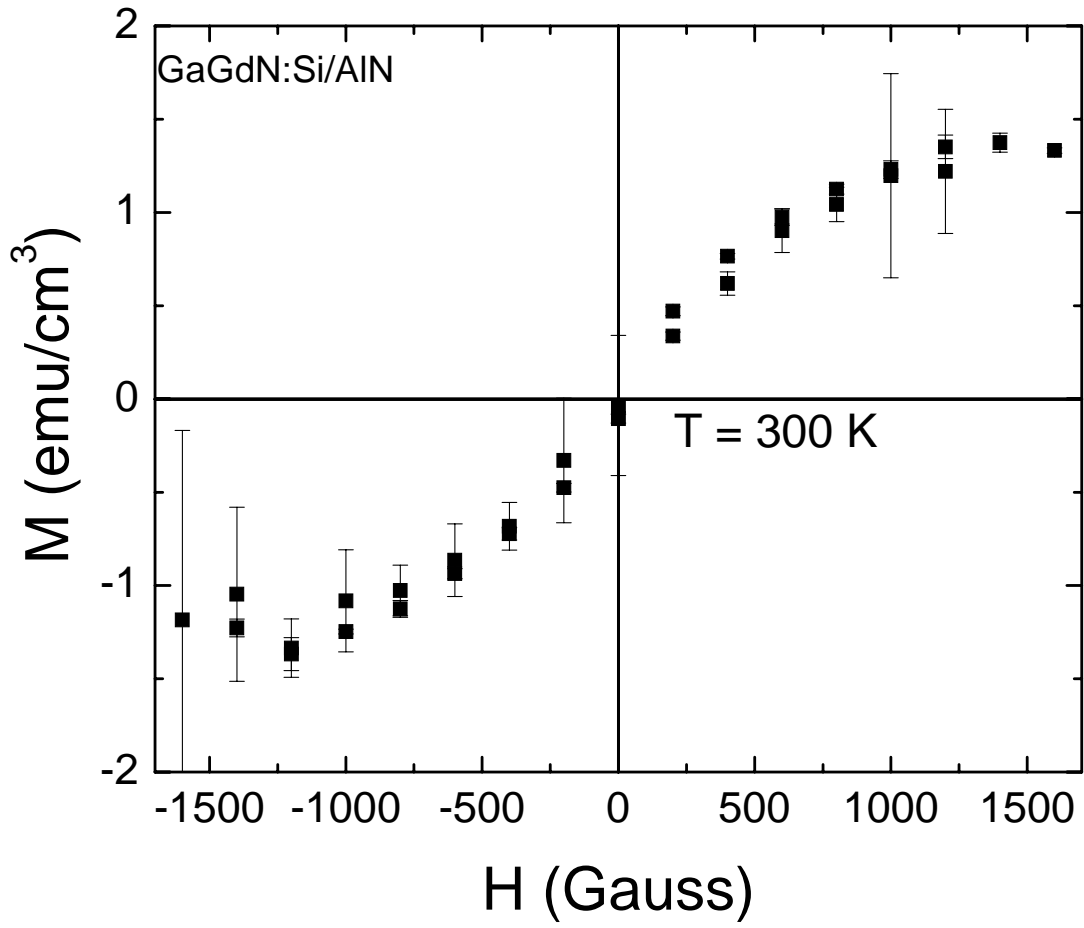


Figure 8-5. Magnetization versus applied field is shown for 10 repetitions of 90Å/80Å GaGdN:Si/AlN layers. The measured  $T_{\text{Si}}$  was 1200°C.

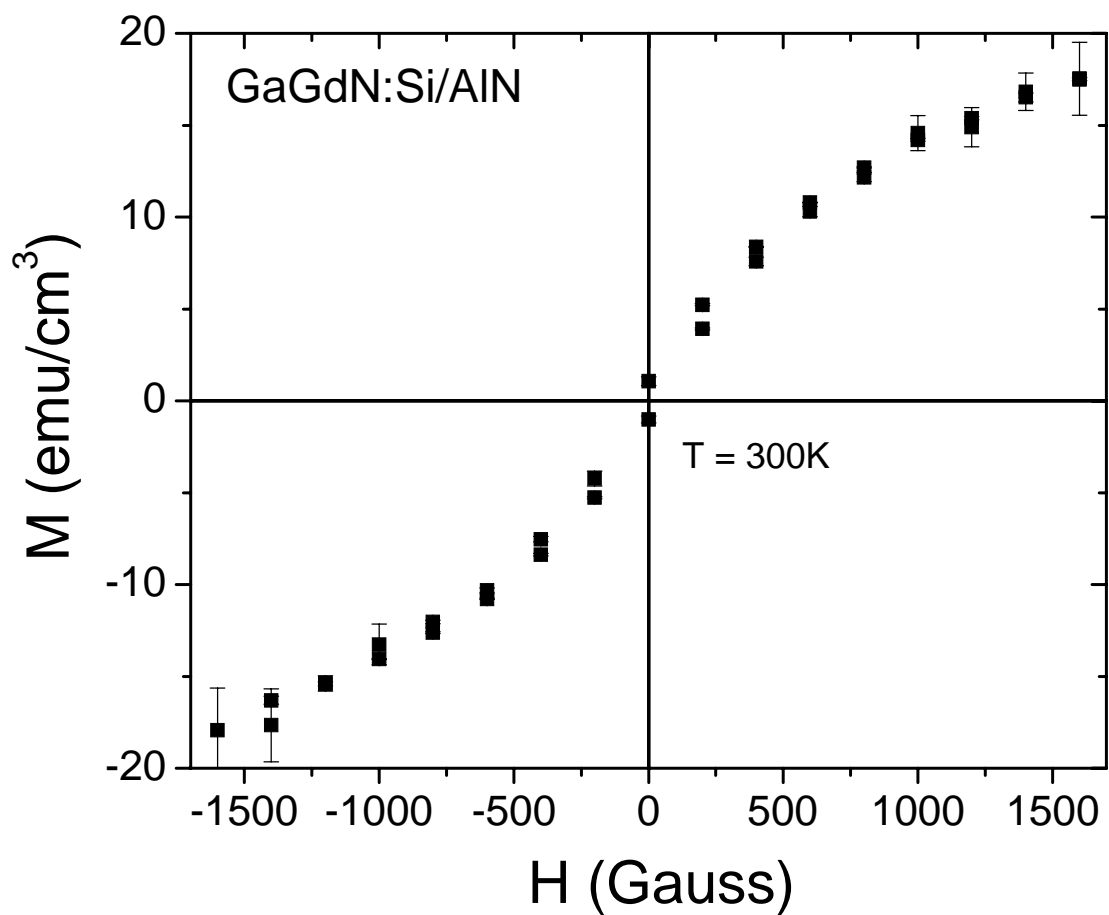


Figure 8-6. Magnetization versus applied field loop shown for 5x 180Å/80Å GaGdN:Si/AlN layers taken at 300K.

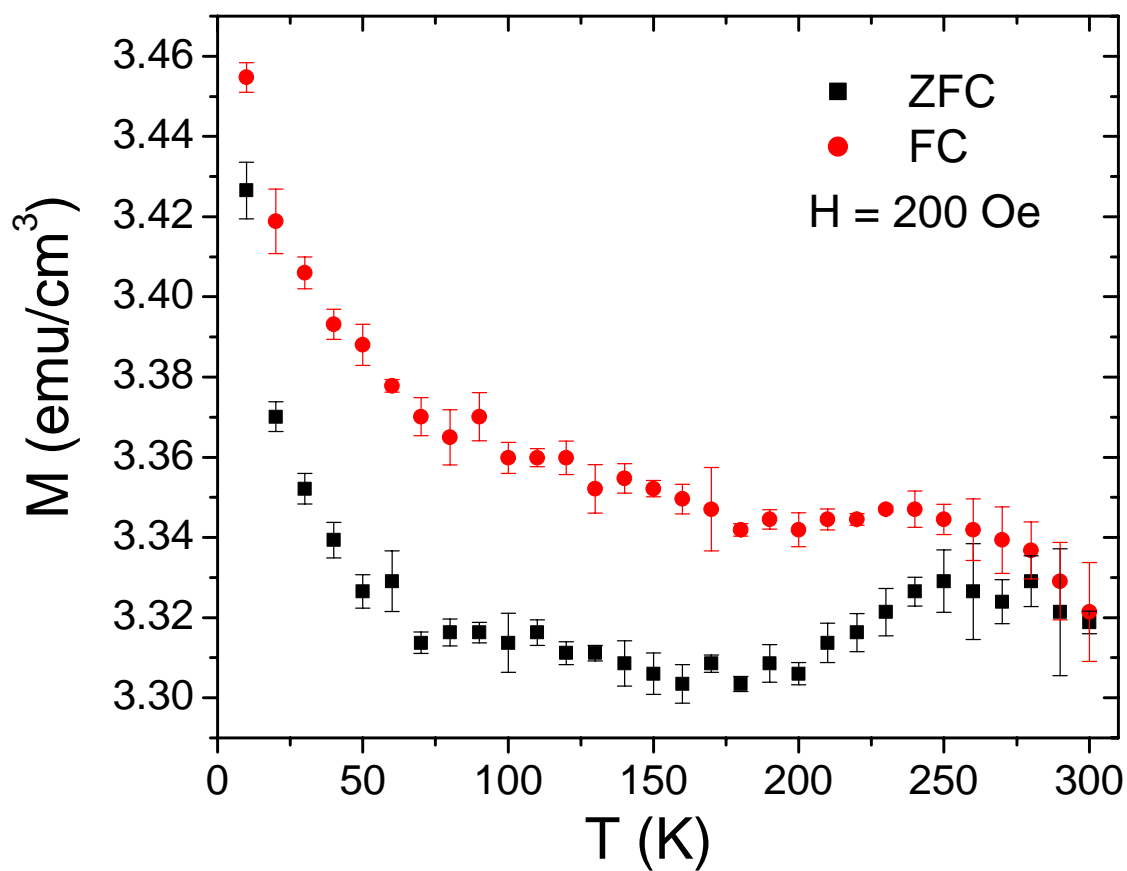


Figure 8-7. Magnetization versus temperature traces for field cooled and zero field cooled curves are shown for 5x GaGdN:Si/AlN 180Å/80Å layers.

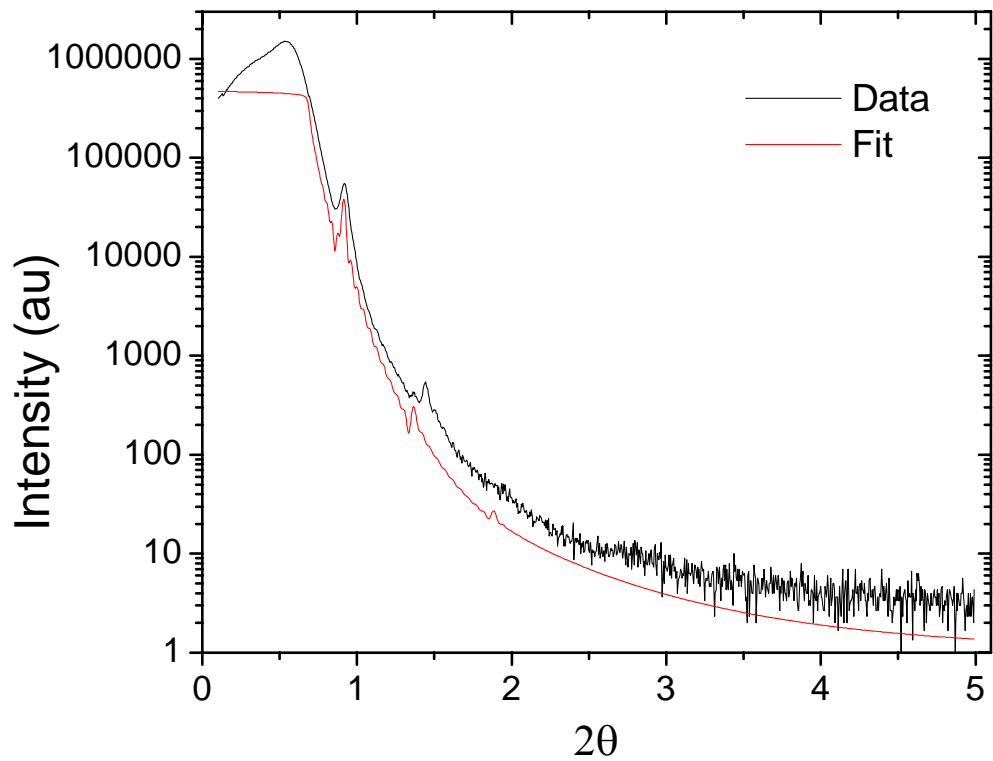


Figure 8-8. Figure 8-3. XRR spectrum is shown for the 10 periodicity GaN/AlGaIn:Gd sample with layer thicknesses of 8.7/18.54nm. The data is shown in black, while the fit curve is in red.

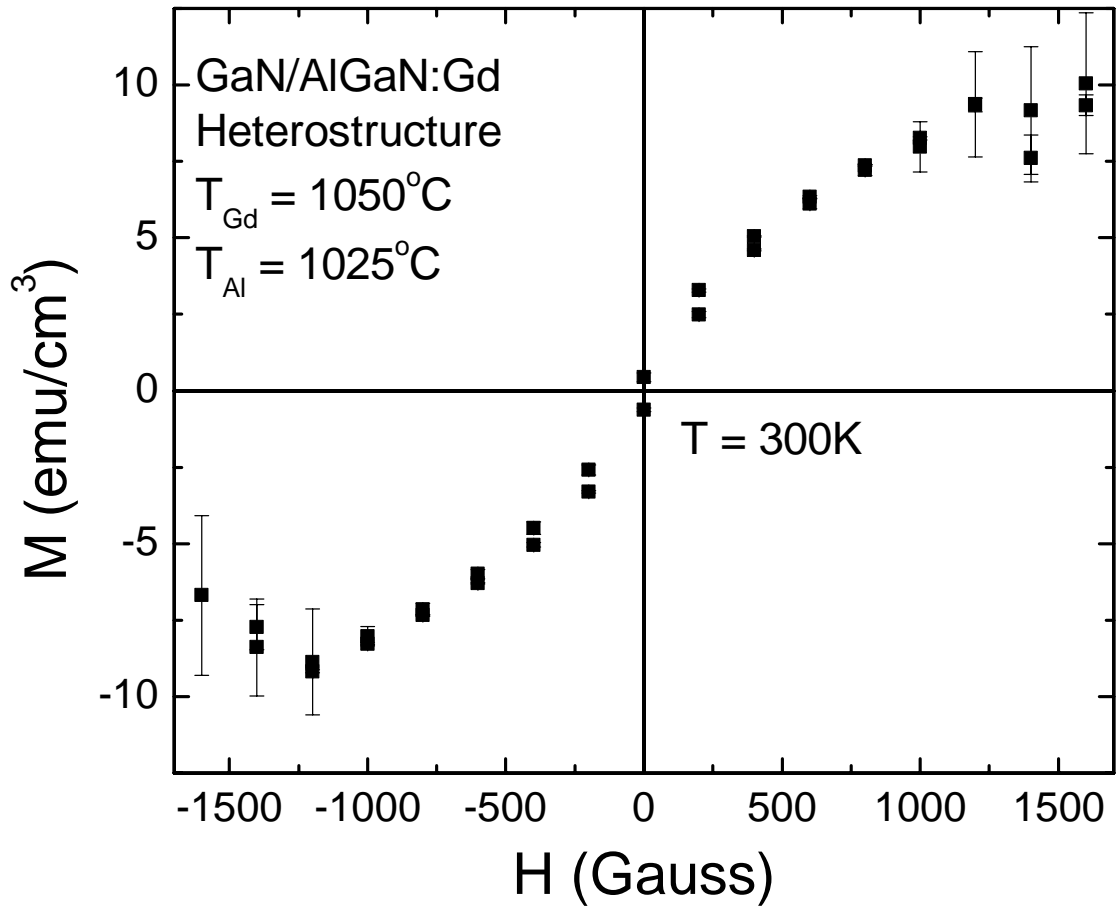


Figure 8-9. Hysteresis loop is shown for 10 repetitions of 18.5/8.7nm AlGaIn:Gd/GaN layers taken at 300K.

## CHAPTER 9 SUMMARY AND FUTURE WORK

Devices based on AlGaIn/GaN structures have been responsible for many of the advancements in novel semiconductor applications. Expanding this structure to spintronic uses requires that the material retain ferromagnetism at room temperature. Using transition metal dopants, such as Cr and Mn, for dilute magnetic semiconductors has required large atomic concentrations of dopant in order to optimize the magnetic signal. Unfortunately, this also leads to the existence of an impurity band, making the discrete spin splitting required for spintronic applications very difficult. Instead, GaN doped with the rare earth metal Gd has been shown to have a colossal magnetic moment at concentrations much below atomic percentages. This material is rather new in the DMS realm, and even the mechanism involved is not well understood. This dissertation has focused on characterizing and qualifying Gd as a possible dopant for spintronic devices. This chapter summarizes the findings and also gives some promising results, which should lead to the future continuation of work in the area of GaN based spintronics.

The GaGdN films were shown to have room temperature ferromagnetism when grown via gas source molecular beam epitaxy, even when doped at exceedingly low levels ( $<10^{16}$  atom/cm<sup>3</sup>). This fulfills the first roadblock in fabricating a practical DMS, while adding the additional advantage of not producing an impurity band, unlike more studied dopants such as Mn. These films were also highly resistive and did show an additional PL peak at 1.7eV due to intra-*f* level transitions. The maximum saturation magnetization demonstrated under these conditions was 6.8 emu/cm<sup>3</sup> when taken at room temperature. This is higher than both GaCrN and GaMnN, and does not possess the possibility that secondary phases are triggering the ferromagnetism. By measuring the magnetization of films of varying thicknesses, it was established that although ferromagnetism is dependent on crystal quality, it is a bulk, not surface, property. This finding fulfills yet another requirement toward qualifying Gd as a practical III-nitride DMS dopant.

An additional advantage in DMS materials for device usage is the ability to manipulate the Fermi level. By codoping the GaGdN films with Si, this ability was also demonstrated. Not only did the GaGdN:Si films display hysteresis, but the saturation magnetization increased linearly with Si incorporation. Correspondingly, the conductivity of the films also increased with Si content. Addition of Si into the films also appeared to smooth out growth, allowing films to attain greater thickness before turning to 2D/3D growth.

Since GaN-based devices have been shown to be radiation resistant, and, as such, are highly useful for space-based operations, radiation effects were also examined for DMS materials. Exposure of GaCrN and GaGdN to proton irradiation at 10 and 40 MeV under a dosage of  $5 \times 10^9 \text{ cm}^{-2}$  was performed. Photoluminescence spectroscopy of the films before and after irradiation revealed decreasing band edge luminescence with irradiation for both materials. This same trend was observed for magnetizations of the samples, with GaGdN showing a much larger degradation than GaCrN. This is partially explained by the lack of an impurity band in GaGdN. A model was proposed for the magnetic response based on proton energy causing the depletion of deep traps within the films, from which arose increasing competition for electrons to polarize. Since a percolation model of ferromagnetism fits the behavior of GaCrN and GaGdN, this would also decrease the overall magnetization of the films. The optical response most likely develops due to radiation induced depopulation of deep traps, turning such traps into non-radiative recombination centers. By annealing the samples under nitrogen plasma for 30 minutes at 500°C and nitrogen introduction at 1.3 sccm, a complete magnetic recovery was observed for all of the samples except for the as grown GaGdN.

During GaN device processing, films are regularly exposed to temperatures above 700°C, especially during ohmic contact annealing. With this in mind, Gd-based DMSs must also withstand thermal annealing at high temperatures without complete loss of room temperature magnetization. Annealing was performed under several conditions: ambient nitrogen, nitrogen plasma, and oxygen plasma. Annealing under ambient nitrogen by rapid thermal anneal (RTA) between 300 and 900°C

showed both GaGdN and GaGdN:Si films fall to between 75 and 70% of the as grown saturation magnetization values, where the largest loss was recorded for GaGdN. To determine if this was an effect of nitrogen loss during the RTA, a study was launched investigating the role of nitrogen incorporation on magnetization in GaGdN. Insufficient as well as overabundant amounts of nitrogen degraded the signal. This study also revealed that the flow rate of 1.6 sccm, which has been used for all previous work, was not optimal. Instead, the highest signal was obtained at a flow rate of 1.8 sccm. Nitrogen plasma annealing of these samples (30 minutes at 500 and 700°C with 1.3 sccm nitrogen) showed that the magnetic signal of those with sufficient incorporation decreased with increasing plasma anneal temperatures. This concurs with the outlier result from radiation where the as grown sample was the only one that experienced a decrease in magnetization from plasma annealing. The films were also exposed to ultraviolet ozone before and after annealing, which would also bombard the material with energy, to aid in determination of the mechanism involved in magnetic degradation. The mechanism behind this behavior may also arise from a depletion of traps. In the irradiation case, radiation depopulates deep level traps, and annealing may have caused a repopulation of the traps, which would also decrease competition for polarizing electrons, thus increasing the magnetization.

These results have shown that GaGdN and GaGdN:Si possess the desired bulk qualities for device fabrication. The next issue to be investigated was if the same would be true of AlGaN:Gd. Varying the Al cell temperature from 1000-1100°C resulted in samples that all demonstrated hysteresis at room temperature. The saturation magnetization values were fairly uniform, between about 3 and 5 emu/cm<sup>3</sup>. The exception was one sample with magnetization of 21 emu/cm<sup>3</sup>. The coercivity of these films was between 60 and 30 Oe, decreasing with Al composition. Thermal annealing under nitrogen plasma was also investigated, and showed a loss of half of the as grown magnetic signal. Since the sample possessed a high saturation magnetization to begin with, the resulting value was still sufficiently large.

Moving even further toward device incorporation, heterostructures were fabricated using GaGdN, GaGdN:Si, and AlGaN:Gd. By growing several layers of thin DMS films separated by buffers of either AlN or GaN, an adequate thickness of DMS material will accumulate to register via SQUID magnetometry. Using this method and materials, the Gd-based DMSs exhibited hysteresis at layer thicknesses between 90 and 154Å.

From the previous studies, it has been demonstrated that Gd is a promising candidate for spintronic device applications. Room temperature hysteresis, sufficient magnetic signal with thermal annealing, tunable Fermi energy, and ferromagnetism at reduced dimensions are all qualities possessed by the Gd-doped films. All of these characteristics are combined with the likelihood of a single impurity level. Further studies to understand the mechanism and effects of depopulated traps should be undertaken, including investigating the trap lifetime after radiation, and optical excitation of the materials to determine trap location.

The next major step is to incorporate these materials into a device in order to prove functionality. The simplest of which might be a spin valve. This is a possibility using a structure based on AlGaN:Gd and GaGdN:Si. The limitation in using these devices is the similarity in coercive fields. At lower saturation magnetization, the AlGaN:Gd has an appreciably larger coercivity (60 Oe) than the GaGdN:Si (35 Oe), so some magnetic signal may be sacrificed to obtain sufficient control for a device based on these materials.

## LIST OF REFERENCES

1. P. Ball, Nature **404**, 918 (2000).
2. S. A. Wolf, and D. D. Awschalom, Science **294**, 1488 (2001).
3. D. D. Awschalom, M. E. Flatte, and N. Samarth, Sci. Am. **286**, 66 (2002).
4. H. Akinaga and H. Ohno, IEEE Trans. Nanotech. **1**, 9 (2002).
5. S. A. Wolf and D. Treger, IEEE Trans. Magnetics **36**, 2748 (2000).
6. Das Sarma, S., American Scientist **89**, 516 2001.
7. M. Oestrich, J. Hubner, D. Hagele, P. J. Klar, W. Heimbrod, W. W. Ruhle, D. E. Ashenford, B. Lunn, Appl. Phys. Lett. **74**, 1251 (1999).
8. S. Das Sarma, E. H. Hwang, A. Kaminski, Cond. Mat. **1**, 1 (2003).
9. S. von Molnar, D. Read, J. Mag. And Mag. Mat. **242-245**, 13 (2002).
10. B. T. Jonker, X. Liu, W. C. Chou, A. Petrou, J. Warnock, J. J. Krebs, G. A. Prinz, J. Appl. Phys. **69**, 6097-6102 (1991).
11. H. Ohno, J. Magnet. Mag. Mater. **200**, 110 (1999).
12. H. Ohno, Science **281**, 951 (1998).
13. T. Dietl, H. Ohno, Physica E **9**, 185 (2001).
14. M.E. Overberg, B.P. Gila, G.T. Thaler, C.R. Abernathy, S.J. Pearton, N. Theodoropoulou, K.T. McCarthy, S. Arneson, A.F. Hebard, S.N.G. Chu, R.G. Wilson, J.M. Zavada and Y.D. Park, J. Vac. Sci. Tech. B **20**, 969 (2002).
15. M. Hashimoto, Y. K. Zhou, H. Tampo, M. Kanamura, H. Asahi, J. Crystal Growth **252**, 499 (2003).
16. G. Thaler, R. Frazier, B. Gila, J. Stapleton, M. Davidson, C. R. Abernathy, S. J. Pearton, C. Segre, Appl. Phys. Lett. **84**, 1314 (2004).
17. G. Thaler, R. Frazier, B. Gila, J. Stapleton, M. Davidson, C. R. Abernathy, S. J. Pearton, C. Segre, Appl. Phys. Lett. **84**, 2578 (2004).
18. Z. Liu, J. De Boeck, V. V. Moshchalkov, and G. Borghs, J. Mag. Mag. Mat. **242-245**, 967 (2002).
19. R. Frazier, G. Thaler, M. Overberg, B. Gila, C. R. Abernathy, and S. J. Pearton, Appl. Phys. Lett. **83**, 1758 (2003).

20. H. Munekata, H. Ohno, S. von Molnar, A. Segmeuller, L. L. Chang, and L. Esaki, *Phys. Rev. Lett.* **63**, 1849-1852 (1989).
21. H. Ohno, H. Munekata, S. von Molnar, and L. L. Chang, *J. Appl. Phys.* **69**, 6103 (1991).
22. H. Munekata, T. Abe, S. Koshihara, A. Oiwa, M. Hirasawa, S. Katsumoto, Y. Iye, C. Urano, and H. Takagi, *J. Appl. Phys.* **81**, 4862 (1997).
23. M. E. Overberg, C. R. Abernathy, S. J. Pearton, N. A. Theodoropoulou, K. T. McCarthy, A. F. Hebard, *Appl. Phys. Lett.* **79**, 1312 (2001).
24. S. Sonoda, S. Shimizu, T. Sasaki, Y. Yamamoto, H. Hori, *J. Crystal Growth* **237**, 1358 (2002).
25. H. X. Liu, S. Y. Wu, R. K. Singh, L. Gu, D. J. Smith, N. Newman, N. R. Dilley, L. Montes, and M. B. Simmonds, *Appl. Phys. Lett.* **85**, 4076 (2004).
26. Y.-K. Zhou, M. Hashimoto, M. Kanamura, and H. Asahi, *J. Supercond.* **16**, 37 (2003).
27. G. T. Thaler, R. M. Frazier, C. R. Abernathy, and S. J. Pearton, *Appl. Phys. Lett.* **86**, 131901 (2005).
28. R. K. Singh, S. Y. Wu, H. X. Liu, L. Gu, D. J. Smith, and N. Newman, *Appl. Phys. Lett.* **86**, 012504, (2005).
29. A. Y. Polyakov, N. B. Smirnov, A. B. Govorkov, G. T. Thaler, R. M. Frazier, C. R. Abernathy, and S. J. Pearton, *J. Vac. Sci. Technol. B.* **23**, 1 (2005).
30. Asahi, Y. K. Zhou, M. Hashimoto, M. S. Kim, X. J. Li, S. Emura, S. Hasegawa, *J. Phys.: Condens. Matter* **16**, S5555 (2004).
31. J. K. Hite, G. T. Thaler, R. Khanna, C. R. Abernathy, S. J. Pearton, J. H. Park, A. J. Steckl, and J. M. Zavada, *Appl. Phys. Lett.* **89**, 132119 (2006).
32. M. Hashimoto, A. Yanase, R. Asano, H. Tanaka, H. Bang, K. Akimoto, H. Asahi, *Jpn. J. Appl. Phys.* **42**, L1112 (2003).
33. A. Svane, N. E. Christensen, L. Petit, Z. Szotek, W. M. Temmerman, *arXiv:cond-mat* **1**, 603288 (2006).
34. N. Teraguchi, A. Suzuki, Y. Nanishi, Y.-K. Zhou, M. Hashimoto, and H. Asahi, *Sol. State Comm.* **122**, 651 (2002).
35. S. Y. Han, J. Hite, G. T. Thaler, R. M. Frazier, C. R. Abernathy, S. J. Pearton, H. K. Choi, W. O. Lee, Y. D. Park, J. M. Zavada, R. Gwilliam, *Appl. Phys. Lett.* **88**, 042102 (2006).
36. S. Dhar, O. Brandt, M. Ramsteiner, V. F. Sapega, and K. H. Ploog, *Phys. Rev. Lett.* **94**, 037205 (2005).
37. S. Dhar, L. Perez, O. Brandt, A. Trampert, K. H. Ploog, J. Keller, and B. Beschoten, *Phys. Rev. B* **72**, 245203 (2005).

38. S. Dhar, T. Kammermeier, A. Ney, L. Perez, K. H. Ploog, A. Melnikov, A. D. Wieck, *Appl. Phys. Lett.* **89**, 062503 (2006).
39. D. Chiba, N. Akiba, F. Matsukura, Y. Ohno, and H. Ohno, *Appl. Phys. Lett.* **77**, 1873 (2000).
40. M. Tanaka and Y. Higo, *Phys Rev. Lett.* **87**, 22602-1 (2001).
41. F. V. Kyrychenko, C. J. Stanton, C. R. Abernathy, S. J. Pearton, F. Ren, G. Thaler, R. Frazier, I. Buyanova, J. P. Bergman, and W. M. Chen, *Physics of Semiconductors: 27<sup>th</sup> International Conference on the Physics of Semiconductors*, p. 1319 (2005).
42. M. S. Kim, Y. K. Zhou, S. Kimura, S. Emura, S. Hasegawa, and H. Asahi, *J. Crystal Growth* **278**, 675 (2005).
43. J. E. Medvedeva, A. J. Freeman, X. Y. Chui, C. Stampfl, and N. Newman, *Phys. Rev. Lett.* **94**, 146602 (2005).
44. S. Y. Wu, H. X. Liu, L. Gu, R. K. Singh, L. Budd, M. Van Schlifgaarde, M. R. McCartney, D. j. Smith, and N. Newman, *Appl. Phys. Lett.* **82**, 3047 (2003).
45. R. M. Frazier, G. T. Thaler, J. Y. Leifer, J. K. Hite, B. P. Gila, C. R. Abernathy, and S. J. Pearton, *Appl. Phys Lett.* **86**, 52101 (2005).
46. C. Zener, *Phys. Rev.* **81**, 440 (1951).
47. T. Dietl, H. Ohno, F. Matsukura, J. Cibert, and D. Ferrand, *Science* **287**, 1019 (2000).
48. T. Dietl, *J. Appl. Phys.* **89**, 7437 (2001).
49. V. I. Litvinov, *Phys. Rev B* **72**, 195209 (2005).
50. V. I. Litvinov and V. K. Dugaev, *Phys. Rev. Lett.* **86**, 5593 (2001).
51. A. Kaminski and S. Das Sarma, *Phys. Rev. B* **68**, 235210 (2003).
52. A. Kaminski and S. Das Sarma, *Phys. Rev. Lett.* **88**, 247202-1 (2002).
53. M. Berciu and R. N. Bhatt, *Phys. Rev. B* **69**, 45202 (2002).
54. M. Berciu and R. N. Bhatt, *Phys Rev Lett.* **87**, 107203-1 (2001).
55. A. L. Chudnovskiy and D. Pfannkuche, *Phys. Rev. B* **65**, 165216-1 (2002).
56. G. M. Dalpian and S.-H. Wei, *Phys. Rev. B* **72**, 115201 (2005).
57. R. M. Frazier, "Influence of Cation Choice on Magnetic Behavior of III-N Dilute Magnetic Semiconductors," Gainesville, FL (2005).
58. W. L. Lambrecht, presented at the Workshop on Gd-Doped Nitride Semiconductors , Gainesville, FL, Feb 2006.

59. M. M. Entsev, V. Y. Davydov, E. E. Haller, A. A. Klochikhin, V. V. Koslovskii, G. A. Oganesyanyan, D. S. Poloskin, N. M. Schmidt, V. A. Vekshin and A. S. Usikov, *Phys. B: Cond. Mat.* **308-310**, 58 (2001).
60. D. C. Look, D. C. Reynolds, J. W. Hemsky, J. R. Sizelove, R. L. Jones, and R. J. Molnar, *Phys. Rev. Lett.* **79**, 2273 (1997).
61. K. H. Chow, G. D. Watkins, Akira Usui, and M. Mizuta, *Phys. Rev. Lett.* **85**, 2761 (2000).
62. R. Khanna, K. K. Allums, C. R. Abernathy, S. J. Pearton, J. Kim, F. Ren, R. Dwivedi, T. N. Fogarty, R. Wilkins, *Appl. Phys. Lett.* **85**, 3131 (2004).
63. M. Osinski, P. Perlin, H. Schoene, A. H. Paxton, and E. W. Taylor, *IEE Electronic Letters* **33**, 1252 (1997).
64. S. J. Cai, Y. S. Tang, R. Li, Y. Y. Wei, L. Wong, Y. L. Chen, K. L. Wang, Mary Chen, Y. F. Zhao, R. D. Schrimpf, J. C. Keay, and K. F. Galloway, *IEEE Trans. Electron Devices* **47**, 304 (2000).
65. B. Luo, J. W. Johnson, F. Ren, K. K. Allums, C. R. Abernathy, S. J. Pearton, R. Dwivedi, T. N. Fogarty, R. Wilkins, A. M. Dabiran, A. M. Wowchack, C. J. Polley, P. P. Chow, A. G. Baca, *J. Elect. Mat.* **31**, 437 (2002).
66. X. Hu, A. P. Karmarkar, B. Jun, D. M. Fleetwood, R. D. Schrimpf, R. D. Geil, R. A. Weller, B. D. White, M. Batiaev, L. J. Brillson, and U. K. Mishra, *IEEE Transactions on Nuclear Science* **50**, 1791 (2003).
67. K. K. Allums, "Proton Radiation and Thermal Stability of Gallium Nitride and Gallium Nitride Devices," <http://purl.fcla.edu/fcla/etd/UFE0013123>, Gainesville, FL (2006).
68. S. von Molnar, *J. Superconductivity: Incorporating Novel Magnetism* **16**, 1 (2003).
69. S. von Molnar and D. Read, *Proc. IEEE* **91**, 715 (2003).
70. M. L. Reed, N. A. El-Masry, H. H. Stadelmaier, M. E. Ritums, N. J. Reed, C. A. Parker, J. C. Roberts, and S. M. Bedair, *Appl. Phys. Lett.* **79**, 3473 (2001).
71. G. T. Thaler, M. E. Overberg, B. Gila, R. Frazier, C. R. Abernathy, S. J. Pearton, J. S. Lee, S. Y. Lee, Y. D. Park, Z. G. Khim, J. Kim, and F. Ren, *Appl. Phys. Lett.* **80**, 3964 (2002).
72. Y. K. Zhou, M. S. Kim, X. J. Li, S. Kimura, A. Kaneta, Y. Kawakami, Sg Fujita, S. Emura, S. Hasegawa, H Asahi, *J. Phys.: Condens. Matter* **16**, S5743 (2004).
73. H. Tang, J. B. Webb, J. A. Bardwell, S. Rolfe, and T. MacElwee, *Solid-State Electronics* **44**, 2177 (2000).
74. J. W. Johnson, J. Han, A. G. Baca, R. D. Briggs, R. J. Shul, J. R. Wendt, C. Monier, F. Ren, B. Luo, S. N. G. Chu, D. Tsvetkov, V. Dmitriev, and S. J. Pearton, *Solid-State Electronics* **46**, 513 (2001).

75. X. L. Wang, C. M. Wang, G. X. Hu, J. X. Wang, T. S. Chen, G. Jiao, J. P. Li, Y. P. Zeng, and J. M. Li, *Solid State Electronics* **49**, 1387 (2005).
76. J. Han, M. H. Crawford, R. J. Shul, J. J. Figiel, M. Banas, and L. Zhang, *J. Appl. Phys.* **73**, 1688 (1998).
77. J. Shakya, K. Knabe, K. H. Kim, J. Li, J. Y. Lin, and H. X. Jiang, *Appl. Phys. Lett.* **86**, 091107 (2005).
78. E. Monroy, F. Calle, J. L. Pau, E. Munoz, F. Omnes, B. Beaumont, and P. Gibart, *J. Cryst. Growth* **230**, 537 (2001).
79. S. J. Pearton, C. R. Abernathy, M. E. Overberg, G. T. Thaler, D. P. Norton, N. Theodoropoulou, A. F. Hebard, Y. D. Park, F. Ren, J. Kim, and L. A. Boatner, *J. Appl. Phys.* **93**, 1 (2003).
80. R. M. Frazier, G. T. Thaler, C. R. Abernathy, S. J. Pearton, M. L. Nakarmi, K. B. Nam, J. Y. Lin, H. X. Jiang, J. Kelly, R. Rairigh, A. F. Hebard, J. M. Zavada, and R. G. Wilson, *J. Appl. Phys.* **94**, 4956 (2003).
81. X. Y. Liu and T. G. Anderson, *Appl. Surf. Sci.* **226**, 331 (2004).

## BIOGRAPHICAL SKETCH

Jennifer Hite was born on August 22, 1977, in Blytheville AFB, Arkansas. Born into a military family, she grew up moving every 2-5 years, residing in Arkansas, Louisiana, Nebraska, Germany, and Florida. In 1995, she graduated from Lake Mary High School in Lake Mary, Florida, and went on to attend the University of Florida on a National Merit Scholarship. She graduated with her bachelor's degree in chemical engineering in 2000 and went to work for Lucent Technologies as a PECVD Equipment Engineer. As the telecommunications industry took a rapid nose-dive, she returned to the University of Florida in the fall of 2001 to attain her graduate degree. She joined Cammy Abernathy's research group in the next year, and obtained a Master of Science in materials science and engineering in 2003. She then continued with several research projects before beginning to work on gadolinium-based materials..